Biomechanical modeling of fetal veins

The umbilical vein and ductus venosus bifurcation

Thesis for the degree of Philosophiae Doctor

Trondheim, November 2012

Paul Roger Leinan

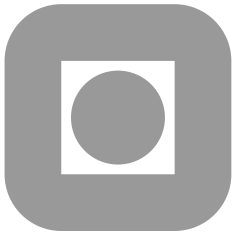

Norwegian University of Science and Technology
Faculty of Engineering Science and Technology
Department of Structural Engineering
Trondheim, Norway

Preface

This doctoral thesis is submitted to the Norwegian University of Science and Technology (NTNU) for the degree Philosophiae Doctor. The work has been carried out at the Department of Structural Engineering, NTNU. My supervisors have been Prof. Leif Rune Hellevik (Department of structural Engineering, NTNU), Prof. Bjørn Skallerud (Department of structural Engineering, NTNU) and Dr.ir. Joris Degroote (Department of Flow, Heat and Combustion Mechanics, Ghent University, Belgium).

The thesis has been financed by a grant from the Faculty of Engineering Science and Technology at NTNU. Furthermore, the financial support from the Center for Biomedical Computing (CBC) for meetings at CBC, Fornebu, is gratefully acknowledged.

Acknowledgements

My sincere gratitude goes to my supervisor Prof. Leif Rune Hellevik and co-supervisor Prof. Bjørn Skallerud for their valuable guidance, and for trusting me with this doctoral project. Especially, I would like to thank Prof. Leif Rune Hellevik for his continuous support and enthusiasm for my work. I have learned a lot from his knowledge and advise in many insightful discussions throughout my period as a Ph.D candidate, which has advanced this project and my scientific skills. I am also grateful to Prof. Bjørn Skallerud for giving me the opportunity to learn from his broad experience base, and for his continuous encouragements. He introduced me to the field of Biomechanics, and his research perspective has extended my horizons. I am also indebted to the guidance from my co-supervisor Dr.ir. Joris Degroote, for sharing his understanding and work into the challenging field of fluid-structure interaction, and for his thorough reviews and keen eye for details.

I would also like to express my appreciation to Prof. Torvid Kiserud. His expertise as a physician and scientist, and his enthusiasm for fetal hemodynamics have motivated and given purpose to my work. A special thanks also goes to my former colleague and now Associate Prof. Victorien Prot, for his scientific contribution and everyday encouragement.

I thank Prof. Jan Vierendeels and Prof. Patrick Segers for including me in their research groups at Ghent University, for their hospitality during my visits and for their scientific contributions. I am also indebted to Prof. Frans van de Vosse for his support and hospitality during my stay at the Biomechanics Laboratory at Eindhoven University of Technology, where I was privileged to work on experimental testing of fetal umbilical veins. Additionally, I would like to acknowledge the contributions from Dr. Chantal van den Broek at HemoLab in Eindhoven, Dr.ir. Abigail Swillens at Ghent University and Prof. Christina Vogt at the Department of Laboratory Medicine at NTNU. Moreover, the students that trusted their Master degree projects on contributions from my work have my thanks: Aleksander, Thomas, Elisabeth and Vinzenz.

The everyday fun, with a nice blend of interesting work and a friendly atmosphere which I experienced at the Department of Structural Engineering would not have been possible without my fellow Ph.D candidates, thank you all.

Finally I would like to thank my family and friends for their continuous support, especially the patience and love from my close family Veronica, Martin and Linnea.

Trondheim, September 2012
Paul Roger Leinan

Contents

Part I

Introductory section

Chapter 1

Introduction

This thesis contains two parts. Part one is an introductory section organized in five chapters. The first chapter presents the motivations and aims of the project. The second chapter presents an overview of the major characteristics of feto-placental circulation relevant for this thesis work. The third chapter presents an overview of the mechanical and numerical concepts considered in the thesis. Chapter five concludes the introductory section, with concluding remarks and directions for future work. The second part of the thesis is a collection of four papers organized in four chapters. The papers are independent with its own introduction and conclusion, some information is therefore repeated.

1.1 Motivation

Knowledge about fetal circulation was for a long time based on invasive animal studies [94], especially in fetal sheep [45, 91, 165]. The introduction of obstetric Doppler ultrasound some 30 years ago, spurred new interest and research into the field of human fetal blood flows [63, 171]. The non-invasive capabilities of Doppler ultrasound have been utilized in numerous clinical studies on the fetal circulation system, such as blood flow in the fetal heart, aorta, umbilical arteries and veins [96, 105, 124, 130, 134]. In addition to standard obstetric ultrasound, Doppler ultrasound examination is today an important tool in the clinical evaluation of fetal wellbeing and development during the gestational period. The feto-placental circulation is one of the important focus areas, where abnormal flow patterns can signal pathologies, such as cardiac malformation, congestive heart disease, imminent asphyxia and chromosomal abnormalities [124, 126, 127, 130]. Computational mechanics can offer a physical basis and numerical tools for the analysis of blood flow in the fetal circulation system. Such knowledge can provide physicians with a deeper understanding of the fetal hemodynamics observed in a clinical setting, which may lead to new diagnostic tools and procedures, and a more physiological interpretation of findings.

The feto-placental circulation is essential in the development and growth of human fetuses, for the major parts of the gestational period [171]. In particular, the distribution of oxygen and

nutrients rich placenta blood to the fetal liver and heart has been given much attention in the literature [103]. An important vessel in this area of the fetal venous return is the ductus venous, a slender trumpet shaped vein that connects the intra abdominal umbilical vein to the inferior vena cava at its inlet to the heart. The ductus venosus enables blood from the placenta to bypass the liver and be shunted directly to the fetal heart. In fact, the ductus venosus is the main distributor of placental blood to the cerebral and coronary circulations [108, 126]. The blood distribution between the ductus venosus and the liver is therefore clinically interesting. Numerical modeling of blood flow in this area of the fetal venous return can significantly improve the confidence of flow rate estimation in a clinical setting, and therefore the distribution of placenta blood to organs in the fetal body [16, 151].

The pulsatile flow in the ductus venosus is an important clinical biomarker, and Maiz and Nicolaides [126] have called the ductus venosus ”A window into the fetal heart”. The contractions of the fetal heart generates pressure and flow waves which propagate into the venous return via the inferior vena cava and the ductus venosus [113]. Pulsatile flow in the ductus venosus is normal throughout gestation. However, increased pulsatility or abnormal velocity waveforms may signal pathology, such as chromosomal abnormalities [130]. The pulsatile nature of blood flow in the ductus venous and connecting veins can be investigated with computational methods [78, 79]. Development of numerical models for pulsatile blood flow is challenging, especially if the mutual interaction between the blood and the vessels is to be taken into account (fluid-structure interaction). However, such models may provide opportunities for new insights into the underlying mechanisms of both physiological and pathological conditions.

The umbilical cord is the vital lifeline that connects the fetus and the placenta, where blood can flow to the placenta through two umbilical arteries and back to the fetus trough the umbilical vein. The umbilical cord floats freely in the amniotic fluid and is responsible for structural integrity of the umbilical vessels, under a variety of loads such as internal pressure and viscous forces as well as external loads such as compression, stretching, torsion and bending, and must maintain an efficient passage for blood flow during gestation [47]. Several abnormalities which can influence the umbilical cord function have been investigated as risk factors in several studies, such as lean and hyper-coiled cord and severe umbilical constriction at the entrance through the abdominal wall of the fetus [46, 145, 172]. Models and parameters for the structural response of umbilical cord tissues are scares in the literature [47], increased focus on this area of fetal physiology may provide new insights into this important vascular organ for fetal development.

1.2 Aims and scope

This project is focused on numerical modeling of vessels mechanics and blood flow in areas of the feto-placental circulation, which is frequently examined in a clinical setting with Doppler ultrasound. The main aim of the thesis is to develop numerical models for blood flow in the fetal venous return (i.e. from the placenta to the fetal liver and heart), where the mutual interaction between the blood and surrounding tissue is taken into account. Hence, both structural modeling of vein tissue and blood flow needs to be included, as well as coupling strategies

between fluids and structures. Fluid-structure interaction (FSI) models of this area of the fetal circulation system may provide physicians with additional tools for diagnostic and research into fetal physiology and pathology. An equally important aim, is from a mechanical point of view, provide physicians with a deeper understanding of fetal blood flow phenomena observed in a clinical setting.

Computational fluid dynamics (CFD) models have been used to investigate pressure drop and velocity profiles in the intra abdominal umbilical vein and ductus venosus bifurcation [77, 151]. In the current work, we aim at a 3D FSI model of the ductus venosus and connecting veins, to include the compliance of the vessels and therefore the vessel deformations under hemodynamics loads. The literature offers limited material data for the intra abdominal umbilical vein and ductus venosus, and only simplified constitutive relations have been considered for these fetal veins [76]. We therefore aim at a constitutive model suitable for three-dimensional (3D) finite element simulations, which will be employed in our FSI modeling. An isotropic hyperelastic model will be investigated based on experimental data from inflation tests [76], which can account for the non-linear stress-strain behavior commonality observed in vascular tissue [83]. Such material models are capable of describing the macroscopic behavior of blood vessels, and are frequently used in vascular FSI simulations [14, 140, 181]. The initial focus of the FSI analysis will concern velocity profile predictions at the ductus venosus inlet through velocity profile coefficients [111, 151]. Velocity profile coefficients are clinically relevant for flow rate calculation with Doppler ultrasound, and therefore the flow distribution in the fetal venous return [115]. A secondary objective is to bring forward FSI modeling in fetal flows, and thus the potential for studying aspects of hemodynamics that cannot be accurately assessed with CFD.

At the present time 3D FSI is both computationally expensive and time consuming in the modeling and development phase. One-dimensional (1D) models for blood flow in compliant vascular networks is therefore an appealing alternative, even though such models simplifies the complex local hemodynamics. 1D models can simulate flow and pressure distribution in the vascular three with varying degree of complexity, and with considerably reduced computational costs compared to 3D FSI [161, 183]. We therefore aim at developing a 1D network model for vascular flow with the potential to include large portions of the feto-placental circulation, e.g. to study systemic pressure and flow distribution, and wave propagation.

The umbilical cord is a complex vascular organ immersed in the amniotic fluid. The human umbilical cord contains two umbilical arteries coiled in helical spirals around the umbilical vein. Furthermore, the three umbilical vessels are embedded in Wharton's jelly, a gelatinous substance rich in collagen fibers [47]. We aim at developing a constitutive fiber model for the structural response of the umbilical vein including the surrounding Wharton's jelly. Structural models may give new insights into the mechanical function of the umbilical cord, i.e. how this organ withstands both external loads and the internal hemodynamics loads, while at the same time provides an efficient passage for blood flow throughout gestation.

Chapter 2

Characteristics of fetal circulation

2.1 The feto-placental circulation

2.1.1 Development and maturation

The human pregnancy can be characterized by two phases, the embryonic and the fetal period. The embryonic phase includes approximately the first eight weeks after conception (tenth gestational week). Key developmental events take place during this period, such as embryogenesis, placentation and organogenesis [171]. The end of the embryonic period is characterized by the matured development of most of the major organs. The embryo is now called a fetus, and with a functioning cardiovascular system, the fetus receives oxygen and nutrients and exchanges waste products through umbilical circulation with the placenta. The remaining gestational period is characterized by fetal maturation and growth dependent on the umbilical circulation.

2.1.2 Blood volume and pressure

The total fetal blood volume is estimated to be 10-12% of the fetal body weight, compared to 7-8% in adults [28]. The main reason for this difference is the portion of the fetal blood volume present in the placenta [104]. Studies in fetal sheep have shown that 50% of the fetal blood volume is present in the placenta at 20 weeks of gestation, and falls to 20% at term [9]. The estimated blood volume contained within the fetal body is 80 ml/kg which is marginally more than in adults [103]. The cardiac output normalized for fetal weight is unchanged during gestation at approximately 400 ml/(min kg). However, at mid gestation 30% of the cardiac output enters the placenta, which falls to 20% after 32 weeks [112].

The umbilical vein blood pressure have been measured during cordocentesis in normal human fetuses, giving a mean value of 4.5 mmHg at mid term and 6.5 mmHg at term [188]. Weiner et al. [192] found similar values but no increase with gestational age. Johnson et al. [92] measured average pressures (during the cardiac cycle) in both atria to be 3.5 mmHg, which remained constant during gestation. Furthermore, the systolic ventricular pressure was found to be 15-20 mmHg at 16 weeks and increase to 30-40 mmHg at 20 week, with negligible difference

between the two ventricular chambers but with significant subject variance [92]. The diastolic ventricular pressure was measured to be less than 5 mmHg at 16-19 weeks of gestation, and 5-15 mmHg at 19-26 weeks of gestation [92].

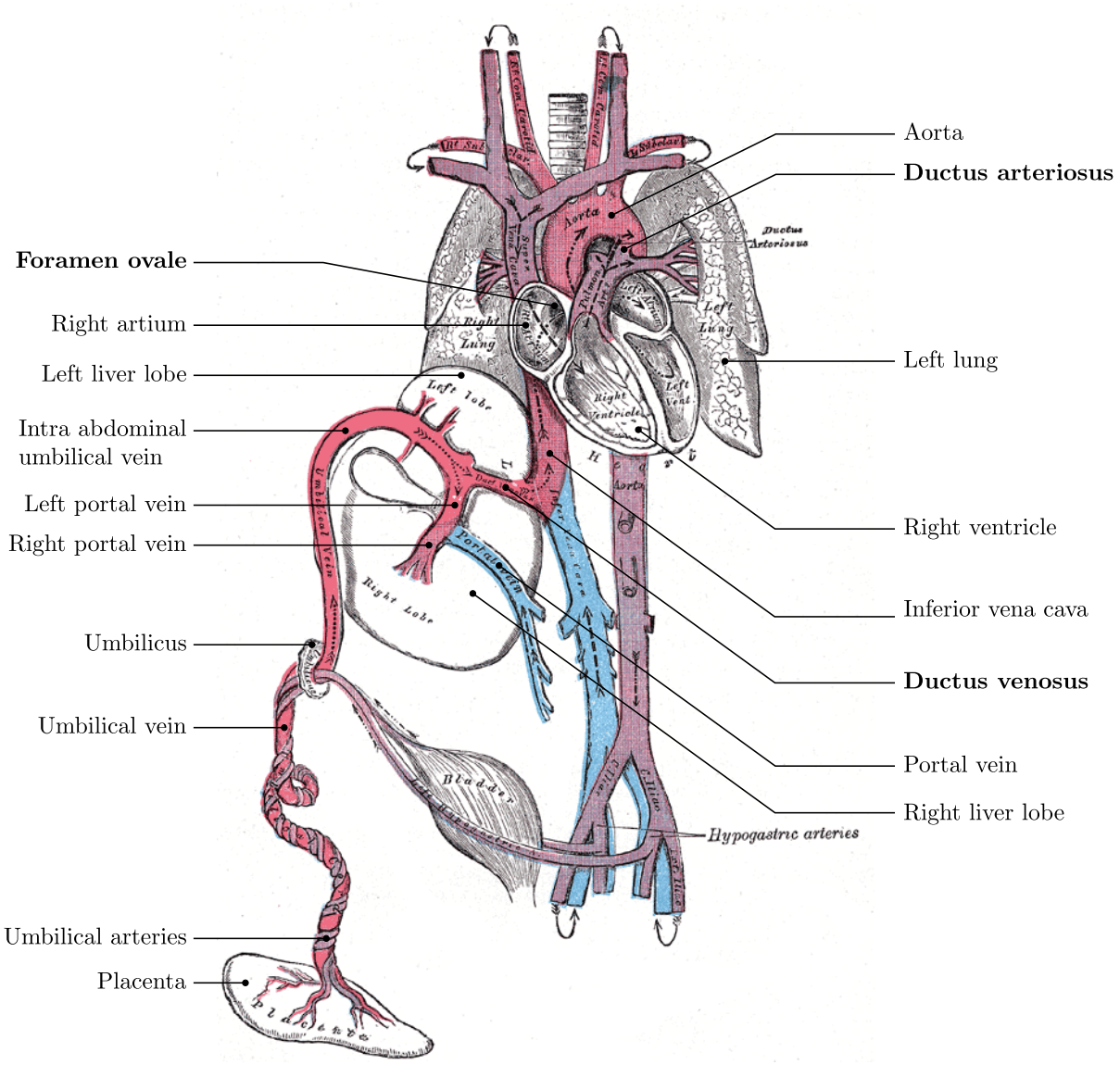

Figure 2.1 Overview of fetal circulation illustrating among other the fetal shunts (boldface), the Ductus arteriosus, the Foramen ovale and the Ductus venosus (Adapted form [66, Gray, H. (1918). Anatomy of the human body, 20th U.S. edition]. The representation of the ductus venosus, inferior vena cava and foramen ovale in this illustration is distorted and does not reflect normal relations that are presented in later illustrations.)

2.1.3 Flow distribution and fetal shunts

In adults, we find that the right and left side of the heart works in series to pump the blood through the lungs (pulmonary circulation) and then the rest of the body (systemic circulation). In the fetus both ventricles pump blood in parallel, primarily to the systemic circulation, due to the ductus arteriosus a short vessel that acts as a shunt and connects the pulmonary artery to the descending aorta (Fig. 2.1). Conditional to gestational age 13-25% of the total cardiac output is directed to the lungs while 40% passes through the ductus arteriosus and flows towards the lower fetal body and the placenta [160].

Blood leaves the fetus via two umbilical arteries embedded in umbilical cord and enters the villous network of the placenta which allows for exchange of gases, nutrients and waste products between the maternal and fetal blood. The oxygen and nutrient rich placenta blood is directed back to the fetus through the umbilical vein. The placenta blood enters the fetal body at the umbilical navel (umbilicus) and flows into the intra abdominal umbilical vein, which is partially embedded in the underside of the left liver lobe (Fig. 2.1). The intra abdominal umbilical vein supplies blood to the left liver lobe through minor vessels along its length. The remaining blood volume is shared between the ductus venosus and the right liver lobe via the left portal vein. The right liver lobe also receives blood with modest oxygen saturation from the lower fetal body through the portal vein. Fetal blood with the lowest oxygen saturation is found in the portal vein (30%) and inferior vena cava (35%), while the highest saturation is found in the umbilical vein and the ductus venosus (80%) [94].

The ductus venous connects the intra abdominal umbilical vein to the inferior vena cava close to its inlet to the heart. (Fig. 2.2). The ductus venosus is therefore an important distributional unit, that shunts highly oxygenated blood into the fetal heart for distribution to other crucial organs. Indeed, the ductus venosus is the main distributor of highly oxygen saturated blood to the cerebral and coronary circulations [108, 126]. None-invasive human studies have shown a shunt fraction through the ductus venosus of 30% at mid gestation and 20% near term, of the total blood flow rate from the placenta. However, the shunt fraction can increase during situations of reduced fetal blood flow rate and oxygen saturation [17, 70].

The third fetal shunt is the foramen ovale (Fig. 2.1), which is a hole between the two atrial chambers that is slightly tilted over the inlet of the inferior vena cava (Fig. 2.2). It has been shown that blood flowing from the ductus venosus is mainly directed through the foramen ovale due to the alignment of the ductus venosus with foramen ovale, and due to the slender shape of the ductus venosus which accelerates the blood and opens the foramen ovale flap [102]. Hence, highly oxygen saturated blood from the placenta can be shunted through the ductus venosus and foramen ovale, and into the left atrium and the left ventricle for rapid distribution to the upper and lower fetal body by the aorta.

The umbilical circulation with the placenta and the three fetal shunts (the ductus arteriosus, ductus venous and foramen ovale), are characteristic to the fetal circulation. This special vascular arrangement is important for an adaptive fetal circulation system, because compared to postnatal life the fetus does not relay on oxygen and nutrient uptake from the lungs and gut. The fetal shunts are expected to be functionally closed within the first weeks after birth, and a normal adult circulation system is established [141].

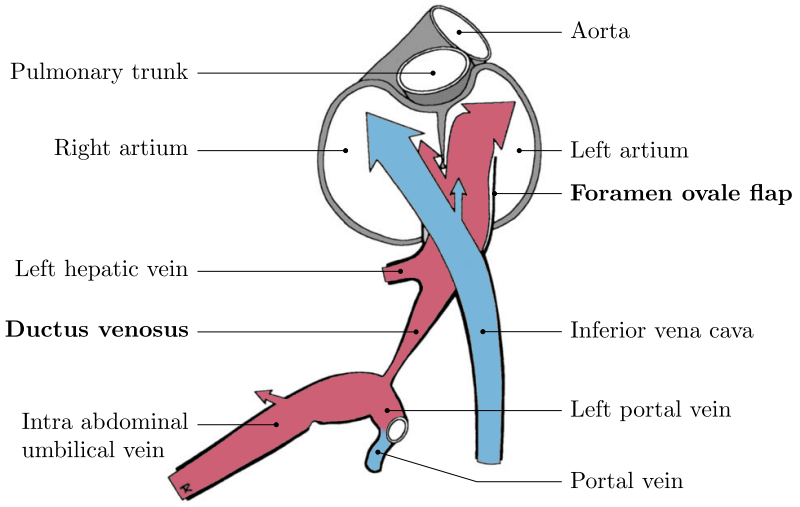

Figure 2.2 Venous return from the inferior vena cava (IVC) into the right atrium, and from the ductus venous (DV) through the foramen ovale (FO) flap and into the left atrium (LA). Adapted from Kiserud [103].

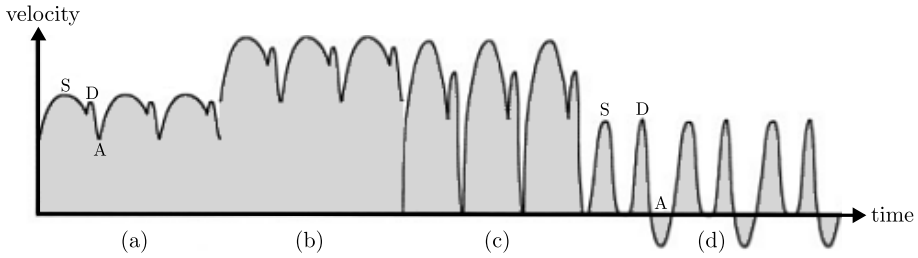

Figure 2.3 Illustration of blood flow velocity in the ductus venosus. (a) Normal velocity wave forms, with a peak during ventricular systole (S), a peak during diastolic filling (D) and a nadir during atrial contraction (A). (b) An increase in flow velocities, caused by an increased portocaval pressure gradient (e.g. liver disease, anemia). (c) An increased nadir during atrial contraction reflects increased end-diastolic pressure commonly seen in placental compromise. (d) Further deterioration may give reversed flow during the atrial contraction (A wave). Adapted from Kiserud and Acharya [104].

2.1.4 The ductus venosus

The ductus venous is a slender conical vein with a narrow inlet that connects the intra abdominal umbilical vein to the inferior vena cava (Fig. 2.2). The morphology of the ductus venosus has been investigated in several studies [2, 134, 136, 178], and the ductus venous is described as similar to other vascular tissue containing muscular, elastin and collagen fibers. The main *in vitro* geometrical features of the human ductus venosus have been measured with ultrasound by several authors [1, 15, 16, 110]. Kiserud et al. [110] reported a mean length of 5 mm at 18 weeks and 15 mm at 34 weeks of gestation. The mean diameter was 0.5 mm at the inlet and 2.0 mm at the outlet at mid gestation, and 1.5 mm at the inlet and 3.0 mm at the outlet

at 34 week of gestation, furthermore the inlet diameter of the ductus venosus hardly exceeds 2 mm during pregnancy. The portocaval pressure gradient, i.e. the pressure difference between the umbilical vein and the inferior vena cava, accelerates blood through the ductus venous, from a mean velocity of 10-22 cm/s in the intra abdominal umbilical vein to 60-85 cm/s in the ductus venosus [6, 105]. The high velocity jet emerging from the ductus venosus is believed to constitute the preferential streaming of blood through the foramen ovale into the left atrium. Additionally, the preferential streaming is facilitated by the alignment and the short distance between the ductus venosus outlet and the foramen ovale, as illustrated in Fig. 2.2 [106].

The liver receives most of the placenta blood in human fetuses, 70% at mid gestation and 80% at term [115], while the remaining placenta blood volume is shunted through the ductus venosus. Hence, indicating the importance of the liver for human fetal development [94]. Distributional mechanisms of the ductus venosus seen in animal studies also seems to operate in humans. The ductus venosus is under tonic adrenergic control and distends under chemical influence [103]. The most extensive dilatation is seen during hypoxia, leading to a 60% diameter increase along the length of the ductus venosus in a study of fetal sheep, which significantly increases shunting through the ductus venosus [114]. The ductus venosus seems to have an important distributional role, however its physiological role is not well understood, e.g. while agenesis (failure of an organ to develop) of the ductus venosus is linked to a range of fetal pathologies, ductus venosus agenesis is also found in normal human pregnancies [104].

The venous flow exiting the placenta into the umbilical vein is steady. However, pulsating flow in the ductus venosus is normal throughout gestation and originates from the pulsatile flow in the fetal heart, which accelerates and decelerates the flow in the ductus venosus [113]. These flow pulsations can also propagate in the umbilical vein, which is a normal finding before 13 weeks of gestation [102]. The characteristic waveform of pulsatile flow in the ductus venosus during a cardiac cycle have been identified as a valuable clinical biomarker [26, 27, 109, 126, 130, 131]. The ductus venosus waveform is recognized by a peak during ventricular systole, a second peak during during diastolic filling and a nadir during atrial contraction (A-wave), as illustrated for normal ductus venosus flow in Fig. 2.3 (a). Ductus venosus velocity waveform examination by Doppler ultrasound is progressively used to identify hypoxaemia, acidosis, cardiac decompensation and placental compromise, and is a promising diagnostic tool for timing the delivery of critically ill fetuses [10, 72, 103]. Furthermore, increased ductus venosus pulsatility or abnormal velocity waveforms may signal chromosomal abnormalities [130]. An extensive review on ductus venosus waveform indexes can be found in Maulik [132].

2.1.5 The umbilical cord

The human umbilical cord is the vital lifeline that facilitates blood flow from the fetus to the placenta through two umbilical arteries for oxygenation, nourishment and exchange of waste products, and back to the fetus through the umbilical vein (Fig. 2.1) [171]. The normal cord length is 50-60 cm at term, and the cord is attached to the fetus at the umbilical navel (umbilicus) at the fetal end, and normally to the placenta midpoint at the placental end. Hence, the body of the umbilical cord is freely immersed in the amniotic fluid contained in the amniotic sac. The tissues that make up the umbilical cord structure are therefore responsible for maintaining blood

flow during fetal grasping, movements, and other forces during gestation and birth [47]. The umbilical vessels are coiled around each other in helical spirals, and the degree of coiling can be identified by the umbilical coiling index (number of coils divided by cord length). A coiling index of 17-22 m^{-1} is considered normal, however hyper-coiled and non-coiled cords are not uncommon [21, 145].

The umbilical vessels, the vein and two arteries, are embedded in Wharton's jelly (Fig. 7.1), an elastic collagen-based extracellular matrix with interconnected fluid-filled pores [47]. Wharton's jelly does not contain normal elastin fibers, but a glycoprotein microfibrils network [54]. The Wharton's jelly is surrounded by an amniotic epithelium layer, a membrane that maintains the fluid pressure within the cannular structure of the extracellular matrix, increasing the resistance to compression of the umbilical vessels [21]. The amount of Wharton's jelly, the degree of coiling and other umbilical cord abnormalities such as one umbilical artery, nuchal cord entanglement and knots, have been investigated as risk factors in several studies [46, 145, 172].

The umbilical vessels have a different composition compared to other vascular structures. The umbilical arteries and vein do not contain nerves, a vasa vasorum network and the normal adventitia found in other cardiovascular vessels [47, 150]. However, the umbilical vessels are attached to the Wharton's jelly matrix by bundles of collagen fibers [189], which may perform the load bearing function of an adventitia [47]. The media layer of the umbilical vein contains circularly arranged smooth muscle cells, elastin, and collagen fibers similar to other venous tissue [123], and a single layer of endothelial cells at the lumen surface. The umbilical arteries do not have an internal elastic lamina and contain little elastin, while the vein contains an elastic sub-intimal layer. However, the umbilical artery media is rich in smooth muscle cells which may counter the need for a substantial elastin content [47, 171]. In depth studies on the micro structure and composition of umbilical cord tissues can be found in Bańkowski [7], Bańkowski et al. [8], Franc et al. [54], Li et al. [123], Nanaev et al. [144] and Vizza et al. [189].

Chapter 3

Methodology

In the initial part of this chapter, the governing equations for fluids and solid structures will be presented, formulated in a continuum mechanical framework with special emphasis on blood flow and vascular mechanics. Furthermore, solution procedures and other important considerations for the coupled FSI problem will be discussed. FSI analysis of blood vessels comes with some specific challenges. The interaction between the fluid and solid is in most cases considered strong, which implies that a minor change of state in either the fluid or solid will have a significant effect on the other. This can be attributed to the incompressibility of blood, the softness of the surrounding vessels and the almost equal density between blood and cardiovascular tissue [186].

The derivation of the 1D governing equations for blood flow in compliant vessels, will be presented in the last section of this chapter. The derivation is indented as a background the 1D network model developed in this thesis (see chapter 9) for applications in fetal flows.

Only an overview of the most important mechanical and numerical concepts will be included in this chapter, hence the interested reader is refereed to the references for in-depth explanations and derivations.

3.1 Governing equations

3.1.1 Kinematics and deformation

Some important concepts of kinematics and deformation will be outlined in this section, which will be used in the following discussion on fluid and structural mechanics. Consider a fluid filled deformable vessel as illustrated in Fig. 3.1. The vessel is represented by Ω_s with boundary surface S_s. The fluid contained by the vessel is given by Ω_f with boundary surface S_f. The wet surface shared by the fluid and solid, i.e. the fluid-structure interface, is given by $S_l = S_f \cap S_s$. The vessel and fluid, initially at rest in a reference configuration at time t_0, receive an inflow Q which causes deformation and fluid flow at time t. Furthermore, the concept of an arbitrary

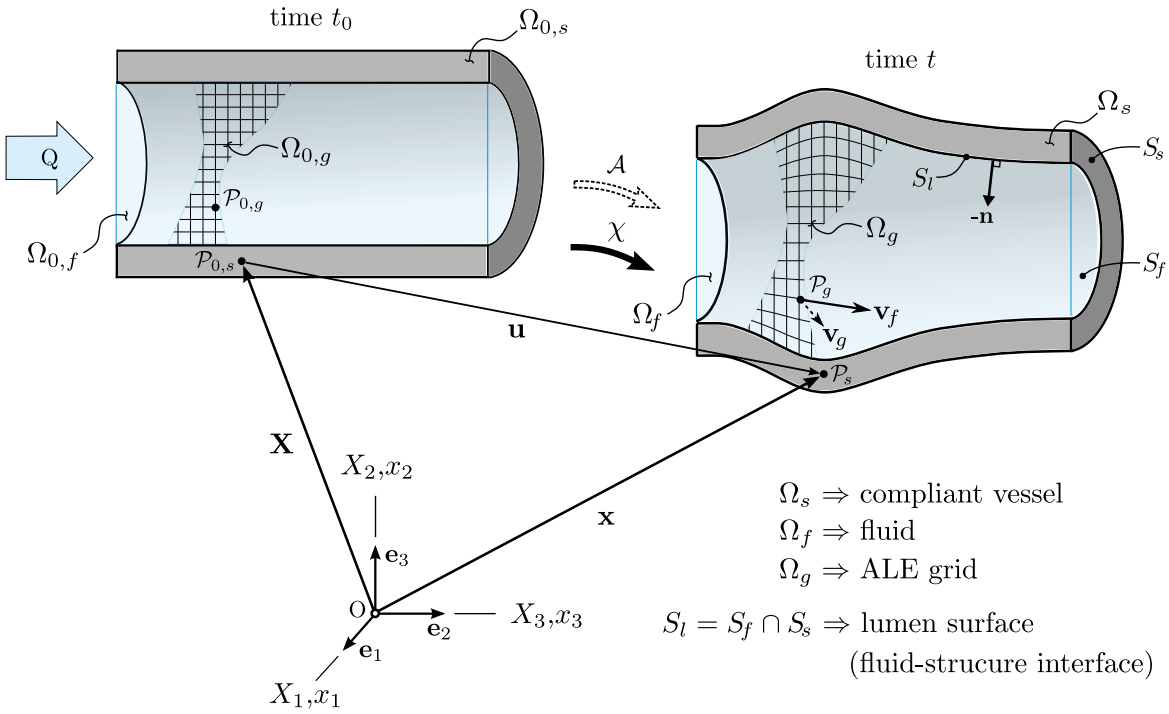

Figure 3.1 Illustration of fluid filled compliant vessel. *To the left*: an initial configuration at time t_0, with a solid $\Omega_{0,s}$, a fluid domain $\Omega_{0,f}$ and a fluid grid $\Omega_{0,g}$, where a flow volume Q enters the fluid domain. *To the right*: a current configuration at time t, given by a deformed solid Ω_s, a deformed fluid domain Ω_f, and a deformed fluid grid Ω_g. The surface of the fluid and solid is given by S_f and S_s respectively, and S_l is the fluid-structure interface with unit normal vector $\mathbf{n}$. The motion χ specifies the current positions $\mathbf{x}$ from $\mathbf{X}$ at time t in the structural domain, $\mathbf{x} = \chi(\mathbf{X}, t) \in \Omega_s$. The motion $\mathcal{A}$ (for an arbitrary Lagrangian-Eulerian formulation) specifies the current positions $\mathbf{x}$ from $\mathbf{X}$ at time t in the fluid grid, $\mathbf{x} = \mathcal{A}(\mathbf{X}, t) \in \Omega_g$. A fluid velocity is given by $\mathbf{v}_f = \mathbf{v}(\mathbf{x}, t)$ for $\mathbf{x} \in \Omega_f, \Omega_g$. A grid velocity is given by $\mathbf{v}_g = \mathbf{v}(\mathbf{x}, t)$ for $\mathbf{x} \in \Omega_g$.

Lagrangian-Eulerian (ALE) grid for the solution of the fluid equations is included in Fig. 3.1. The initial ALE grid $\Omega_{0,g}$ at time t_0 deforms to Ω_g at time t.

Consider an initial (reference) $\Omega_{0,s}$ and a deformed (current) Ω_s configuration of the vessel given in Fig. 3.1, and the transformation map χ, which describes the transformation from a reference location $\mathbf{X} \in \Omega_{0,s}$ of a particle $\mathcal{P}_{0,s}$ to a current position $\mathbf{x} = \chi(\mathbf{X}) \in \Omega_s$ of a particle $\mathcal{P}_s$. From this map, the deformation gradient tensor is defined as

$$\mathbf{F}(\mathbf{X}) = \frac{\partial \chi(\mathbf{X})}{\partial \mathbf{X}} = \frac{\partial \mathbf{x}}{\partial \mathbf{X}}. \tag{3.1}$$

The deformation gradient tensor $\mathbf{F}$ takes into account large deformations and rotations, and the Jacobian $J(\mathbf{X}, t) = \det(\mathbf{F})$ quantifies the local volumetric change around $\mathcal{P}_{0,s}$ given by the motion χ. Hence, an incompressible material requires $J = 1$. Given the deformation gradient tensor, it is convenient to define the strain measures; the right and left Cauchy-Green deformation tensors, $\mathbf{C} = \mathbf{F}^T\mathbf{F}$ and $\mathbf{b} = \mathbf{F}\mathbf{F}^T$, which are symmetric and positive definite

[81]. The displacement of a reference particle $\mathcal{P}_{0,s}$ to a current position $\mathcal{P}_s$ is given by the displacement field

$$\mathbf{u}(\mathbf{x},t) = \mathbf{U}(\mathbf{X},t) = \mathbf{x}(\mathbf{X},t) - \mathbf{X}, \tag{3.2}$$

where the material description of the displacement field $\mathbf{U}(\mathbf{X},t)$ coincides with the spatial description of the displacement field $\mathbf{u}(\mathbf{x},t)$ [81].

Given a spatial velocity $\mathbf{v}(\mathbf{x},t)$, for example in the fluid domain as seen in Fig. 3.1 (where $\mathbf{v}_f(\mathbf{x},t) = \mathbf{v}(\mathbf{x},t) \in \Omega_f$), the velocity gradient tensor is defined by

$$\mathbf{l}(\mathbf{x},t) = \frac{\partial \mathbf{v}(\mathbf{x},t)}{\partial \mathbf{x}} = \nabla \mathbf{v}(\mathbf{x},t). \tag{3.3}$$

From which the rate of deformation tensor is given by

$$\mathbf{d} = \frac{1}{2}(\mathbf{l} + \mathbf{l}^T), \tag{3.4}$$

which is frequently used in fluid mechanisms formulations because of its spatial reference frame [52].

3.1.2 A fluid formulation for blood flow

Blood is composed of cells suspended in a liquid called plasma. Plasma, normally makes up 55% of the total blood volume and contains 91.5% water, 7% proteins and other 1.5% other solutes [170]. The remaining blood volume contains different types of cells, where red blood cells are the most abundant. Generally, blood behaves as a non-Newtonian fluid due to the high cell content. However in the larger arteries and veins blood may be considered a Newtonian fluid, an assumption which does not hold for e.g. capillaries where the vessel lumen and red blood cells are similar in size [57]. Furthermore, because of the high water content in plasma and within in blood cells, blood may be considered an incompressible fluid. In the reminder of this thesis, blood will be considered a Newtonian incompressible fluid.

The flow of an incompressible fluid is governed by the conservation of mass and the incompressible Navier-Stokes equations, which may be presented as

$$\left.\begin{aligned} \nabla \cdot \mathbf{v}_f &= 0 \\ \rho_f \left(\frac{\partial \mathbf{v}_f}{\partial t} + \mathbf{v}_f \cdot \nabla \mathbf{v}_f - \mathbf{f}_f \right) + \nabla \cdot \boldsymbol{\sigma}_f &= \mathbf{0} \end{aligned}\right\} \quad \text{in } \Omega_f, \tag{3.5}$$

where $(\bullet)_f = (\bullet) \in \Omega_f$ and ρ_f is the fluid density and $\mathbf{f}_f$ includes body forces. Furthermore, in Eq. 3.5 one can recognize the material derivative $\dfrac{\mathrm{d}\mathbf{v}_f}{\mathrm{d}t} = \dfrac{\partial \mathbf{v}_f}{\partial t} + \mathbf{v}_f \cdot \nabla \mathbf{v}_f$ of the flow velocity field $\mathbf{v}_f$. For Newtonian fluids with dynamic viscosity μ the Cauchy stress tensor $\boldsymbol{\sigma}_f$ is defined by

$$\boldsymbol{\sigma}_f = -p_f \mathbf{I} + 2\eta \mathbf{d}_f \tag{3.6}$$

where $\mathbf{d}_f$ is the rate of deformation tensor (Eq. 3.4), p_f is the fluid pressure and $\mathbf{I}$ is the identity tensor.

3.1.3 A structural formulation for soft tissue

Structural deformation determined from conservation of momentum in a material description, reads

$$\rho_s \left(\frac{\mathrm{d}^2 \mathbf{u}_s}{\mathrm{d}t^2} - \mathbf{f}_s \right) - \nabla \cdot \boldsymbol{\sigma}_s = \mathbf{0} \quad \text{in } \Omega_s, \tag{3.7}$$

for $(\bullet)_s = (\bullet) \in \Omega_s$, where ρ_s is the solid density; $\mathbf{u}_s$ is the displacement field (Eq. 3.2); $\mathbf{f}_s$ includes body forces; and $\boldsymbol{\sigma}_s$ is the Cauchy stress tensor. The Cauchy stress tensor $\boldsymbol{\sigma}_s$ may be defined by

$$\boldsymbol{\sigma}_s = \frac{1}{J} \mathbf{F} \mathbf{S} \mathbf{F}^T, \tag{3.8}$$

where J is the Jacobian of the deformation gradient tensor $\mathbf{F}$ (Eq. 3.13) and $\mathbf{S}$ is the second Piola-Kirchhoff stress tensor [90].

The elastic (passive) structural response of soft tissue is mainly governed by elastin and collagen fibers [56], and a nearly incompressible bulk behavior [32]. The stress-strain response is non-linear predominantly due to the wavy nature of collagen fibrils in the unloaded state, and the progressive recruitment of fibers for increased strain. Moreover, vascular tissues are most often anisotropic due to preferred fiber orientations [83]. Hyperelasticity offers a nonlinear constitutive framework suitable for describing the structural response vascular tissues. A hyperelastic material assumes the existence of a thermodynamic energy potential Ψ (Helmholtz free-energy function) [59], from which the second Piola-Kirchhoff stress, and other stress measures can be defined. For an incompressible hyperelastic material, the second Piola-Kirchhoff stress may be presented as

$$\mathbf{S} = -p_s \mathbf{C}^{-1} + 2 \frac{\partial \Psi(\mathbf{C})}{\partial \mathbf{C}}, \tag{3.9}$$

where p_s is a scalar which can be interpreted as a hydrostatic pressure. The energy potential Ψ is evaluated as a function of the Cauchy-Green deformation tensor $\mathbf{C} = \mathbf{F}^T \mathbf{F}$, however other strain measures are also applicable [81]. Substitution of the second Piola-Kirchhoff stress for a hyperelastic material Eq. 3.9 into the Cauchy stress Eq. 3.8, gives

$$\boldsymbol{\sigma}_s = -p_s \mathbf{I} + 2\, \mathbf{F} \frac{\partial \Psi(\mathbf{C})}{\partial \mathbf{C}} \mathbf{F}^T, \tag{3.10}$$

for isohoric deformation $J = 1$ (incompressible solid) [84]. Additionally the relation $\mathbf{C}^{-1} = \mathbf{F}^{-1} \mathbf{F}^{-T}$ has been used.

Both isotropic and anisotropic constitutive models will be considered in this work, which can be realized through an appropriate choice of strain energy function, e.g.

$$\Psi = \Psi(\mathbf{C}, \mathbf{A}_1, .., \mathbf{A}_N) \tag{3.11}$$

where an anisotropic description of collagen fibers in the vessel wall can be included in a set of second-order tensors $\mathbf{A}_1, .., \mathbf{A}_N$ [59, 83]. Other important contributors to the mechanical behavior of vascular tissue, such as viscoelasticity and smooth muscle cell activation will not be included in this work.

3.2 Fluid-solid coupling

3.2.1 Equilibrium and boundary conditions

Appropriate boundaries conditions for the fluid and solid are essential in FSI simulations. At the fluid-structure interface S_l, two conditions must be satisfied, kinematic equilibrium

$$\mathbf{v}_f = \frac{\mathrm{d}\mathbf{u}_s}{\mathrm{d}t}, \tag{3.12}$$

and dynamic equilibrium

$$\boldsymbol{\sigma}_f \cdot \mathbf{n} = \boldsymbol{\sigma}_s \cdot \mathbf{n}, \tag{3.13}$$

for $\mathbf{x} \in S_l$ where $\mathbf{n}$ is a unit vector normal to the fluid-structure interface (Fig. 3.1) [38, 52].

Boundary conditions also needs to be specified on the free fluid and solid surfaces, i.e $S_f \setminus S_l$ and $S_s \setminus S_l$. Displacement boundary conditions will be applied for the free end surfaces of vessel walls in this work. More sophisticated structural boundary conditions may include the influence of surrounding tissue. For example boundary condition for external tissue support which includes both elastic and viscoelastic effects have been presented by Moireau et al. [140] and Crosetto et al. [35]. The non-slip condition for flow at the fluid-structure interface will be utilized in this work. Furthermore, lumped models will be considered, applied at the flow inlets and outlets as uniform pressure boundary conditions. The impedance (frequency dependent resistance) to flow in or in parts of the vascular system can be modeled with lumped descriptions, such the Windkessel model [52, 183].

3.2.2 Computational fluid and solid domains

A material formulation is most often used when solving structural equations for solids, which implies that a discretized point in the solid (grid node) follows the motion of the material. This is convenient because the displacements between local particles in a structure, are usually relatively small. The situation is quite different for fluids, the displacements of fluid particles are in most cases very large. Hence, following the relative motion between fluid particles in space is therefore not very practical from a computational standpoint. An spatial formulation is therefore convenient for fluid mechanical problems, where the computational domain (fluid grid) is stationary and the material, the fluid, moves relative to the domain.

In FSI simulations the fluid domain is required to move with the deforming structure, which presents a challenge for the usual spatial description of computational fluid mechanics. Several approaches have been developed to tackle this problem, e.q. the immersed boundary method and the fictitious domain method. In short, these methods involve a computational domain (grid) for the fluid which is fixed in space and extends beyond the structural grid (i.e. overlapping), where the volume occupied by the fluid follows the deformation of the structure by a functional condition/constraint for the flow variables on fluid-structure interface. For more detailed description for these methods see e.g. Peskin [155] and Glowinski et al. [64].

An alternative approach, is the ALE formulation for fluid flow in moving domains [42, 80]. In the ALE formulation, the fluid grid is allowed to arbitrary move relative to the motion of the fluid itself. This is convenient in an FSI setting, because the local velocity of the fluid grid at the fluid-structure interface can be matched with the local velocity of the structure at the fluid-structure interface. In this way, the motion of the deforming structure can directly determine the shape of the fluid gird. Furthermore, the displacement of the fluid grid can be extended into the fluid domain by method of choice, e.g. spring smoothing [11, 37], so that grid quality for the fluid is maintained (see illustration in Fig. 3.1 for $\Omega_{0,g}$ and Ω_g). The fluid variables (e.g. velocity and pressure) are then conservatively interpolated between the displaced and initial fluid grid [44]. It follows from the above description, that each node in the fluid grid, may have an arbitrary velocity relative to the fluid, except from the nodes on the fluid-structure interface which have the same normal velocity as the neighboring nodes on the fluid-structure interface of the structural grid. The main advantage of the ALE method for FSI applications over the above mentioned methods (immersed boundary and fictitious domain) is increased accuracy near the fluid-structure interface [52].

The governing equations for fluid flow on an arbitrary moving grid is found by reformulating the Navier-Stokes equations in an ALE framework. In practice this means that the local grid velocity needs to be subtracted from the transport contribution in the flow acceleration. The relation between a property β in a reference fluid grid and a spatial fluid grid, may be given by

$$\frac{\partial \beta}{\partial t}_{|\mathcal{A}} = \frac{\partial \beta}{\partial t} + \mathbf{v}_g \cdot \nabla \beta \tag{3.14}$$

where $\mathbf{v}_g$ is the grid velocity and $\frac{\partial \beta}{\partial t}_{|\mathcal{A}}$ is the ALE time derivate [52]. The transformation $\mathcal{A}$ contains the motion of the fluid grid which is matched with the structure at the fluid-structure interface, and adjusted to conserve grid quality inside the fluid domain (illustrated in Fig. 3.1). Recalling the conservation of mass and Navier-Stokes equations (Eq. 3.5), and introducing the ALE transformation (Eq. 3.14). It can be shown that the Navier-Stokes equations in a ALE framework reads

$$\left.\begin{aligned} \nabla \cdot \mathbf{v}_f = 0 \\ \rho_f \left(\frac{\partial \mathbf{v}_f}{\partial t} + (\mathbf{v}_f - \mathbf{v}_g) \cdot \nabla \mathbf{v}_f - \mathbf{f}_f \right) - \nabla \cdot \boldsymbol{\sigma}_f = \mathbf{0} \end{aligned}\right\} \quad \text{in } \Omega_g, \tag{3.15}$$

for $(\bullet)_{g,f} = (\bullet) \in \Omega_{g,f}$, A detailed derivation of Eq. 3.15, can be found in e.g. Formaggia et al. [52] and Donea et al. [42].

3.2.3 Coupling techniques

The coupling of a FSI problem can be tackled with either a monolithic or partitioned approach. In a monolithic approach the fluid and structural equations are solved simultaneously in one equation system [12, 13, 52, 86], which is favorable for the stability of the coupled problem, an especially important feature for strongly coupled FSI problems like blood flow in blood vessels [39]. In the partitioned approach is the fluid and the structural equations solved separately, and

a coupling algorithm is used to transfer forces and deformations between the fluid and the solid [38, 52, 190]. One advantage with the partitioned approach, is that optimized off the shelf black box solvers can be employed for the fluid and structural problems. Furthermore, the partitioned approach will in most cases not loose ground to a monolithic approach with regards to efficiency and stability, if an appropriate coupling approach is used depending on the FSI problem in hand [39, 52].

A partitioned FSI coupling can be solved with both an explicit and implicit strategy. In an explicit formulation, are the fluid and solid problems solved separately a fixed number of times each time-step (usually one). Hence, contrary to an explicit monolithic formulation, an explicit partitioned coupling will not result in equilibrium between the fluid and solid at each time-step. Explicit partitioned approaches will therefore require small time-steps to remain stable in most cases, and are suitable for FSI problems where the mutual interaction between the fluid and solid is weak. A partitioned coupling can be made implicit by Newton-Raphson iterations or by performing coupling iterations between the fluid and structural solver, until convergence (equilibrium) of the coupled problem [38]. An implicit scheme will increase the stability of the coupled problem, which is essential if the mutual interaction is strong. Several implicit partitioned coupling schemes have been investigated in the literature, such as the Jacobi and Gauss-Seidel iteration schemes, Gauss-Seidel with Aitken relaxation and different Newton-Raphson formulations, see e.g. Degroote [38].

A common decomposition of the FSI problem is the Dirichlet-Neumann decomposition. In this approach, the displacement the fluid-structure interface $\boldsymbol{\mathcal{D}}$ is determined by the solution of the structural equations (S), giving $\boldsymbol{\mathcal{D}} = \mathbf{u}_s \in S_l$, for a given stress distribution $\boldsymbol{\mathcal{T}}$ on the fluid-structure interface. The interface stress distribution is determined by the solution of the fluid equations (F), giving $\boldsymbol{\mathcal{T}} = \boldsymbol{\sigma}_f \cdot \mathbf{n} \in S_l$, for a given interface displacement $\boldsymbol{\mathcal{D}}$. In an abstract notation this can be written as

$$\mathsf{F}(\boldsymbol{\mathcal{X}}_f, \boldsymbol{\mathcal{D}}(\boldsymbol{\mathcal{X}}_s)) = \mathbf{0} \tag{3.16}$$

$$\mathsf{S}(\boldsymbol{\mathcal{X}}_s, \boldsymbol{\mathcal{T}}(\boldsymbol{\mathcal{X}}_f)) = \mathbf{0} \tag{3.17}$$

where $\boldsymbol{\mathcal{X}}_f$ contains all flow variables (e.g. pressure, velocity) and $\boldsymbol{\mathcal{X}}_s$ contains all structural variables (e.g. stress, displacement). The time level of the variables are not included in the above notation. Given the Dirichlet-Neumann formulation of the FSI problem in Eqs. 3.16-3.17, a black box flow solver can be represented by the function $\mathcal{F}$, which returns the stress vector

$$\boldsymbol{\mathcal{T}} = \mathcal{F}(\boldsymbol{\mathcal{D}}), \tag{3.18}$$

on S_l for a given displacement $\boldsymbol{\mathcal{D}}$. Similarly, a black box structural solver can be represented by the function $\mathcal{S}$, which returns the displacement

$$\boldsymbol{\mathcal{D}} = \mathcal{S}(\boldsymbol{\mathcal{T}}) \tag{3.19}$$

of S_l for a given interface stress $\boldsymbol{\mathcal{T}}$. The coupled FSI problem may now be set up in a fixed point formulation for the interface displacement

$$\boldsymbol{\mathcal{D}} = \mathcal{S} \circ \mathcal{F}(\boldsymbol{\mathcal{D}}) \tag{3.20}$$

which can be solved with for example an explicit staggered scheme or an implicit Gauss-Seidel iteration scheme. Alternatively, a root finding problem can be formulated

$$\mathcal{R}(\boldsymbol{\mathcal{D}}) = \mathcal{S} \circ \mathcal{F}(\boldsymbol{\mathcal{D}}) - \boldsymbol{\mathcal{D}} = \mathbf{0} \tag{3.21}$$

where $\mathcal{R}$ is a residual operator for the interface displacement, which can be solved with Newton-Raphson iterations.

Given the non-linear system posed by residual operator in Eq. 3.21, the Newton-Raphson iteration update for the interface displacement is given by

$$\boldsymbol{\mathcal{D}}^{k+1} = \boldsymbol{\mathcal{D}}^{k} + (\mathcal{R}'^{k})^{-1}(-\mathcal{R}^{k}). \tag{3.22}$$

The Jacobian $\mathcal{R}'^{k}$ at Newton-Raphson iteration step k is defined as $\frac{\partial \mathcal{R}^{k}}{\partial \boldsymbol{\mathcal{D}}}$, with the residual given by

$$\mathcal{R}^{k} = \mathcal{R}(\boldsymbol{\mathcal{D}}^{k}) = \mathcal{S} \circ \mathcal{F}(\boldsymbol{\mathcal{D}}^{k}) - \boldsymbol{\mathcal{D}}^{k} = \widetilde{\boldsymbol{\mathcal{D}}}^{k+1} - \boldsymbol{\mathcal{D}}^{k}. \tag{3.23}$$

$\widetilde{\boldsymbol{\mathcal{D}}}^{k+1}$ is the intermediate value of the interface displacement given by the black box solvers within each coupling iteration step [38]. The Newton-Raphson iterations within a time-step converge when the tolerance $||\mathcal{R}^{k}|| \leq \varepsilon_0$ is reached, and the solution can be proceed to the next time-step. However, calculation of the exact Jacobian $\mathcal{R}'$ is not possible with inaccessible black box solvers because the Jacobian of $\mathcal{S}$ and $\mathcal{F}$ are then unknown. Additionally, the computational cost of solving Eq. 3.22 each iteration step may be large depending on the degrees of the freedom in the fluid-structure interface. However, the system given in Eq. 3.22 can be solved efficiently with black box solvers if the Jacobian is approximated, as shown by e.g. Degroote et al. [39, 40], Gerbeau and Vidrascu [60] and Vierendeels et al. [187].

A promising Newton-Raphson technique with approximate Jacobians for partitioned FSI coupling has recently been developed by Degroote et al. [39], named IQN-ILS (Interface Quasi-Newton with an approximation for the Inverse of the Jacobian from a Least-Squares model). In the IQN-ILS approach, is the exact Jacobian $\mathcal{R}'$ (in Eq. 3.22) replaced by an approximation for the inverse of the Jacobian (denoted with a hat) giving

$$\boldsymbol{\mathcal{D}}^{k+1} = \boldsymbol{\mathcal{D}}^{k} + \widehat{(\mathcal{R}'^{k})^{-1}}(-\mathcal{R}^{k}). \tag{3.24}$$

Furthermore, Degroote et al. [39] have developed an efficient procedure to directly evaluate the matrix-vector product between the inverse approximate Jacobian and the residual vector, given by
$\widehat{(\mathcal{R}'^{k})^{-1}}(-\mathcal{R}^{k})$. The procedure is based on a technique introduced by Vierendeels et al. [187], to approximate the inverse of the Jacobian based on a particular choice of vectors, i.e. the change in the displacement residual $\Delta\mathcal{R}$ and change in interface displacement $\Delta\widetilde{\boldsymbol{\mathcal{D}}}$. Such that the coupling procedure does not require the solution of the linear system in Eq. 3.24, each Newton-Raphson iteration. Moreover, the matrix-vector product is evaluated with information from previous iteration steps which accelerates convergence, depending on the number of included time-steps and the nature of the FSI problem in hand. For example, information from old time-steps will

not give good estimates for the new interface update, if the deformation between time-steps are to large large. The IQN-ILS coupling approach has been implemented by Degroote [38] in an in-house FSI couping code *Tango*, which will be applied in a 3D FSI study in this thesis. Hence, further numerical details on the IQN-ILS technique are omitted, and the interested reader is referred to the detailed descriptions given in Degroote et al. [39, 40].

3.3 Equations for vascular 1D flow

The vascular system, composed of a network of diverging and converging arteries and veins, may be viewed as system of slender compliant vessels from a systemic point of view (Fig. 3.2). 1D models for compliant vessels are therefore an attractive choice when studying large parts of the vascular system. Although such models simplifies the complex local hemodynamics, they are computationally efficient and can provide much valuable information on e.g. the distribution and propagation of flow, pressure and shear waves in the arterial tree. A significant number of research articles exist in the literature on the subject of 1D models for blood flow, with varying degree of model complexity, see e.g Reymond et al. [161] for an overview.

This section will present the major steps involved when deriving the 1D governing equations for blood flow in compliant vessels. The derivation is performed from the conservation principal of Reynolds' transport theorem as outlined by Hellevik [75], and first presented by Hughes and Lubliner [87].

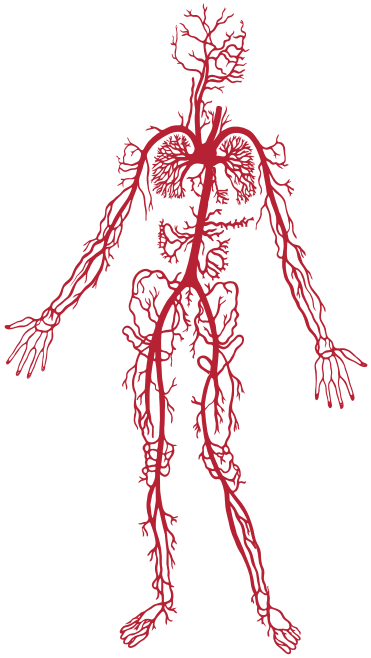

Figure 3.2 The arterial tree. From Solomon et al. [175]

3.3.1 Transport equation

The 1D transport equation will be derived from Reynolds' transport theorem for the spatial and temporal evolution of an intensive property present in a fluid, evaluated in a moving/deformable control-volume [90, 194].

Consider an intensive property $\beta = \beta(\mathbf{x}, t)$ present as a continuous function at a location $\mathbf{x} = \{x, y, z\}$ in a fluid volume $V_f = V_f(t)$ with surface $\partial V_f = \partial V_f(t)$. The fluid is moving though a moving/deformable control-volume $V_c = V_c(t)$, with the shape of a vessel with major axis along the z-axis, as seen in Fig. 3.3. The control-volume surface $S_c = S_c(t)$ is defined by three connected surfaces, two flat end surfaces normal to the z-axis A_1 and A_2, and a lumen surface $S_l = S_l(t)$ which may be considered as the inner wall surface of a deformable vessel, see e.g the fluid-structure interface in Fig. 3.1. Hence, the end surfaces A_1 and A_2 define the in/out-flow faces of the vessel, and we require that their positions are fixed in the z-direction at two arbitrary locations z_1 and z_2. The control-surface for the vessel is therefore given by $S_c = S_l \cup A_1 \cup A_2$, with surface normal $\mathbf{n}$ (Fig. 3.3).

Reynolds' transport theorem for an intensive property β present in the fluid volume V_f, and a moving/deformable control-volume V_c, may be presented as

$$\frac{d}{dt}\int_{V_f} \beta \, dV = \frac{d}{dt}\int_{V_c} \beta \, dV + \int_{S_c} \beta \left(\mathbf{v}_f - \mathbf{v}_c\right) \cdot \mathbf{n} \, dA, \tag{3.25}$$

where $\mathbf{v}_f = \mathbf{v}_f(\mathbf{x}, t)$ is the velocity of the fluid boundary ∂V_f, and $\mathbf{v}_c = \mathbf{v}_c(\mathbf{x}, t)$ is the velocity of the control-surface S_c [75, 90, 194]. The difference between the fluid and control-surface

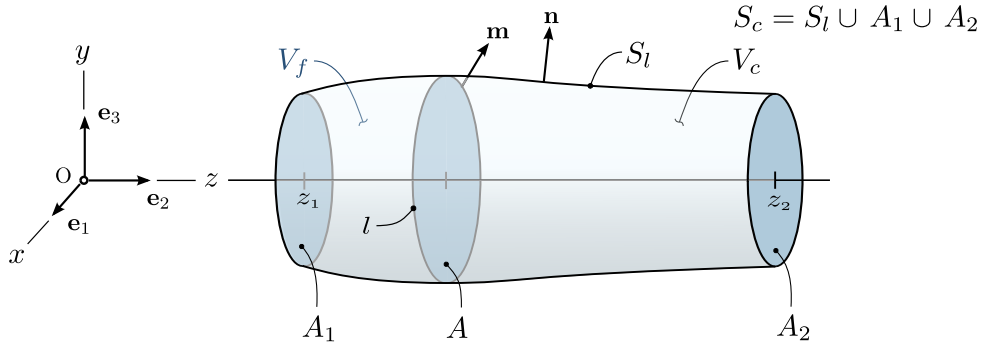

Figure 3.3 Illustration of fluid filled vessel with major axis along the z-axis. The fluid volume is defined by $V_f = V_f(t)$. The vessel volume $V_f = V_f(t)$ acts as a moving/deformable control volume, bounded by the vessel surface $S_c = S_c(t)$ with normal $\mathbf{n}$, which is composed of the end surfaces A_1 at A_2 fixed at positions z_1 and z_2, and the vessel lumen $S_l = S_l(t)$. An internal cross-sectional surface given by $A = A(z,t)$ bounded by the curve $l = l(z,t)$ with outwards normal $\mathbf{m}$, determines the lumen area $A = A(z,t)$.

velocity defines the relative velocity $\mathbf{w} = \mathbf{v}_f - \mathbf{v}_c$.

Quantities evaluated over a cross-sections normal to the z-axis at a position z ($z_1 \leq z \leq z_2$) and time t, will be needed in the following derivation. Hence, we define a cross-sectional area $A = A(z,t) = \int_A dA$, bounded by the curve $l = l(z,t)$ with outwards normal $\mathbf{m}$, as seen in Fig. 3.3. Area-averaged values are defined by

$$\overline{\bullet} = \frac{1}{A} \int_A \bullet \, dA, \tag{3.26}$$

which allows for the following decomposition of volume integrals

$$\int_V \bullet \, dV = \int_{z_1}^{z_2} \left(\int_A \bullet \, dA \right) dz = \int_{z_1}^{z_2} A \, \overline{\bullet} \, dz. \tag{3.27}$$

Decomposition of surface integrals are also needed, given by

$$\int_S \bullet \, dA = \int_{z_1}^{z_2} \left(\oint_l \bullet \, dl \right) dz. \tag{3.28}$$

The left hand term in Eq. 3.25, concerning the intensive property β in the fluid volume V_f, may be redefined as

$$\frac{d}{dt} \int_{V_f} \beta \, dV = \int_{V_f} \dot{\beta} \, dV = \int_{z_1}^{z_2} \left(\int_A \dot{\beta} \, dA \right) dz, \tag{3.29}$$

from the arguments in Irgens [90] where $\dot{\beta}$ is the material derivate of β, and after the introduction of Eq. 3.27. The first term on the right hand side of Eq. 3.25 may be redefined by introducing Eq. 3.27, and by taking into account that the positions of the control-surfaces A_1

and A_2 are independent of time [87], giving

$$\frac{d}{dt}\int_{V_c}\beta\,dV = \int_{z_1}^{z_2}\frac{\partial}{\partial t}(A\overline{\beta})\,dz. \tag{3.30}$$

The surface integral over the control-surface S_c, given in the second term on the right hand side of Eq. 3.25, may be decomposed as follows

$$\int_{S_c}\beta\left(\mathbf{v}_f-\mathbf{v}_c\right)\cdot\mathbf{n}\,dA = \int_{S_l}\beta\left(\mathbf{v}_f-\mathbf{v}_c\right)\cdot\mathbf{n}\,dA + \int_{A_1}\left(\mathbf{v}_f-\mathbf{v}_c\right)\cdot\mathbf{n}\,dA + \int_{A_2}\left(\mathbf{v}_f-\mathbf{v}_c\right)\cdot\mathbf{n}\,dA. \tag{3.31}$$

From the above discussion, we recall that the control-surface velocity is zero ($\mathbf{v}_c = 0$) at A_1 and A_2, and that the fluid velocities are required to only have components in the axial direction at A_1 and A_2, i.e. $\mathbf{v}_f\cdot\mathbf{n} = -v_z$ at A_1 and $\mathbf{v}_f\cdot\mathbf{n} = v_z$ at A_2, where $v_z = v_z(\mathbf{x},t)$. The relations given in Eq. 3.27-3.28 are introduced to Eq. 3.31, which after some manipulation and by the use of the divergence theorem, gives

$$\int_{S_c}\beta\left(\mathbf{v}_f-\mathbf{v}_c\right)\cdot\mathbf{n}\,dA = \int_{z_1}^{z_2}\left(\oint_l\beta w_n\,dl\right)dz + \int_{z_1}^{z_2}\frac{\partial}{\partial z}(A\overline{\beta v_z})\,dz, \tag{3.32}$$

where the relative normal velocity w_n is defined by $w_n = \mathbf{w}\cdot\mathbf{n} = (\mathbf{v}_f-\mathbf{v}_c)\cdot\mathbf{n}$.

The 1D transport equation for a generic property β can now be derived from substitution of Eqs. 3.29, 3.30 and 3.32 into Eq. 3.25, giving

$$\frac{\partial}{\partial t}(A\overline{\beta}) + \frac{\partial}{\partial z}(A\overline{\beta v_z}) + \oint_l\beta w_n\,dl = \int_A\dot{\beta}\,dA, \tag{3.33}$$

where the sums $\int_{z_1}^{z_2}\bullet\,dz$ between the two positions z_1 and z_2, have canceled, as Eq. 3.33 should be true for all positions z_1 and z_2 [75, 87].

3.3.2 Mass conservation

The 1D mass balance is found by letting $\beta = 1$ in the 1D transport equation Eq. 3.33, giving

$$\frac{\partial A}{\partial t} + \frac{\partial}{\partial z}(A\overline{v}_z) + \oint_l w_n\,dl = 0, \tag{3.34}$$

for an incompressible fluid, i.e. $\nabla\cdot\mathbf{v}_f = 0$. The third left hand side term may be considered as a volumetric outflow per unit length, i.e. a permeable vessel wall.

3.3.3 Momentum balance

The 1D momentum balance may now be found from the 1D transport equation Eq. 3.33, by letting $\beta = v_z$, giving

$$\frac{\partial}{\partial t}(A\overline{v}_z) + \frac{\partial}{\partial z}(A\overline{v_z^2}) + \oint_l v_z w_n\,dl = \int_A\dot{v}_z\,dA, \tag{3.35}$$

where an expression for the material derivative of the axial velocity $\dot{v}_z$ is needed. Recalling the incompressible Navier-Stokes equations Eq. 3.5 and the constitutive equation for a Newtonian fluid Eq. 3.6. Furthermore, employing the arguments presented Hughes and Lubliner [87] and the reference therein, e.g. the transverse velocities may be assumed much smaller that the axial velocities, $v_x/v_z \ll 1$ and $v_y/v_z \ll 1$, gives the following result

$$\dot{v}_z = -\frac{1}{\rho_f}\frac{\partial p_f}{\partial z} + \frac{\partial}{\partial \alpha}\left(\nu \frac{\partial v_z}{\partial \alpha}\right) + f_z, \tag{3.36}$$

where $\nu = \eta/\rho_f$ is the dynamic viscosity; f_z includes body forces; α is a repeated index to be summed over x, y and z [87]. From substitution of Eq. 3.36 into the momentum balance Eq. 3.35 and employing Eq. 3.27-3.28 and the divergence theorem, we now find the 1D momentum balance

$$\frac{\partial}{\partial t}(A\overline{v}_z) + \frac{\partial}{\partial z}(A\overline{v_z^2}) + \oint_l v_z w_n \, dl = -\frac{A}{\rho_f}\frac{\partial}{\partial z}(\overline{p}_f) + \oint_l \left(\nu \frac{\partial v_z}{\partial m}\right) dl + A\,\nu\overline{\frac{\partial^2 v_z}{\partial z^2}} + A\overline{f}_z, \tag{3.37}$$

where $\mathbf{m} = [m_x, m_y, 0]$ is the outwards normal to l (Fig. 3.3) [75, 87].

3.3.4 1D equations for a compliant vessel

The conservation of mass Eq. 3.34 and the momentum balance Eq. 3.37, represents the general form of the governing 1D equations for flow in a compliant vessel. A reduced form may be derived if body forces and the contribution $\overline{\frac{\partial^2 v_z}{\partial z^2}}$ are neglected, the permeability is set to zero $w_n = 0$, $p = \overline{p}_f$, $v = \overline{v}_z$ and a circular cross section is assumed;

$$\frac{\partial A}{\partial t} + \frac{\partial Av}{\partial z} = 0 \tag{3.38}$$

$$\frac{\partial Av}{\partial t} + \frac{\partial A\overline{v_z^2}}{\partial z} + \frac{A}{\rho_f}\frac{\partial p}{\partial z} = \frac{2\pi R}{\rho_f}\tau_z \tag{3.39}$$

$$A = A(p, z, t) \tag{3.40}$$

where $R = \sqrt{A/\pi}$ is the radius of the vessel, and viscous shear stress is given by $\tau_z = \mu[\frac{\partial v_z}{\partial r}]_{r=R}$. The system Eq. 3.38-3.39 is closed by the introduction of a constitutive relation Eq. 3.40 between the cross-sectional area A and lumen pressure p.

The distribution of the axial velocity $v_z = v_z(\mathbf{x}, t)$ in the vessel cross-section, i.e. the velocity profile, is not yet discussed. One possibility is to assume an axisymmetrical velocity profile $\phi(r)$ which only depends on the radial coordinate r, with the requirement $\int_A \phi(r)\, da = A$. Such that the axial velocity may be decomposed as $v_z = \phi(r)\, v$. In this case, terms in Eq. 3.38-3.39 which include the axial velocity v_z needs to be reevaluated according to

$$\overline{v_z^2} = v^2\,\frac{1}{A}\int_A \phi(r)^2 dA, \tag{3.41}$$

$$\tau_z = \mu\,\left[\frac{\partial v_z}{\partial r}\right]_{r=R} = \mu\, v\,\left[\frac{d\phi(r)}{dr}\right]_{r=R}. \tag{3.42}$$

Other assumptions about the velocity profile is also possible, e.g. an assumed Stokes layer or Womersley theory. An overview and comparison of different approaches for velocity profiles approximation can be found in van de Vosse and Stergiopulos [183].

3.4 Discretization

The discretization of 3D fluid and structural models, will in this work be handled by commercial black box solvers. The finite volume method will be used for the fluid equations and the finite element method will be used for the structural equations. Details in on these discretization techniques will not be included in this work, and the reader is referred to standard textbooks on this issue [19, 148, 185].

The equations for 1D flow in compliant vessels will be discretized with the explicit MacCormack method [5, 125], and the details of the discretization of the 1D model is given in chapter 9.

Chapter 4

Summary of appended papers

Paper 1 (chapter 6)

Structural modeling of the intra abdominal umbilical vein and the ductus venosus
Leinan P.R., L.R. Hellevik, V. Prot, T. Kiserud and B.H. Skallerud
Parts of this work have been published in Leinan et al. [120]
An isotropic hyperelastic non-linear constitutive model and parameters for the intra abdominal umbilical vein and the ductus venosus are presented, based on inflation test data from fetal sheep. Additionally, a method for parameter estimation is outlined, by enforcing cross-sectional equilibrium of a cylindrical vessel segment, and employing the mean value theorem.

Paper 2 (chapter 7)

Structural properties and constitutive modeling of the human umbilical vein and Wharton's jelly
Leinan P.R., V. Prot, C.N. van den Broek, T. Kiserud, C. Vogt, B. Skallerud, F.N. van de Vosse and L.R. Hellevik
Submitted 2012 for journal publication
A fiber dispersion model and parameters are presented for the human umbilical vein and surrounding Wharton's jelly, and analyzed with a 3D finite element model. Experimental *in vitro* inflation-extension tests are performed on nine human umbilical cord specimens, and the constitutive model parameters are fitted to the inflation-extension data through an inverse optimization algorithm.

Paper 3 (chapter 8)

Velocity profiles in the human ductus venosus: a numerical fluid structure interaction study
Leinan P.R., J. Degroote, T. Kiserud, B. Skallerud, J. Vierendeels and L.R. Hellevik
Accepted for publication in Biomechanics and Modeling in Mechanobiology
A 3D FSI study is presented on hemodynamics in the fetal intra abdominal umbilical vein, ductus venosus and left portal vein bifurcation, with lumped model boundary conditions. The primary aim of the study is to investigate velocity profiles at the inlet of the the ductus venosus

under normal conditions in the later stages of gestation, aimed at volumetric flow rate assessment with Doppler velocimetry.

Paper 4 (chapter 9)

A one-dimensional vascular network model, for applications in the feto-placental circulation Leinan P.R. and L.R. Hellevik
A 1D vascular network model is developed aimed at applications in the feto-placental circulation. The network model is derived from the governing equations for 1D flow in compliant vessels, and discretized with the explicit MacCormack scheme. The system characteristics (Riemann variables) are determined and formulated in a linearized form, and used to impose boundary conditions, lumped models and network connections.

4.1 Declaration of authorship

In paper 1, Paul Roger Leinan implemented the theory and performed the numerical simulations. The inflation test data was provided by Hellevik et al. [76]. In paper 2, Paul Roger Leinan implemented the parameter optimization algorithm and extended the numerical implementation of the constitutive model from Prot and Skallerud [156], to include a fiber dispersion model for fetal veins. Paul Roger Leinan performed the experimental testing and modified the inflation-extension test setup, provided by the group of Frans N. van de Vosse at the department of Biomedical engineering at Eindhoven University of Technology (the Netherlands), to include static inflation-extension testing of fetal veins. In paper 3, Paul Roger Leinan build the model, implemented boundary conditions and performed the numerical simulations. The FSI coupling code *Tango*, implemented by Joris Degroote [38], was provided by the group of Jan Vierendeels at the Department of Flow, Heat and Combustion Mechanics at Ghent University (Belgium). In paper 4, Paul Roger Leinan implemented the theory and performed the numerical simulations.

In papers 1, 2, 3 and 4, Paul Roger Leinan wrote the manuscripts. The co-authors contributed constructive criticism that increased the scientific quality of the papers.

Chapter 5

Conclusions and directions for further work

5.1 Conclusions

In this study, mechanical modeling and experimental testing have been carried out on veins in the fetal venous return. The main aim of the work has been to bring forward numerical models, concerning FSI of hemodynamic phenomena in fetal flows. Such models have the potential to enhance understanding of underlying causes in physiology and pathology, and to enable the development of new clinical procedures.

An isotropic hyperelastic model is employed for the intra abdominal umbilical vein and the ductus venosus (chapter 6), and fitted to *in vitro* inflation test data given by Hellevik et al. [76] from fetal sheep fetuses. We therefore provide a first estimate for a constitutive model and parameters suitable for finite element analysis for intra abdominal umbilical vein and the ductus venosus, for which only a simplified compliance model has been considered before [76]. A close fit is observed between the proposed hyperelastic model and the compliance seen in the experimental data by Hellevik et al. [76], when compared in finite element simulations. However, considerable variance exists in the model parameters.

We introduced a hyperelastic fiber dispersion model for the combined response of the umbilical vein and surrounding Wharton's Jelly (chapter 7), similar to anisotropic models often used in arterial mechanics [59, 118, 184]. We fitted the fiber dispersion model to experimental data from *in vitro* inflation-extension test on human umbilical veins, performed within this thesis. A detailed structural model for umbilical veins is missing in the literature, and experimental data on this vascular tissues are scares [47]. The model describes the radial expansion and change in the reduced axial force seen in the inflation-extension tests reasonably well. Moreover, our model indicate that the main fiber angle for the combined response of the umbilical vein and surrounding Wharton's Jelly is aligned with the circumferential direction of the umbilical vein. However, considerable variance exists in the model parameters.

We developed a mathematical model to assist the clinical assessment of volumetric flow rate through the ductus venosus (chapter 8). The model employs 3D FSI simulations of the bifurcation formed by the intra abdominal umbilical vein, the ductus venosus and the left portal vein, with lumped model boundary conditions for the major surrounding veins. The compliance of

the veins are modeled with the isotropic hyperelastic materials derived in chapter 6. Our model, compared to previous models in the literature of the ductus venosus bifurcation [77, 151], takes into account the compliance of the veins and lumped boundary models. Velocity profile shape coefficients at the inlet of the ductus venous are evaluated in a parametric study, based on a reference case for a human fetus at 36 weeks of gestation. The velocity profile shape coefficient at the inlet of the ductus venous is found to be 0.69 ± 0.02, which confirms previous studies in the literature, based on steady flow and rigid walls by Pennati et al. [151] and Doppler velocimetry measurements by Kiserud et al. [115]. Additionally, CFD simulations with rigid walls performed in the current study (chapter 8), produced only minor differences in the velocity profiles compared to the FSI simulations. Hence, our results indicate that wall compliance does not significantly alter velocity profile predictions in the ductus venous bifurcation, and that rigid wall CFD simulations as performed by Pennati et al. [151], may be sufficient for predicting velocity profile coefficients for clinical flow assessments in the ductus venous. The presented numerical model is a promising tool for accurate, practical and non-invasive prediction of volumetric flow rate through the ductus venosus by Doppler ultrasound in a clinical setting, with possibilities for extension to other veins in the feto-placental circulation.

We developed a 1D vascular network model, aimed for applications in the feto-placental circulation (chapter 9). The model is derived from the governing equations for 1D flow in compliant vessels and discretized with the explicit MacCormack scheme. Boundary conditions are imposed in a characteristics manner by the linearized Riemann variables. By employing the linearized Riemann variables we avoid the need for an explicit form of the Riemann variables by full integration, which may be considered the more common approach [3, 50, 143, 169]. Integration of the Riemann variables is not always possible, and depends on the choice of constitutive models for the vessels compliance. Moreover, we show that the Riemann variables linearized around the previous time-step incorporates well in the explicit MacCormack scheme. A flexible framework for the imposition of flow (and pressure) boundary conditions is outlined such that reflection points at the flow inlet/outlets may be accounted for, e.g. to model reflection from the ventricle and aortic valve while at the same time, allow for flow to be ejected into the vascular system. The proposed formulation for imposition of boundary conditions means that complex lumped models may also be incorporated with ease e.g. Windkessel models, as shown in the current work.

5.2 Directions for future work

Experimental data on human fetal veins, especially within the fetal body such as the intra abdominal umbilical vein and the ductus venosus, are not easily accessible and little data is available in the literature. However, knowledge on the structural response of fetal veins is essential in FSI studies, both for 3D and 1D models. Further detailed experimental studies on the structural response of fetal veins (and arteries) are therefore called for. Studies on animal models is a viable option as shown by Hellevik et al. [76], from which the results can be compared to human fetal conditions by means of non-invasive techniques.

The combined structural response of human umbilical vein and surrounding Wharton's Jelly have been investigated within this thesis in inflation-extension tests, and subsequently modeled with a fiber dispersion model. However, the morphology of the umbilical vein differs significantly from the Wharton's Jelly, hence separate evaluation of the two tissues is an interesting prospect for further experimental testing and structural modeling, as shown by Pennati [150]. Moreover, the detailed orientation and distribution of collagen fibers (and other fibrous tissue content) in the umbilical vein and in the Wharton's Jelly, is largely unknown in the literature. Hence, studies on the detailed distribution of collagen fiber in the umbilical vein and in the Wharton's Jelly are called for.

Velocity profile shape coefficients at the inlet of the ductus venosus are investigated in this thesis with a 3D FSI and CFD model of the bifurcation formed by the intra abdominal umbilical vein, the ductus venosus and the left portal vein. Moreover, lumped models are used as boundary conditions for the in/out-flow faces of the 3D FSI domain. Hence, a large number of model assumptions and parameters are included in the current modeling approach, for example the compliance of the veins derived from limited experimental data on fetal sheep fetuses (chapter 6) [76]. Hence, further investigations on the impact of model configuration and input parameters are needed, to increase the confidence of velocity profile predictions in the ductus venosus over a wider physiological and pathological range. Moreover, only minor differences in the velocity profiles are found between the FSI and CFD models in the current study. However, more significant differences between FSI and CFD are found in other hemodynamical parameters such as flow rate distribution and velocity pulsation indices's. Further studies are therefore called for to determined the influence on wall compliance for abnormal/diseased conditions, e.g. high ductus venosus pulsations, reversed flow and increased wall compliance.

At the present time, 3D FSI models are both computational expensive and time consuming to develop. We therefore developed a 1D network model for blood flow in compliant vessels, aimed at applications in the feto-placental circulation. The 1D network model is a promising tool for studies on systemic flow and pressure distribution in the vascular tree, and fetal hemodynamics phenomena such as the propagation of pressure and flow waves from the fetal heart and into the umbilical circulation. Furthermore, an interesting prospect for further studies is a simulation environment where the 3D and 1D FSI models can be combined. Such that complex local hemodynamics can be addressed with 3D FSI at a region of interest, with the 1D network model as boundary condition to account for a larger part of the vascular tree with low computational cost [25, 49, 146].

Part II

Research papers

Chapter 6

Structural modeling of the intra abdominal umbilical vein and the ductus venosus

Parts of this chapter was published in

MekIT'09: Fifth National Conference on Computational Mechanics, Trondheim
2009 May: p.281-295
On material modeling of the umbilical vein
P.R. Leinan, L.R. Hellevik, V. Prot, T. Kiserud and B.H. Skallerud

6.1 Introduction

In this work, we present a first estimate for a constitutive model and parameters for the intra abdominal umbilical vein (IVU) and the ductus venosus (DV) based on experimental inflation test data from fetal sheep. Additionally, a method for parameter estimation is outlined, by enforcing cross-sectional equilibrium of a cylindrical segment, and employing the mean value theorem.

Experimental data on the compliance of fetal veins are scares in the literature [47], with some notable exceptions for the human cordal umbilical vein (UV) presented by Daniel et al. [36], Li et al. [121, 122], Pennati [150], and on the IUV and DV of fetal sheep given by Hellevik et al. [76]. Our aim in this study, is to investigate a structural model suitable for finite-element analyses of the IUV and DV, previously used in the description of arterial wall mechanics [59, 147]. The constitutive model is derived from a stored strain energy potential for a hyperelastic isotropic material, with three material parameters. The strain energy potential contains an exponential and a Neo-Hookean term which are functions of the first invariant of the right Cauchy-Green tensor. The Neo-Hookean term is included to describe elastic behavior in the low pressure region, when elastin is the most prominent load bearing constituent. The stiffening effect found in most vascular tissues in the high pressure region caused by increasing recruitment of collagen fibers is modeled by the exponential term [83]. Moreover, the chosen form of exponential term can be considered to model an isotropic distribution of collagen fibers [59].

Available experimental data from Hellevik et al. [76] will be employed to determined model parameters. Hellevik et al. [76] investigated the compliance of the IUV and DV from fetal sheep in *in-vitro* inflation tests, i.e. the change in the internal diameter as a function of lumen pressure. However, the thicknesses of vein walls were not quantified by Hellevik et al. [76]. Vascular tissue can be assumed nearly incompressible [32], hence the deformation of the vein walls can be determined if the unloaded wall thicknesses are known (effects from residual stress and axial stretch [31, 34], will not be considered here). Approximate values for the wall thicknesses will be included in the current work from a morphological study by Ailamazyan et al. [2], on the human IUV and DV.

Material parameters are determined with the non-linear least squares (LS) technique, from comparing static equilibrium of a pressurized cylindrical cross-section [34, 83], and the inflation data from Hellevik et al. [76]. Cross-section equilibrium is evaluated by employing the mean value theorem, which is solved for in an iterative procedure between LS optimization and a finite-element (FE) model [120].

6.2 Materials and methods

6.2.1 Compliance and unloaded geometry

The compliance of the fetal sheep IUV and DV near term, have been measured by Hellevik et al. [76] in *in-vitro* inflation tests. The transmural pressure p_i was adjusted in decreasing steps

with a saline column, from an experimentally defined sample specific maximum pressure level [76]. The inner vein diameter d_i was measured with an ultrasound transducer as the average of five or more measurements, when the transmural pressure p_i had stabilized within each stepwise decrease. Compliance data on four IVU and four inlet DV samples are provided by Hellevik et al. [76] for the purpose of constitutive modeling in the current work. For more details on the experimental protocol see Hellevik et al. [76]. The lumen radius at approximately zero transmural pressure, is accepted as the unloaded inner radii R_i for each individual IUV and DV sample (from Hellevik et al. [76]) in the current work, i.e. $R_i = d_i/2$ at $p_i \approx 0$. Furthermore, the small transmural pressures (≈ 0.7 mmHg) present in the experimental data at the assumed unloaded states are for convenience subtracted from all the pressure data points for each sample. An assumption for the wall thicknesses of the veins is also needed, to fit the constitutive model to the compliance data. Ailamazyan et al. [2] gives an average wall thickness of 0.26 mm for eighth IUV samples and 0.12 mm at the inlet of the DV for nine samples, in a morphological study on human fetuses between 20 and 40 weeks of gestation. The averaged wall thickness data given by Ailamazyan et al. [2] are accepted as an approximation for the unloaded wall thickness H (Fig. 6.1), of the IUV and DV in the current study. From these wall thickness data, approximate radius-thickness ratios R_i/H are determined, from the average unloaded inner radii R_i data for the fetal sheep IUV and DV samples provided by Hellevik et al. [76] (see Table 6.1). Hence, the model parameters will be determined from the compliance data provided by Hellevik et al. [76], on four IUV samples with equal radius-thickness ratio $R_i/H = 7.0$, and four DV samples with equal radius-thickness ratio $R_i/H = 6.7$.

6.2.2 Equilibrium and kinematics

The Cauchy equation equations of motion, reduces to

$$\nabla \cdot \boldsymbol{\sigma} = \mathbf{0}, \tag{6.1}$$

when body forces and accelerations are excluded [90]. Equilibrium in the radial direction r is given by

$$\frac{d\sigma_{rr}}{dr} + \frac{(\sigma_{rr} - \sigma_{\theta\theta})}{r} = 0, \tag{6.2}$$

in cylindrical coordinates when shear-stresses are neglected. Hence, cross-sectional equilibrium is determined by the radial σ_{rr} and circumferential $\sigma_{\theta\theta}$ Cauchy stress components. Integration of Eq. 6.2, given a deformed cylinder cross-section (Fig. 6.1), with inner radius r_i, outer radius r_o, an internal pressure $p_i = -\sigma_{rr}|_{r=r_i}$ and an external pressure $0 = \sigma_{rr}|_{r=r_o}$, gives

$$p_i = \int_{r_i}^{r_o} \frac{(\sigma_{\theta\theta} - \sigma_{rr})}{r}\, dr, \quad r_i \leq r \leq r_o. \tag{6.3}$$

Furthermore, for isochoric deformation, a material point at a radius r in the deformed cylinder, can be related to the corresponding reference position R through

$$r = \sqrt{\frac{R^2 - R_i^2}{k\lambda_z} + r_i^2}, \tag{6.4}$$

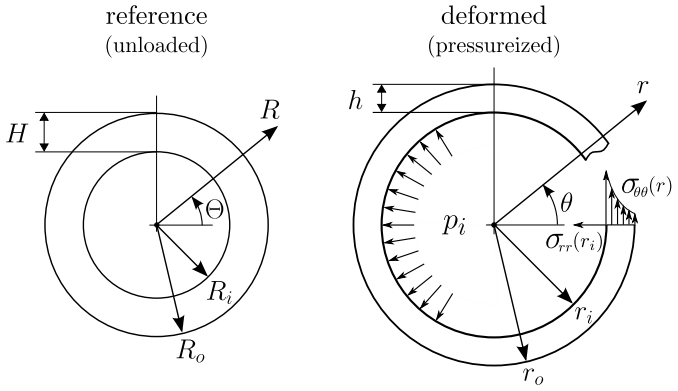

Figure 6.1 Illustration of a cylinder cross-section. In the reference unloaded state with the reference radial R and angular coordinate Θ; wall thickness H; inner radius R_i and outer radius R_0. In the deformed state after pressurization from the uniform lumen pressure p_i, with the radial r and angular θ coordinates; wall thickness h; inner radius r_i and outer radius r_o.

where λ_z is the axial stretch and R_i is the reference radius of the inner cylinder surface. The parameter $k = 2\pi/(2\pi - \alpha)$ is a measure for the opening angle α of the cylinder, see e.g. Holzapfel et al. [83], which can be used to include effects from residual strains (neglected in the current study, i.e $\alpha = 0\,\text{rad}$). The stretches in the circumferential and radial direction are defined by

$$\lambda_\theta = \frac{r}{R}, \quad \lambda_r = \frac{R}{r\lambda_z}. \tag{6.5}$$

In the following, measures for the mean circumferential and radial stress over the wall thickness are also required, defined by

$$\bar{\sigma}_{rr} \equiv \frac{1}{h}\int_{r_i}^{r_o} \sigma_{rr}(r)\, dr, \tag{6.6}$$

$$\bar{\sigma}_{\theta\theta} \equiv \frac{1}{h}\int_{r_i}^{r_o} \sigma_{\theta\theta}(r)\, dr, \tag{6.7}$$

where $h = r_o - r_i$ is the deformed cylinder wall thickness.

6.2.3 Constitutive model

Morphological descriptions of the DV and IUV can be found in the literature, where the DV has been given the most attention [2, 134, 136, 178], and limited information can be found for the IUV [129]. The DV and IUV are described as similar to other venous tissues containing muscular, elastin and collagen fibers. Functions of exponential form are popular for describing the highly non-linear passive stress-strain response of arteries [58, 59, 83, 84], due to the increased

recruitment of collagen fibers for increasing strains. The strain energy function

$$\begin{aligned}\psi &= \tilde{\psi}(I_1) - q(J-1),\\ \psi &= a_1(I_1-3) + a_2(\, e^{a_3\,(I_1-3)^2} - 1) - q(J-1),\end{aligned} \tag{6.8}$$

contains an exponential term with two parameters a_2 and a_3 and a Neo-Hookean term with a single parameter a_1, included to describe elastic behavior in the low pressure region when elastin is considered the primary load bearing element. The scalar q is a Lagrange multiplier introduced to enforce incompressibility, which needs to be determined from boundary conditions [81, 157]. Both the Neo-Hookean and exponential terms are functions of the first invariant

$$I_1 = \lambda_r^2 + \lambda_\theta^2 + \lambda_z^2 = \mathrm{tr}(\mathbf{C}), \tag{6.9}$$

of the right Cauchy-Green tensor, which in our case is limited to the principal stretches

$$\mathbf{C} = \mathbf{F}^T\mathbf{F} = \begin{bmatrix} \lambda_r^2 & 0 & 0 \\ 0 & \lambda_\theta^2 & 0 \\ 0 & 0 & \lambda_z^2 \end{bmatrix}, \tag{6.10}$$

giving the left Cauchy-Green tensor $\mathbf{b} = \mathbf{F}\mathbf{F}^T = \mathbf{C}$. The tensor $\mathbf{F}$ is the deformation gradient, and

$$J = \det(\mathbf{F}) = \lambda_r\lambda_\theta\lambda_z \tag{6.11}$$

is the volumetric ratio, where incompressibility requires $J = 1$. The second Piola-Kirchhoff stress tensor expressed in terms of the strain energy potential ψ (Eq. 6.8), and the right Cauchy-Green tensor $\mathbf{C}$, is given by

$$\mathbf{S} = 2\,\frac{\partial\psi(\mathbf{C})}{\partial\mathbf{C}}. \tag{6.12}$$

Since the strain energy function Eq. 6.8 depends only on I_1 and J, we find the following expression for the second Piola-Kirchhoff stress

$$\mathbf{S} = 2\,\tilde{\psi}_1\mathbf{I} - qJ\,\mathbf{C}^{-1}, \tag{6.13}$$

where

$$\tilde{\psi}_1 = \frac{\partial\tilde{\psi}}{\partial I_1} = a_1 + 2a_2a_3\,(I_1-3)\,e^{a_3\,(I_1-3)^2}, \tag{6.14}$$

Furthermore, the results $J = \sqrt{\det(\mathbf{C})}$, $\frac{\partial\det(\mathbf{C})}{\partial\mathbf{C}} = \det(\mathbf{C})\mathbf{C}^{-1}$ and $\frac{\partial I_1}{\partial\mathbf{C}} = \mathbf{I}$, have been used in the above derivation [81]. The Cauchy stress $\boldsymbol{\sigma}$ is determined from a push forward by the deformation gradient tensor $\mathbf{F}$, giving

$$\begin{aligned}\boldsymbol{\sigma} &= \frac{1}{J}\,\mathbf{F}\mathbf{S}\mathbf{F}^T,\\ &= 2\,\tilde{\psi}_1\mathbf{b} - q\mathbf{I},\\ &= \left[2a_1 + 4a_2a_3\,(I_1-3)\,e^{a_3\,(I_1-3)^2}\right]\mathbf{b} - q\mathbf{I},\end{aligned} \tag{6.15}$$

with $J = 1$, and where $\mathbf{I}$ is the identity tensor [156].

The hyperelastic model given by the strain energy potential in Eq. 6.8 is implemented in a user sub-routine in *Abaqus FEA*, defined by

$$\tilde{\psi} = a_1(I_1 - 3) + a_2(\ e^{a_3\ (I_1-3)^2} - 1), \tag{6.16}$$

and its derivatives,

$$\tilde{\psi}_1 = \frac{\partial \tilde{\psi}}{\partial I_1} \quad \text{and} \quad \tilde{\psi}_{11} = \frac{\partial^2 \tilde{\psi}}{\partial {I_1}^2}.$$

The material model is employed in an axisymmetrical FE model of the IUV and DV, constructed of 20 CAX8RH elements. The cylinder ends of the FE model are clamped in the axial direction and free to move in the radial direction, and a uniform pressure is applied to the inner cylinder surface.

6.2.4 Parameter estimation

The model parameters a_1, a_2 and a_3 (Eq. 6.8) are determined with the LS technique. The LE object function ϵ^2 to be minimized, is expressed as the difference between lumen pressure p_i^{exp} measured during inflation tests and a model lumen pressure p_i^{mod} given by the cross-sectional equilibrium in Eq. 6.3. Hence, the objective function reads

$$\epsilon^2 = \sum_{j=1}^{m} \left(p_{i,j}^{\text{exp}} - p_{i,j}^{\text{mod}}\right)^2. \tag{6.17}$$

where p_i^{mod} is a function of the model parameters a_1, a_2 and a_3, and the deformation measured during the inflation tests for $j = \{1, .., m\}$ pressure levels.

The model pressure p_i^{mod} is determined from the integrated expression for cross-sectional equilibrium of a cylindrical section given in Eq. 6.3, which may be presented as

$$p_i = \int_{r_i}^{r_o} \frac{\sigma(r)}{r}\, dr, \quad r_i \le r \le r_o, \tag{6.18}$$

$$\text{for} \quad \sigma(r) = \sigma_{\theta\theta}(r) - \sigma_{rr}(r), \tag{6.19}$$

Introduction of the mean value theorem into Eq. 6.18, gives

$$p_i = \sigma(\hat{r}) \int_{r_i}^{r_o} \frac{1}{r}\, dr, \quad r_i \le (\ r \text{ and } \hat{r}\ ) \le r_o,$$

$$p_i = \sigma(\hat{r})\ \ln\left(\frac{r_o}{r_i}\right), \tag{6.20}$$

$$\text{for} \quad \sigma(\hat{r}) = \sigma_{\theta\theta}(\hat{r}) - \sigma_{rr}(\hat{r}) \equiv \overline{\sigma}_{\theta\theta} - \overline{\sigma}_{rr}. \tag{6.21}$$

Hence, the radial position $\hat{r}$ in the cylinder wall needs to be determined to find the mean stresses $\overline{\sigma}_{\theta\theta}$ and $\overline{\sigma}_{rr}$. The Cauchy stresses Eq. 6.15 as functions of $\hat{r}$, reads

$$\overline{\sigma}_{rr} = \left[2a_1 + 4a_2a_3\ (\hat{I}_1 - 3)\ e^{a_3\ (\hat{I}_1-3)^2}\right]\ \hat{\lambda}_r^2 - q, \tag{6.22}$$

$$\overline{\sigma}_{\theta\theta} = \left[2a_1 + 4a_2a_3\ (\hat{I}_1 - 3)\ e^{a_3\ (\hat{I}_1-3)^2}\right]\ \hat{\lambda}_\theta^2 - q. \tag{6.23}$$

where $\hat{I}_1$, $\hat{\lambda}_r$ and $\hat{\lambda}_\theta$ are given by Eq. 6.4-6.5 (with $\lambda_z = 1$ and $k = 1$). The model pressure p_i^{mod} can now be determined by substitution of Eq. 6.22-6.23 into Eq. 6.20

$$p_i^{\text{mod}} = \left[2a_1 + 4a_2a_3\ (\hat{I}_1 - 3)\ e^{a_3\ (\hat{I}_1-3)^2}\right]\ [\hat{\lambda}_\theta^2 - \frac{1}{\hat{\lambda}_\theta^2}]\ \ln\left(\frac{r_o}{r_i}\right), \tag{6.24}$$

with $\hat{\lambda}_r = \hat{\lambda}_\theta^{-1}$ (Eq. 6.11) and where r_o is given by Eq. 6.4.

An iterative procedure between LS minimization and FE analysis (Alg. 1) is used to determined the radial position $\hat{r}$ and model parameters a_1, a_2 and a_3 The initial guess for the radial position is set to the middle wall position, $\hat{r}_k = \frac{1}{2}(r_i + r_o)$ for $k = 0$, where k is the iteration counter. Based on the radial position $\hat{r}_k$, the model parameter $\{a_1, a_3, a_3\}_k$ are determined by LS minimization with the object function given in Eq. 6.17 and the model pressure $p_{i,k}^{\text{mod}}$ (Eq. 6.24). A subsequent FE analysis is then carried out with the obtained model parameters, to find the mean stresses

$$\overline{\sigma}_k = \overline{\sigma}_{\theta\theta,k} - \overline{\sigma}_{rr,k}, \tag{6.25}$$

calculated from the FE results by Eqs. 6.7-6.6. The update in the radial position is then given by; find $\hat{r}_k$ such that

$$\sigma(\hat{r}_k) = \overline{\sigma}_k. \tag{6.26}$$

The procedure is then repeated until the position $\hat{r}_k$ converges, i.e. $|\hat{r}_{k-1} - \hat{r}_k| < \varepsilon$.

Algorithm 1: Algorithm for parameter estimation

Input: Inflation test data, p_i and λ_θ
Initialize a_1, a_2, a_3 and $\hat{r}_{k=0} = \frac{1}{2}(r_i + r_o)$
Output: a_1, a_2 and a_3
while $|\hat{r}_{k-1} - \hat{r}_k| > \varepsilon$ **do**
  (*1.*) LS optimization (Eq. 6.17)
  (*2.*) FE analysis
  foreach pressure level p_i **do**
    (*3.*) calculate $\overline{\sigma}_k = \overline{\sigma}_{\theta\theta,k} - \overline{\sigma}_{rr,k}$ (Eqs. 6.7-6.6)
    (*4.*) find $\hat{r}_k \Rightarrow \sigma(\hat{r}_k) = \overline{\sigma}_k$
  end
  $k = k + 1$;
end

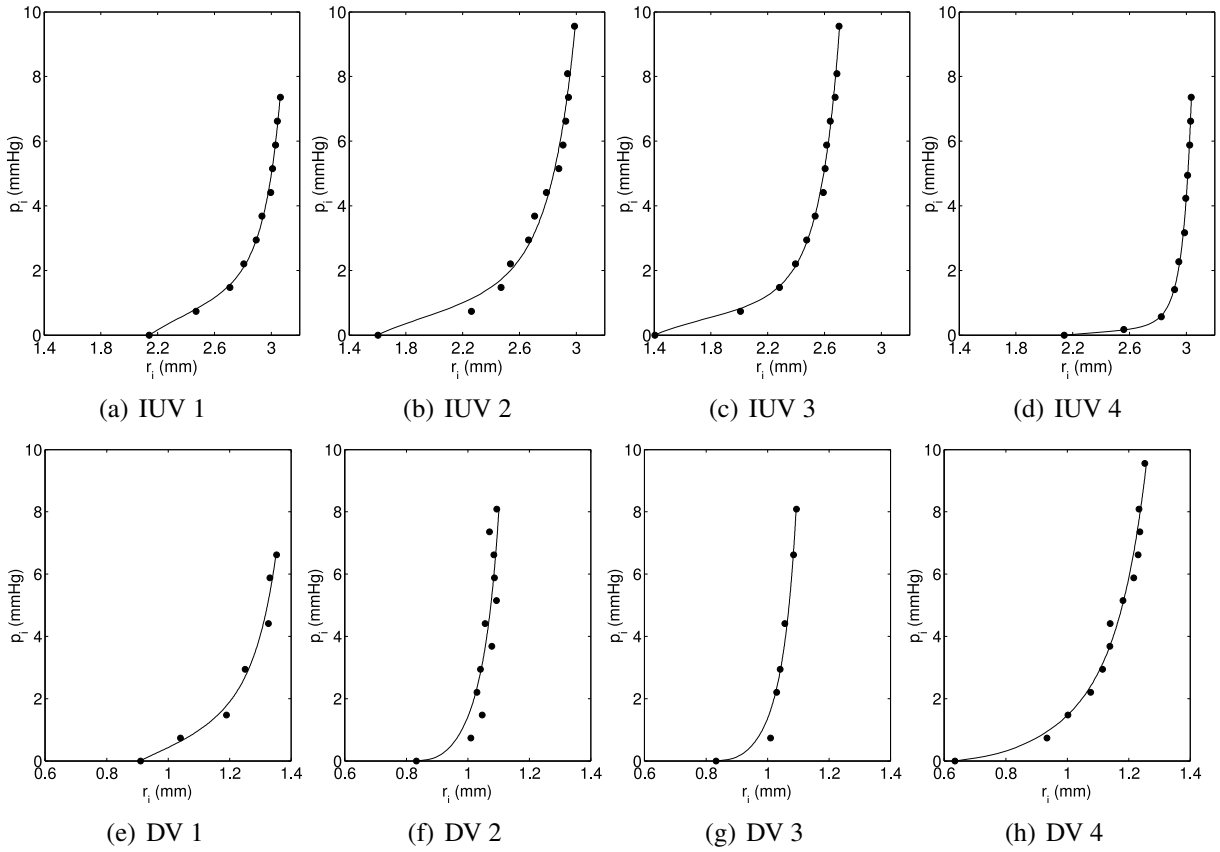

(a) IUV 1 (b) IUV 2 (c) IUV 3 (d) IUV 4

(e) DV 1 (f) DV 2 (g) DV 3 (h) DV 4

Figure 6.2 Inflation data (*dots*) and model response (*solid lines*) for the four IUV and four DV samples, given by the transmural pressure p_i versus internal radius r_i.

6.3 Results

The model parameters a_1, a_2 and a_3 are estimated for the four IUV and DV inflation test samples. The optimization procedure (Alg. 1) required on average less than four iterations to converge for a tolerance of $\varepsilon = 0.01$mm. The results are presented in Table 6.1, which includes the initial sample radius R_i, the model parameters a_1, a_2 and a_3 and the objective function residual ϵ, for the individual IUV and DV samples, and the IUV and DV sample population mean and standard deviation (std). As can be observed for the mean parameter values given in Table 6.1, the Neo-Hookean parameter a_1 is higher for the IUV than for the DV, while the exponential parameters a_2 and a_3 are higher for the DV than for the IUV. Furthermore, significant spread is present in the model parameters between samples, as reflected by the standard deviations. A lower bound of 100 Pa is enforced on the a_1 parameter for all samples during optimization, which proved necessary to avoid divergence of the FE model at low pressures for DV samples 2 and 3.

The inflation data and the model and response from FE analysis (Table 6.1) are compared in Fig. 6.2a-h, for the four IUV and DV samples. A clear stiffening behavior in the radial

expansion is observed for increasing pressure, with significant radial expansion for transmural pressures below ∼2mmHg. Moreover, a good match between the inflation data and the FE simulations can be observed both in the low and high pressure region, especially for IUV samples 1, 3 and 4, and DV samples 1 and 4.

Table 6.1 Results from the model parameters optimization for the four IUV and DV samples, given by the reference inner radius R_i; model parameters a_1,a_2 and a_3; the objective function residual ϵ.

	IUV					DV				
sample	R_i (mm)	a_1 (Pa)	a_2 (Pa)	a_3	ϵ (mmHg)	R_i (mm)	a_1 (Pa)	a_2 (Pa)	a_3	ϵ (mmHg)
1	2.14	2423.3	460.8	5.90	0.5	0.91	1092.4	716.7	2.73	1.0
2	1.60	1398.4	1524.0	0.57	1.4	0.83	100.0	911.3	9.22	4.3
3	1.41	1113.2	792.9	0.60	0.9	0.83	100.0	608.9	12.47	1.1
4	2.14	347.1	30.5	15.14	0.5	0.64	205.3	2277.4	0.29	1.6
mean	1.82	1320.5	702.1	5.55	0.8	0.80	374.4	1128.9	6.16	2.0
std	0.38	743.8	546.1	5.95	0.4	0.12	481.2	775.9	5.63	1.6

6.4 Conclusions

This study presents a first estimate of a constitutive model and parameters for the IUV and DV. Additionally, a method for parameter estimation is outlined, where model parameters are determined from experimental data with the LS technique in combination with FE simulations. The current study relies on experimental data on the compliance of fetal sheep IUV and DV from *in-vitro* inflation tests provided by Hellevik et al. [76]. Optimized model parameters for four IUV samples and four DV samples are given in Table 6.1, including mean values and standard deviation. Significant spread in the model parameters are present between samples, as reflected by the standard deviations.

The *in-vitro* compliance data from Hellevik et al. [76] for the IUV and DV samples in Fig. 6.2a-h are compared to the corresponding model response (Table. 6.1) in FE simulations. A close match is found both in the low and high pressure region for the majority of the IUV and DV samples, indicating that the proposed model with a Neo-Hookean and exponential term is adequate to describe the non-linear radial expansion, seen in the sample population. However, the relative contribution from the Neo-Hookean and exponential term differs significantly between samples for both the IUV and DV parametric sets, as seen in Table. 6.1.

An isotropic hyperelastic material model for the IUV and DU is proposed in this work. However, the collagen and elastin fiber layout in most vascular tissues are highly anisotropic [83], e.g Pennati [150] reported higher stiffness in the axial direction compared to the circumferential direction of human cordial UVs, both in the low and high strain region.

An approximation for the unloaded radius-wall thickness ratios R_i/H for the IUV and DV samples is used this study. The approximation is based on morphological data from the literature

by Ailamazyan et al. [2], on the human IVU and DV. A radius-wall thickness ratio R_i/H of 7.0 is used for the four IUV samples and 6.7 for the four DV samples. The assumption of the two general radius-wall thickness ratios for the IUV and DV samples sets, is necessary to allow for a continuum model to be fitted to the experimental data, as the individual wall thicknesses of the IUV and DV specimens from Hellevik et al. [76] are unknown. The limitation introduced by the approximation of the radius-wall thickness ratio will significantly influence the value of the model parameters, which might explain the some of the large spread in the model parameter given in Table 6.1.

In conclusion, the proposed isotropic hyperelastic model and fitted parameters, proved capable of describing the measured compliance during inflation test on fetal sheep IUV and DV from Hellevik et al. [76], when compared in FE analysis. However, significant spread is presents in the derived model parameters. Moreover, the proposed model and parameters must be viewed in the light of the limitations represented by an isotropic constitutive model, and the general radius-wall thickness ratios employed to obtain the model parameters for the IUV and DV sample population.

Chapter 7

Structural properties and constitutive modelling of the human umbilical vein and Wharton's jelly

The content of this chapter was submitted for journal publication in 2012

Structural properties and constitutive modeling of the human umbilical vein and Wharton's jelly
P.R. Leinan, V. Prot, C.N. van den Broek, T. Kiserud, C. Vogt, B. Skallerud, F.N. van de Vosse and L.R. Hellevik

7.1 Introduction

During the last 30 years, advances particularly in ultrasound techniques have brought forth the fetal circulation as an important field of clinical medicine. In this domain, the umbilical cord is the crucial connection between the placenta and the fetus [21]. The two umbilical arteries (UA) have been studied extensively, and used to assess downstream impedance in the feto-placental circulation. The umbilical vein (UV) has more recently gained interest for assessing volume flow and studying flow propagation, both important components in understanding normal and abnormal hemodynamics in the growing fetus. In particular the interpretation of pulsatile blood velocities in the UV has proven to be a challenge, signifying the need for more insight into the underlying mechanisms [102]. While it is known that UV diameter, vascular tone and response to flow variation are not under neural [53] but endocrine control [71, 138, 139], less is known of the equally important mechanical properties of the UV and its surrounding tissue, i.e. the Wharton's jelly (WJ). Hence, in the present study we focus on the mechanical properties of the UV and WJ.

The umbilical cord floats freely in the amniotic fluid except from the attachment points at the placenta and fetal navel. The different tissues that make up the umbilical cord (Fig. 7.1) are therefore responsible for the structural integrity of the umbilical vessels and an open and efficient passage for fetal blood during gestation and birth. The umbilical cord needs to be capable of withstanding a variety of external loads such as compression, bending, knotting and tension [47]. Additionally, the umbilical vessels need to handle the load from varying blood pressure and flow during fetal development. The umbilical venous blood pressure for human fetuses has been measured during cordocentesis in normal and pathological pregnancies [188, 192]. The findings suggest a range of 1-11 mmHg, with a mean value of 6 mmHg at term.

The UV and two arteries are coiled around each other in helical spirals, and the degree of coiling can be identified by the umbilical coiling index (number of coils divided by cord length). The normal umbilical cord length is reported to be 50-60cm at term of gestation, with 10-11 helical coils between the placenta and fetus, i.e. a coiling index in the range of 17-22 [21, 145]. The umbilical vessels are embedded in Wharton's jelly (WJ), which is described as an elastic collagen-based extracellular matrix with interconnected fluid-filled pores [47]. WJ does not contain elastin fibers, but a glycoprotein microfibrils network is present in the collagen matrix which can contribute to the elastic behavior of the WJ at low loads [135, 150]. The amount of WJ and degree of coiling (i.e. lean and hyper-coiled cord respectively) and other umbilical cord abnormalities have been investigated as risk factors in several studies [46, 145, 172]. The WJ is encased by an outer amniotic epithelium layer, and it is assumed that this membrane maintains the fluid pressure within the WJ cannular structure, giving added resistance to compression of the umbilical vessels [21]. The UV lacks the typical adventitia found in other cardiovascular vessels, and it is suggested that the surrounding WJ assists the structural integrity of the UV [47, 150]. The UV and WJ are attached to each other by bundles of collagen fibers [189], and studies by Bańkowski et al. [8] and Nanaev et al. [144] suggest that the collagen orientation in the WJ becomes more circular close to the UV. The UV tissue contains collagen and elastin fibers, smooth muscle cells and ground substance, and Li et al. [123] and Benirschke and Kaufmann [20] reported axially and circularly arranged smooth muscle cells in the inner and outer (media)

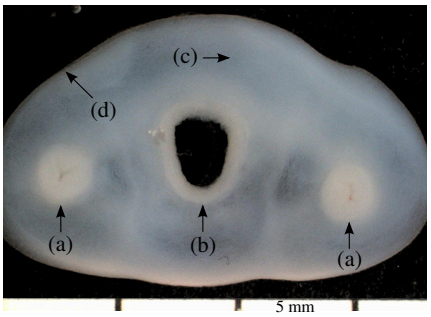

Figure 7.1 Cross section of a human umbilical cord, (a) umbilical arteries, (b) umbilical vein, (c) Wharton's jelly (blue colored tissue surrounding the umbilical arteries and vein) and (d) amniotic epithelium (outer skin layer)

layer of the UV, respectively. The study by Li et al. [123] also concludes that the percentage content of elastin, collagen and smooth muscle cells is similar to other cardiovascular vessels. A cross section of a human umbilical cord (from the current study) can be seen in Fig. 7.1, containing two arteries, the UV, WJ and the amniotic epithelium. More detailed descriptions on the micro structure and composition of the different tissues in the umbilical cord can be found in e.g. Bańkowski et al. [8], Franc et al. [54], Li et al. [123], Nanaev et al. [144], Vizza et al. [189] and Bańkowski [7].

The anatomical and histological aspects of the umbilical vessels and WJ have been given much attention in the literature. While many studies address other cardiovascular tissues from a mechanical point of view, e.g. adult human arteries, relatively few addresses the umbilical tissue from this perspective. Studies in the literature where the mechanical properties of the umbilical cord are investigated include Bertrand et al. [22], Daniel et al. [36], Gervaso et al. [61], Ghosh et al. [62], Goktas et al. [65], Hellevik et al. [76], Li et al. [122], Pennati [150] and Li et al. [121]. These studies include investigations on human and animal material, e.g. Hellevik et al. [76] tested the intra abdominal UV of fetal lambs. Others have tested the mechanical properties of human UVs for loads beyond physiological conditions aimed at using the UV as a graft for tissue engineering [36, 121, 122]. The most extensive mechanical investigation of the human umbilical cord is carried out by Pennati [150]. In his paper, uni-axial tension (circumferential and axial) and compliance tests provided mechanical properties of the UV and WJ, including viscoelastic effects.

The motivation for the work presented here, originates from the observation that constitutive modeling of vessels in the umbilical cord is missing in the literature, and that material parameters for human umbilical tissues are relatively scarce [47]. This work therefore focuses on deriving a structural model for the human UV and surrounding WJ, using the continuum framework frequently employed to model arteries and veins [83, 163]. Additionally, *in vitro* inflation-extension (IE) tests on nine healthy umbilical cord specimens are carried out, allowing the structural model and the associated material parameters to be fitted to experimental data.

7.2 Materials and methods

7.2.1 Experimental setup

An *in vitro* IE setup for mechanical testing of cardiovascular vessels under approximated physiological conditions was used in this work [184].

The UV specimens were connected to two separate hollow stainless steel rods by Luer-lock polycarbonate fittings. The samples and steel rods assembly were immersed in an organ bath. The steel rods was extended out from the organ bath, and rubber gaskets ensured a tight seal. Silicone tubing was attached to the steel rods and the organ bath, and connected to a pressure pump driven by a proportional pneumatic valve (Festo, The Netherlands). Connector valves controlled the flow distribution through the specimens and/or organ bath. A part of the silicone tubing was immersed in a heater bath with a temperature control system keeping the fluid at 38^oC. A pressure transducer was placed in-line with the specimens to measure the lumen pressure p_i. One of the steel rods was connected to a load cell measuring the reduced axial force F_z (Eq. 7.14). The second steel rod was attached to a linear actuator controlling the axial displacement, giving the axial stretch λ_z. The inner diameter of the specimens d_i was recorded by a linear array ultrasound scanner (8 MHz, Esaote Europe, The Netherlands) combined with arterial analyzer software (Art.Lab, Esaote Europe, The Netherlands). The diameter was measured along 32 lines/cm (in the axial z-direction, see Fig. 7.2) in B-Mode (30 frames/s). A static fluid column was connected to the test assembly with silicone tubing, which made it possible to control the pressure p_i in increments by adjusting the fluid column height. Hence, the pressure pump was used to circulate the fluid through the test samples and organ bath to equilibrate the tissue. During mechanical testing, the flow was directed to the organ bath only to keep the temperature constant, and the static fluid column was used to control the lumen pressure p_i.

7.2.2 Experimental protocol

The *in vitro* IE tests were carried out at Laboratory for Biomechanics, TU/e Eindhoven the Netherlands. The umbilical cord specimens were collected from nine normal pregnancies at term at the Maxima Medical Center, Eindhoven the Netherlands, and included 6 female and 3 male vaginally delivered newborns at gestational age 39.6 ± 1.0 weeks. All contributors were informed about the nature of the study and gave their written consent. The average birth weight was 3277.8 ± 466.8 grams, placenta weight 537.28 ± 152.5 grams, and Apgar score was recorded to 9.1 ± 0.4 and 10 ± 0.0 (Apgar score at 1 and 5 minutes respectively).

The umbilical cords were harvested shortly after birth, stored in bottles containing phosphate buffered saline (PBS) and placed in a refrigerator (4^oC). The umbilical cord specimens where transported from the hospital to the laboratory in an insulated bag, where sample preparation started immediately, directly followed by mechanical testing. Maximum 24 hours (mean 17.5h$\pm$6.2h) elapsed from time of birth and harvest of the umbilical cords to mechanical testing.

A section from each umbilical cord was selected for testing. A relatively uniform and straight test specimen was necessary in the IE test set-up (see Sec. 7.2.1). It was therefore

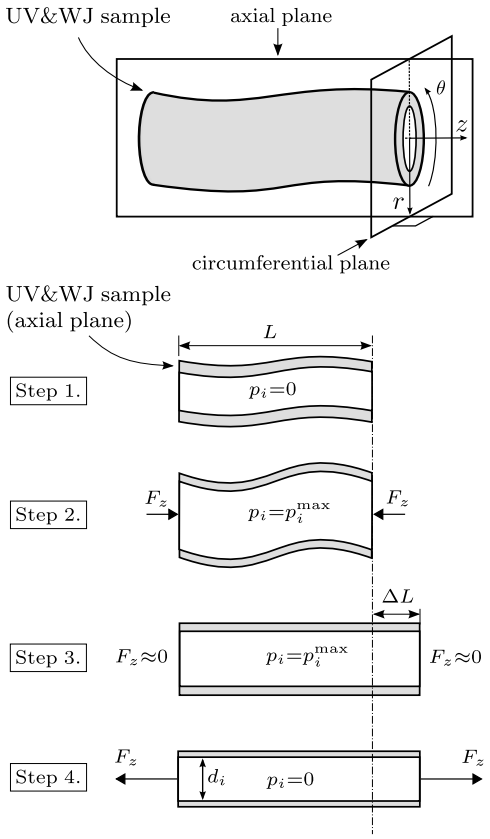

Figure 7.2 *Inflation-extension testing procedure*. Schematic overview of a UV&WJ specimen during *in vitro* IE testing. Given by the lumen pressure p_i; reduced axial force F_z; internal diameter d_i; reference length L; and the change in length ΔL under displacement control. The IE test procedure is illustrated in four steps. Step 1, the sample in the unloaded state at reference length. Step 2, the sample is pressurized to maximum assumed physiological pressure $p_i = p_i^{\max} \approx 11$ mmHg, while the reference length is maintained. Step 3, the sample is stretched by a length ΔL until the specimen is straightened and the reduced axial force is positive and close to zero. Step 4, the lumen pressure is stepwise reduced to zero, while the change in reduced axial force F_z and internal diameter d_i are recorded

important to select a cord section that met these requirements. However, a sample in the middle region of the cord was chosen if possible. The amniotic epithelium and sub-amniotic layer (Fig. 7.1) was carefully removed from the umbilical cord samples using a scalpel, forceps and micro-dissection scissor. The procedure revealed the umbilical arteries and the UV with a layer of surrounding WJ (see Fig. 7.4). It proved difficult to remove the WJ layer surrounding the UV samples. The transition between the UV and WJ was also not obvious during sample preparation, and it was decided to treat the surrounding WJ layer as a part of the UV structure and not to remove it. The UVs with an outer layer of WJ was therefore accepted as the test specimens (The test samples of the UVs with an outer layer of WJ will in the following be refereed to as UV&WJ). Luer-lock polycarbonate fittings were inserted at each end of the UV&WJ specimens

and fixed with suture wire. The UV&WJ specimens were placed in a PBS bath and the length between the sutures at each end was measured with a caliper rule giving the reference length L ($L_{\text{mean}} = 35.5 \pm 4.1$mm). The UV&WJ specimens were then fixed in the organ bath of the *in vitro* test setup (Sec. 7.2.1), and PBS solution at 38^oC was circulated through the samples and organ bath for 30 minutes to equilibrate. Subsequently, Papaverine (10^{-4}M) was added to the PBS solution as a smooth muscle relaxant followed by an additional 15 minutes of circulatory flow.

Mechanical testing started with the specimens at zero external load and axial displacement (Fig. 7.2, Step 1). The specimens were preconditioned by first varying the pressure five times between $p_i = 0$ and $p_i = p_i^{\max} \approx 11$mmHg, terminating at $p_i = p_i^{\max}$ (Fig. 7.2, Step 2). The lumen pressure range is chosen based on preliminary tests, and on the findings of Ville et al. [188] and Weiner et al. [192], which suggest a physiological lumen pressure range of 1-11 mmHg for human fetuses. The reduced axial force (F_z) at this point was in the majority of cases slightly negative, and some of the UV&WJ specimens became slightly tortuous. Subsequently, the axial stretch was increased (displaced by ΔL) so that the samples straightened and the reduced axial force magnitude was positive and close to zero (Fig. 7.2, Step 3). The axial displacement ΔL was preconditioned five times. Finally, the lumen UV&WJ pressure p_i was stepwise decreased (≈ 1mmHg) from $p_i^{\max}$ to $p_i = 0$. Each stepwise pressure reduction was followed by a 4 minute static interval to allow viscoelastic effects to dissipate [150]. The UV&WJ lumen pressure p_i, diameter d_i and reduced axial force F_z were recorded at the end of each 4 minute interval, in accordance with the procedure explained in Sec. 7.2.1. The decrease in pressure to $p_i = 0$, resulted in increasing reduced axial force magnitude F_z (Fig. 7.2, Step 4). Subsequently, cross sectional slices (rings) were cut from the UV&WJ specimens with a scalpel and photographed with a microscope. The images was used to calculate the unloaded dimensions of the specimens, and fraction of WJ to UV area, by image analysis and visual inspection.

7.2.3 Histology

A histological study was carried out to investigate the fiber orientation in the WJ layer around the UV. Three WJ specimens were collected from three umbilical cords at the Department of Pathology and Medical Genetics at the University Hospital of Trondheim, Norway. The specimens where sliced repeatedly in the circumferential direction (i.e in the θ-direction, Fig. 7.2) with a microtome, from the outer WJ surface (the amniotic epithelium layer, Fig. 7.1) to the transition zone between the WJ and the UV. The sample slice thickness was 5μm, and the distance between each collected sample slice was in the order of 100μm. A total of 43 WJ slices where collected from the three WJ specimens. The WJ slices were stained with and Collagen-Masson's trichrome (TRI) and photographed under a microscope (10X magnification). The fiber distribution and directions in the stained WJ slice images was quantified with an image analysis software (OrientationJ, [162, 166]).

7.2.4 Vessel compliance and pulse wave velocity

The compliance of an elastic vessel is given by

$$C = \frac{\partial A}{\partial p}, \tag{7.1}$$

where $A = \pi d_i^2/4$ is the vessel cross sectional area and $p = p_i$ is the lumen pressure. The vessel pulse wave velocity c can be estimated from the vessel compliance

$$c = \sqrt{\frac{A}{\rho C}}, \tag{7.2}$$

known as the Bramwell-Hill equation [29], where ρ is the fluid density.

A model for the expansion fetal of veins as a function of lumen pressure has been proposed by Hellevik et al. [76], where the pressure-area ($p - A$) relation is described by an exponential function

$$p = p_s \exp\left[b\,(\frac{A}{A_s} - 1)\right], \tag{7.3}$$

given by a standard pressure $p_s = 5$ mmHg, A_s the lumen area at standard pressure and a stiffness parameter b. The exponential pressure-area model provides the opportunity to describe a non-linear vessel area expansion as a function of lumen pressure by a single stiffness parameter, b, which is convenient for comparison with studies on fetal veins in the literature, e.g. Hellevik et al. [76], Pennati [150].

7.2.5 Kinematics

The deformation of a cylindrical tube due to an internal pressure and axial stretch is conveniently expressed in cylindrical coordinates. Let Ω_0 be the free reference configuration where a material point is given by $\{R, \Theta, Z\}$. A material point in the deformed configuration Ω is given by $\{r, \theta, z\} = \{r(R), \Theta, \lambda_z Z\}$. The angular coordinate is equal in the deformed and the reference configuration meaning that the deformation is axisymmetrical with respect to the z-axis. A schematic representation of the deformation is seen in Fig. 7.3, the tube is defined by the radial and axial coordinates

$$\begin{aligned} R_i \leq R \leq R_o, \quad 0 \leq Z \leq L \quad \text{in} \quad \Omega_0 \\ r_i \leq\ r \leq r_o, \quad 0 \leq z \leq l \quad \text{in} \quad \Omega \end{aligned} \tag{7.4}$$

subscripts i and o denote the inner and outer radius respectively. The deformation in the axial direction is defined by the stretch λ_z, which is a known value. The function $r(R)$ is then the only unknown, and links the deformed radial coordinate r to the reference configuration. A material point $\mathbf{x} = \chi(\mathbf{X})$ in the deformed configuration can now be written in the form

$$\mathbf{x} = r(R)\ \mathbf{e}_r + \lambda_z Z \mathbf{e}_z, \tag{7.5}$$

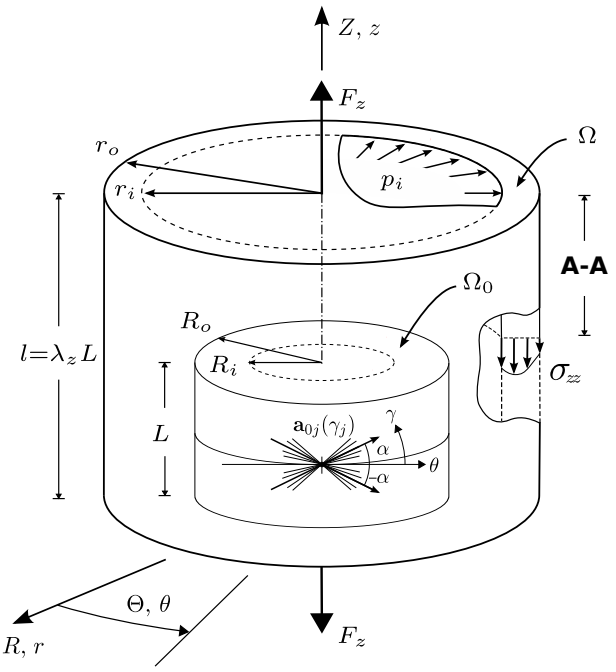

Figure 7.3 Overview of the fiber reinforced closed cylinder model of the UV&WJ specimens. The reference and current configuration are illustrated by Ω_0 and Ω respectively. The fiber distribution is illustrated in the reference configuration containing N fiber families given by $\mathbf{a}_{0j}(\gamma_j)$, $j = \{1, .., N\}$, where γ is the fiber angle. The fiber distribution is symmetric with respect to the axial (z-axis) and circumferential (θ-axis) direction, with main fiber angle α, and the distribution of fibers is determined by a normal probability distribution, Eq. 7.25, which includes a distribution angle β. The current configuration is loaded with internal pressure p_i and the reduced axial force F_z

given by the unit base vectors $\{\mathbf{e}_r, \mathbf{e}_\theta, \mathbf{e}_z\}$ in the deformed configuration with the counterparts $\{\mathbf{E}_R, \mathbf{E}_\Theta, \mathbf{E}_Z\}$ in the reference configuration given by the material point $\mathbf{X}$. The deformation gradient $\mathbf{F}$ is defined as $\mathbf{F} = \frac{\partial \chi(\mathbf{X})}{\partial \mathbf{X}}$ and maps a material point from the reference to the deformed configuration. Using Eq. 7.5 gives

$$\mathbf{F} = \frac{\partial r(R)}{\partial R}\mathbf{e}_r \otimes \mathbf{E}_R + \frac{r(R)}{R}\,\mathbf{e}_\theta \otimes \mathbf{E}_\Theta + \lambda_z\,\mathbf{e}_z \otimes \mathbf{E}_Z. \tag{7.6}$$

The deformation is considered isochoric giving $\det(\mathbf{F}) = 1$ and integration with respect to the reference radius R yields an expression for the deformed radius

$$r = r(R) = \sqrt{\frac{R^2 - R_i^2}{\lambda_z} + r_i}, \tag{7.7}$$

in which r_i and R_i are the internal current and reference tube radii. The stretches in the radial λ_r and circumferential direction λ_θ are identified as

$$\lambda_r = \frac{R}{r\lambda_z}, \quad \lambda_\theta = \frac{r}{R}, \tag{7.8}$$

from substitution of Eq. 7.7 into Eq. 7.6. The deformation gradient can now be expressed in terms of the stretches

$$\mathbf{F} = \lambda_r \mathbf{e}_r \otimes \mathbf{E}_R + \lambda_\theta \, \mathbf{e}_\theta \otimes \mathbf{E}_\Theta + \lambda_z \, \mathbf{e}_z \otimes \mathbf{E}_Z, \tag{7.9}$$

where incompressibility requires $\det(\mathbf{F}) = \lambda_r \lambda_\theta \lambda_z = 1$ [83].

7.2.6 Equilibrium

The local Cauchy equations of motion for a body, when body forces and accelerations are excluded, reduces to

$$\nabla \cdot \boldsymbol{\sigma} = \mathbf{0}, \tag{7.10}$$

which in component form in cylindrical coordinates for the radial and axial directions when shear stresses are not present further reduces to

$$\frac{d\sigma_{rr}}{dr} + \frac{(\sigma_{rr} - \sigma_{\theta\theta})}{r} = 0, \tag{7.11}$$

$$\frac{d\sigma_{zz}}{dz} = 0. \tag{7.12}$$

Integration of Eq. 7.11 gives the stress balance over a cross section normal to the z axis (Fig. 7.3). Hence, the boundary conditions $p_i = -\sigma_{rr}|_{r=r_i}$ and $\sigma_{rr}|_{r=r_o} = 0$ yields the pressure

$$p_i = \int_{r_i}^{r_o} \frac{(\sigma_{\theta\theta} - \sigma_{rr})}{r} \, dr, \quad r_i \leq r \leq r_o, \tag{7.13}$$

on the inner cylinder surface [34]. A force balance in the axial direction of the cylinder is also needed. From Eq. 7.12 we realize that there is no axial dependence of σ_{zz}, and thus the axial force may be derived from a force balance at a given cross section. Considering the cross sectional cut **A-A** in Fig. 7.3, gives the reduced axial force

$$F_z = 2\pi \int_{r_i}^{r_o} \sigma_{zz} r dr - p_i \pi r_i^2, \tag{7.14}$$

which is the force measured during IE tests [83], required to hold the vessel at the constant length $l = \lambda_z L$.

7.2.7 Material description

Constitutive modeling

The mechanical (passive) response of arterial and vein tissue is mainly governed by the presence of connective tissue, collagen and elastin fibers [56, 89]. Cardiovascular tissue is also considered to be nearly incompressible, it is therefore convenient to split the material response

into a dilatation and distortional part. Hence, in the following the multiplicative decomposition of the deformation gradient

$$\mathbf{F} = (J^{1/3}\mathbf{I})\,\bar{\mathbf{F}}, \tag{7.15}$$

is considered, defined by the volume ratio $J = \det \mathbf{F} > 0$ [48].

An invariant-based partial structural model is chosen to model the passive mechanical behavior of the UV&WJ samples [119], based on contributions by Holzapfel et al. [83] and Rezakhaniha and Stergiopulos [163]. The components of the structural model is based on the histological description of the UV and WJ in the literature. The UV is reported to contain both elastin and collagen fibers, and the WJ is reported to be rich in collagen fibers and contains an elastic glycoprotein microfibrils network (see Sec. 7.1).

Elastin description

Elastin in the UV and the elastic glycoprotein microfibrils network in the WJ are lumped into one elastic material and modeled as an isotropic Neo-Hookean material (Eq. 7.23).

Collagen fiber description and distribution

Collagen fibers in the UV and WJ are modeled as elastic fibers, where the elasticity is given by exponential functions of the fiber stretch (Eq. 7.24). The detailed orientation of collagen fibers in the UV and surrounding WJ is unknown, however findings in the literature indicate that the fiber orientation in the UV is similar to other venous tissue [123], and that the fiber orientation in the WJ is more uniform than in the UV but mainly circumferential close to the UV [8, 144]. In this work we choose to lump the fiber content of the UV and the surrounding WJ into a normal probability distribution (Eq. 7.25) [43]. The fiber distribution is represented by N fiber families with main fiber angle α, and a dispersion angle β. A fiber dispersion angle of $\beta = 10\,\text{deg}$ is assumed in this work, to limit the number of unknown material parameters.

Strain energy potential

The isotropic and anisotropic structural components of the UV and the surrounding WJ are lumped into one UV&WJ material model, given by a strain energy potential Ψ. The strain energy potential contains a volumetric (dilatational) part $U(J)$ to enforce incompressibility, an isotropic part $\bar{\Psi}_{\text{iso}}$ with a Neo-Hookean response and an anisotropic part $\bar{\Psi}_{\text{aniso}}$ with N fiber families.

$$\Psi = U(J) + \bar{\Psi}^{\,\text{iso}}(\bar{\mathbf{C}}) + \bar{\Psi}^{\,\text{aniso}}(\bar{\mathbf{C}}, \mathbf{a}_{0j} \otimes \mathbf{a}_{0j}), \quad j = 1, .., N \tag{7.16}$$

where $\bar{\mathbf{C}} = \bar{\mathbf{F}}^T\bar{\mathbf{F}}$ is the modified right Cauchy-Green deformation tensor, and $\mathbf{a}_{0j}$ are vectors representing N fibers in the reference configuration

$$\mathbf{a}_{0j} = \cos(\gamma_j)\,\mathbf{E}_\theta + \sin(\gamma_j)\,\mathbf{E}_z, \quad j = 1, .., N \tag{7.17}$$

given by the unit reference cylindrical basis vectors $\mathbf{E}_\theta$ and $\mathbf{E}_z$. The fiber directions γ_j are given as angles relative to the circumferential direction. The strain energy potential is redefined with

regards to invariants, giving

$$\Psi = U(J) + \bar{\Psi}^{\,\mathrm{iso}}(\bar{I}_1) + \bar{\Psi}^{\,\mathrm{aniso}}(\bar{I}_{4j}), \quad j = 1, .., N \tag{7.18}$$

defined by,

$$\bar{I}_1 = \mathrm{tr}\,(\bar{\mathbf{B}}), \tag{7.19}$$

$$\bar{I}_{4j} = \mathrm{tr}\,(\bar{\mathbf{a}}_j \otimes \bar{\mathbf{a}}_j), \quad j = 1, .., N \tag{7.20}$$

$\bar{I}_1$ is the first invariant of the modified left Cauchy-Green deformation tensor $\bar{\mathbf{B}} = \bar{\mathbf{F}}\,\bar{\mathbf{F}}^T$, and $\bar{\mathbf{a}}_j = \bar{\mathbf{F}}\,\mathbf{a}_{0j}$ are the stretched fibers in the deformed configuration associated with volume preserving deformation. The invariants $\bar{I}_{4j}$ are the squared stretches in the direction of the fibers

$$\bar{I}_{4j} = \bar{\lambda}_\theta^2 \cos^2(\gamma_j) + \bar{\lambda}_z^2 \sin^2(\gamma_j), \quad j = 1, .., N \tag{7.21}$$

$$\text{where} \quad \bar{\lambda}_\theta = J^{-1/3}\lambda_\theta, \quad \bar{\lambda}_z = J^{-1/3}\lambda_z.$$

The functions describing the volumetric, isotropic and anisotropic terms in the UV&WJ strain energy potential Ψ are given by

$$U(J) = \frac{\kappa}{2}(J-1)^2, \tag{7.22}$$

$$\bar{\Psi}^{\,\mathrm{iso}}(\bar{I}_1) = c_1(\bar{I}_1 - 3), \tag{7.23}$$

$$\bar{\Psi}^{\,\mathrm{aniso}}(\bar{I}_{4j}) = \sum_{j=1}^{N} \phi_j \frac{k_1}{2k_2}(\exp[k_2\,(\bar{I}_{4j} - 1)^{\,2}] - 1), \tag{7.24}$$

where the fiber distribution ϕ_j is determined by a normal probability distribution

$$\phi_j = A\,\exp\left[\frac{\cos[2(\gamma_j - \alpha)] + 1}{\beta}\right], \quad j = 1, .., N \tag{7.25}$$

which includes the main fiber angle α; the dispersion angle β; and a scaling factor A defined such that the total fiber content equals $\sum_{j=1}^{N} \phi_j = 1.0$ [43]. The fiber distribution is symmetric with respect to the axial (z-axis) and circumferential (θ-axis) direction as illustrated in Fig. 7.2, and discretized with $N = 180$ fiber angles i.e. $\gamma_j = \{$-89, -88, .., 89, 90$\}$. The parameters k_1 and k_2 (Eq. 7.24) are material parameters for the exponential fiber response. Furthermore, c_1 is the Neo-Hookean material parameter (Eq. 7.23). The material is modeled slightly compressible, where κ is a positive penalty parameter in the penalty function $U(J)$ (Eq. 7.22). The aim is to choose an appropriate value for κ so that the material behavior is nearly incompressible, for discussion see Prot and Skallerud [156].

Cauchy stresses

The Cauchy stresses are given by

$$\boldsymbol{\sigma} = \frac{2}{J}\,\mathbf{F}\frac{\partial \Psi}{\partial \mathbf{C}}\mathbf{F}^T \tag{7.26}$$

in which the strain energy potential is differentiated with respect to the right Cauchy-Green tensor $\mathbf{C}$ followed by a push forward by the deformation gradient $\mathbf{F}$. Furthermore, the stresses are split into an hydrostatic and a deviatoric part

$$\boldsymbol{\sigma} = \kappa(J-1)\,\mathbf{I} + \frac{1}{J}\mathrm{dev}(\bar{\boldsymbol{\sigma}}). \tag{7.27}$$

Hence, for the UV&WJ material model the deviatoric stress tensor $\bar{\boldsymbol{\sigma}}$ is given by

$$\bar{\boldsymbol{\sigma}} = 2\;\bar{\Psi}_1^{\,\mathrm{iso}}\,\bar{\mathbf{B}}\;\; + \sum_{j=1}^{N} 2\;\bar{\Psi}_{4j}^{\,\mathrm{aniso}}\,\bar{\mathbf{a}}_j \otimes \bar{\mathbf{a}}_j \tag{7.28}$$

where the notation $\frac{\partial \bar{\Psi}}{\partial \bar{I}_{4j}} = \bar{\Psi}_{4j}$ is used [156].

7.2.8 Model parameter optimization

The IE tests (Sec. 7.2.2) provides radii $r_i^{\exp}$ and reduced axial force $F_z^{\exp}$ data points as a function of lumen pressure p_i for the nine UV&WJ specimens in the sample population. The numerical model of the UV&WJ given in Sec. 7.2.7 is evaluated with respect to the experimental data by a normalized error, ε, given by

$$\begin{aligned}\varepsilon^2 &= \varepsilon_r^2 + \varepsilon_{\Delta F}^2 \\ &= \frac{\sum (r_i^{\exp} - r_i^{\mathrm{mod}})^{\,2}}{\sum (r_i^{\exp})^{\,2}} + \frac{\sum (\Delta F_z^{\exp} - \Delta F_z^{\mathrm{mod}})^{\,2}}{\sum (\Delta F_z^{\exp})^{\,2}},\end{aligned} \tag{7.29}$$

where the superscript 'mod' and 'exp' are short for model and experimental values respectively, and ε_r and $\varepsilon_{\Delta F}$ are the normalized error for the radial expansion and change in reduced axial force. In this study, the change in reduced axial force is considered in the parameter optimization, obtained from subtracting the mean reduced axial force contribution, $\Delta F_z = F_z - \overline{F}_z$, due to a possible inaccuracy in the absolute axial force measurements [184]. Furthermore, the relative contributions from radial expansion and the change in reduced axial force in the normalized error are weighted by a scalar ω giving the objective function

$$\hat{\varepsilon}^2 = \omega\,\varepsilon_r^2 + (1-\omega)\,\varepsilon_{\Delta F}^2. \tag{7.30}$$

The weighting factor is introduced to balance the contribution for the radial expansion and change in reduced axial force. The weighting factor is determined prior to parameter optimization for each IE data set from the relation

$$\omega = \frac{\varepsilon_{\Delta F}^2}{\varepsilon_r^2 + \varepsilon_{\Delta F}^2}, \tag{7.31}$$

by comparing 4th order polynomials fits of the radial expansion and change in the reduced axial force of the experimental data to the original experimental data.

The continuum model representing the UV&WJ (Sec. 7.2.7) is implemented in the finite element (FE) software *Abaqus* FEA by a user subroutine, for implementation details see Prot and Skallerud [156]. The UV&WJ is modeled as a cylinder consisting of axisymmetrical quadratic elements (CAX8RH). A grid containing 10 elements with a bias ratio of 15 toward the inner cylinder surface, proved to provide sufficient grid resolution in the desired load range. The cylinder is free to expand in the radial direction, and can be displaced axially by a length $\Delta L = L(\lambda_z - 1)$. A uniformly distributed pressure p_i is applied on the internal cylinder surface. Hence, the FE model provides the position of the internal cylinder surface r_i^{mod} and the change in the reduced axial force ΔF_z^{mod} through Eq. 7.14, needed in the evaluation of normalized error.

Algorithm 2: Model parameter optimization

Input:

$\Upsilon^{\text{exp}} = \{A_0, \lambda_z^{\max}, p_i^{\max}, r_i^{\text{exp}}, \Delta F_z^{\text{exp}}, \omega\}$

$\Pi_0^{\text{Geo}} = \{c_1, R_i, R_o\}$

$\Pi_0^{\text{Mod}} = \{c_1, k_1, k_2, \alpha\}$

$\varepsilon_0 = 10^{-3}, \quad \varepsilon_1 = 0$

$n = 0$

while $|\varepsilon_n - \varepsilon_{n+1}| \geq \varepsilon_0$ **do**

$$\underset{\Pi_n^{\text{Geo}}}{\text{argmin}} \ \hat{\varepsilon}^2 \quad \begin{cases} \lambda_z = \lambda_z^{\max} \\ p_i = [0, .., p_i^{\max}] \\ \pi(R_o^2 - R_i^2) = A_0 \end{cases} \tag{7.32}$$

$$\underset{\Pi_n^{\text{Mod}}}{\text{argmin}} \ \hat{\varepsilon}^2 \quad \begin{cases} \lambda_z = \lambda_z^{\max} \\ p_i = [0, .., p_i^{\max}] \\ \alpha \geq 0.0 \end{cases} \tag{7.33}$$

$n = n + 1$

end

The parameter optimization algorithm (Alg. 2) is implemented in a numerical Python environment, using sequential least squares through the *fmin_slsqp* function [93] to minimize the objective function $\hat{\varepsilon}^2$ (Eq. 7.30). The experimentally obtained data for each UV&WJ specimen $\Upsilon^{\text{exp}} = \{A_0, \lambda_z^{\max}, p_i^{\max}, r_i^{\text{exp}}, \Delta F_z^{\text{exp}}, \omega\}$ are given as input to the numerical model, i.e. the cross section area A_0 in the unloaded state; the maximum experimental axial stretch $\lambda_z^{\max}$; and the maximum experimental lumen pressure $p_i^{\max}$. Furthermore, experimentally obtained results are used in the evaluation of the normalized error (Eq. 7.29) and objective function (Eq. 7.30); the inner UV radius r_i^{exp}; the change in the reduced axial force ΔF_z^{exp}; and the weighting factor ω (Eq. 7.31).

The optimization procedure is initiated by initial guesses of the unloaded geometry Π_0^{Geo} and model parameters Π_0^{Mod} (Input, Alg. 2). Each loop in the optimization procedure contains

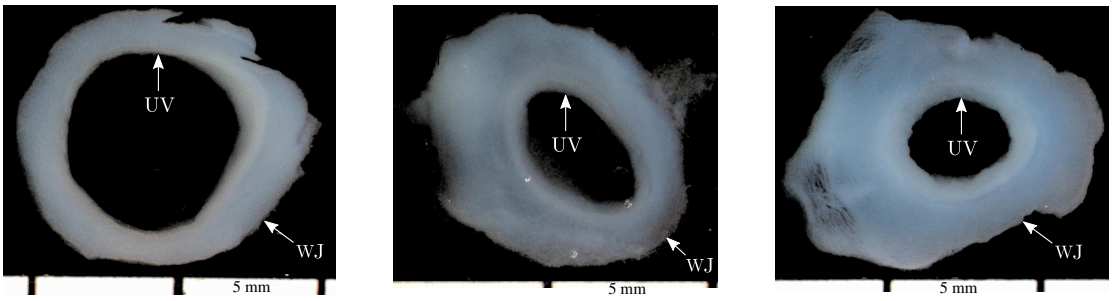

(a) UV&WJ 3 (b) UV&WJ 4 (c) UV&WJ 8

Figure 7.4 Cross sectional slices of three UV&WJ samples, showing the transition between the UV (white inner layer) and the WJ (blue outer layer)

two steps, *first step*: estimation of the reference geometry $\Pi_n^{\text{Geo}} = \{c_1, R_i, R_o\}$ (Eq. 7.32), *second step*: estimation of model parameters $\Pi_n^{\text{Mod}} = \{c_1, k_1, k_2, \alpha\}$ (Eq. 7.33) [184]. The optimization algorithm is implemented so that each gradient evaluation in the evaluation of the objective function $\hat{\varepsilon}^2$ (Eq. 7.30), calls a FE analysis of the numerical model of the UV&WJ samples. Hence, the parameters Π_n^{Geo} and Π_n^{Mod} are determined from the least square fit between the numerical model response and the experimental data through evaluation of the objective function $\hat{\varepsilon}^2$. The updated model error ε_{n+1} is computed after successful optimization of the model parameters Π_n^{Mod}, and the change in error from the previous and current iteration step $|\varepsilon_n - \varepsilon_{n+1}|$ is used as a relative convergence criterion.

7.3 Results

7.3.1 Inflation-extension tests and model parameters

The parameter optimization procedure (Sec. 7.2.8) is employed for the nine UV&WJ IE data sets. Cross sectional slices for some of the tested UV&WJ specimens can be seen in Fig. 7.4. The UV&WJ specimens contain a varying degree of WJ, and the distribution of WJ is not uniform. Model parameter results are seen in Table 7.1, and considerable variance is present, reflected by the standard deviation (SD). The fraction of WJ to UV area is given as $\text{A}_{\text{WJ/UV}}$ and the total cross sectional reference area is given by A_0.

The experimentally obtained data (dots) and numerical model response (solid line) for the nine UV&WJ data sets are shown in Fig. 7.5, giving the lumen pressure versus internal radius ($p_i - r_i$) and lumen pressure versus the change in the reduced axial force ($p_i - \Delta F_z$). A clear stiffening effect in the radial expansion r_i is observed as the pressure increases. The change in reduced axial force ΔF_z decreases with a linear trend from a maximum value at zero lumen pressure ($p_i \approx 0$). In general, the behavior of the radial expansion and the reduced axial force given by the numerical model compares reasonably well with the experimental data for the nine UV&WJ specimens. However, there is a skewed difference in the fitted axial force and the measured axial force.

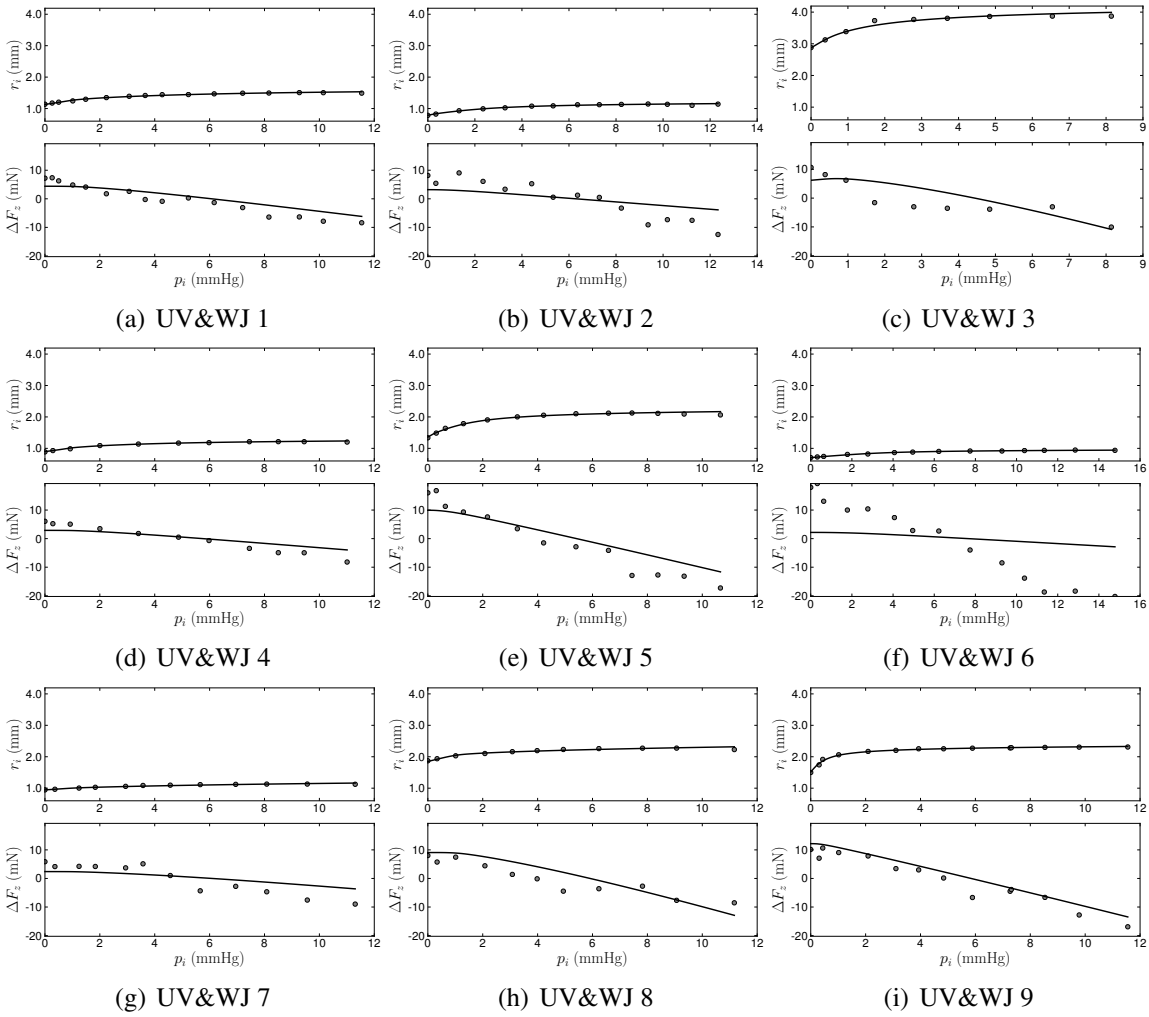

(a) UV&WJ 1 (b) UV&WJ 2 (c) UV&WJ 3

(d) UV&WJ 4 (e) UV&WJ 5 (f) UV&WJ 6

(g) UV&WJ 7 (h) UV&WJ 8 (i) UV&WJ 9

Figure 7.5 Experimental data (*dots*) and model response (*solid lines*) for the nine UV&WJ samples. Upper panel in each figure illustrates pressure versus internal radius ($p_i - r_i$). Lower panel in each figure illustrates pressure versus the change in the reduced axial force ($p_i - \Delta F_z$)

7.3.2 Collagen orientation and distribution

The normalized distribution of fibers angles ϕ_{hist} in the WJ from the histology study (Sec. 7.2.3), is seen in Fig. 7.6. The fiber distribution contains fiber directions from 43 stained WJ slices, given by the distribution mean and standard deviation at each angle. The fiber distribution indicates that the majority of the fibers angles in the WJ are aligned around the circumferential direction of the UV, i.e. $\alpha \sim 0\,\text{deg}$.

Table 7.1 Parameters for the nine UW&WJ specimens. Including, the fraction of WJ to UV area $A_{WJ/UV}$; the total cross sectional reference area A_0; and the axial stretch λ_z, determined during experimental IE testing. The inner radius R_i; the model parameters c_1,k_1,k_2 and α; the radial ϵ_r and force $\epsilon_{\Delta F}$ fit errors; and the weight factor ω, determined during parameter optimization

	experimentally defined			fitted parameters					fit error		
UV&WJ	λ_z	$A_{WJ/UV}$	A_0 (mm^2)	R_i (mm)	c_1 (kPa)	k_1 (kPa)	k_2	α (deg)	ϵ_r	$\epsilon_{\Delta F}$	$1-\omega$ 10^{-3}
1	1.25	2.07	22.8	1.27	0.486	2.936	6.6	1.4	0.11	0.69	4.23
2	1.08	2.15	22.0	0.81	0.174	0.439	2.9	0.3	0.12	0.81	3.63
3	1.30	2.57	36.5	3.33	0.357	1.434	11.4	16.4	0.12	0.87	43.79
4	1.25	3.30	32.6	1.00	0.358	1.825	6.3	0.0	0.12	0.74	127.79
5	1.13	4.47	29.8	1.41	0.085	0.256	1.9	4.3	0.14	0.64	43.15
6	1.07	7.17	58.6	0.73	0.444	0.456	8.8	0.0	0.09	0.94	15.36
7	1.12	4.19	47.0	1.00	0.613	4.604	5.4	7.6	0.12	0.81	0.30
8	1.25	4.34	55.8	2.11	1.174	9.766	12.1	8.3	0.13	0.73	2.13
9	1.21	3.40	27.6	1.67	0.085	0.199	5.3	0.3	0.10	0.59	100.82
mean	1.18	3.74	37.0	1.48	0.420	2.435	6.8	4.3	0.12	0.76	37.91
std	0.08	1.48	12.9	0.77	0.317	2.939	3.3	5.3	0.01	0.10	44.24

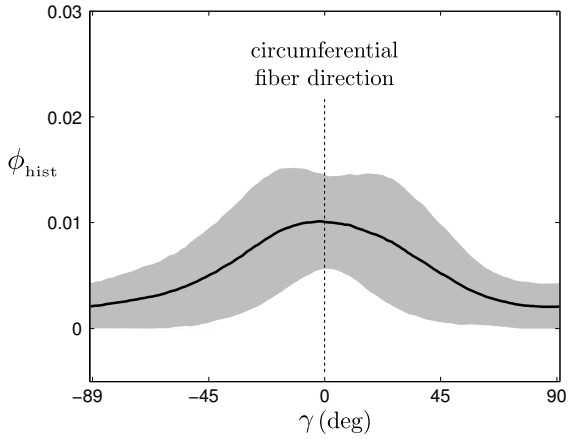

Figure 7.6 Normalized distribution of fibers angles (ϕ_{hist}) in the WJ from histology from a total of 43 stained WJ slices (Sec. 7.2.3), mean (solid line) and standard deviation at each angle (gray shaded area). The fiber distribution at each angle is normalized with the total fiber count in the 43 WJ slices so that $\sum_{j=1}^{N} \phi_{j,\text{hist}} = 1$, for the $N = 180$ fiber directions γ_j.

7.3.3 Parameters for comparison with the literature

The Bramwell-Hill pulse wave velocity c (Eq. 7.1) is calculated for the UV&WJ model, with the mean parameter set in Table 7.1 (with $\lambda_z = 1.0$). The resulting pulse wave velocity is plotted as a function of pressure in Fig. 7.7, giving increasing pulse wave velocity for increasing pressure,

caused by the stiffening effect of the increasing contribution from the fiber stress in the high pressure region.

The stiffness parameter b in an exponential pressure-area constitutive model (Eq. 7.3) is determined for the nine UV&WJ specimens by least square fitting, giving a mean value of $b = 8.55 \pm 4.22$.

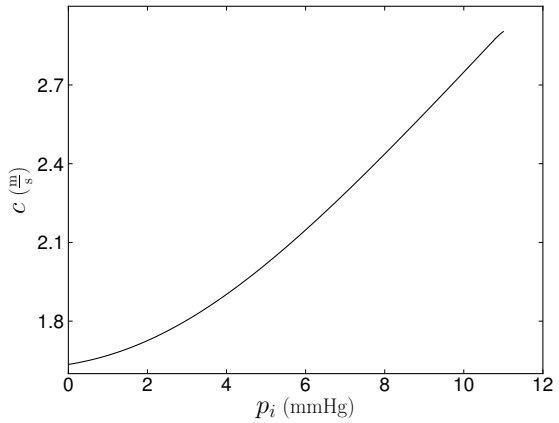

Figure 7.7 Pulse wave velocity c as a function of lumen pressure p_i for the UV&WJ model, with mean model parameters from Table 7.1 ($\lambda_z = 1.0$)

7.4 Discussion

In this study, experimental data and a structural model are presented for the passive and combined response of the human UV and surrounding WJ. The UV&WJ structural model contains three material parameters c_1,k_1,k_2, a main fiber angle α and fiber dispersion angle β. The model parameters c_1,k_1,k_2 and α are determined with an inverse optimization scheme, where the model response is fitted to experimental data obtained from IE tests on nine normal human UV&WJ specimens. The mean value of the material parameters derived from parameter optimization on IE data can provide a generic material description, as demonstrated by van den Broek et al. [184] in a study on porcine coronary arteries. Mean model parameters and SDs for the nine UV&WJ specimens are given in Table 7.1. The magnitude of the SDs may reflect the substantial biological variation commonly observed in fetal studies.

The UV&WJ model captures both the global behavior of the lumen pressure versus internal radius ($p_i - r_i$), and lumen pressure versus the change in the reduced axial force ($p_i - \Delta F_z$) for the nine samples reasonably well as seen in Fig. 7.5. However, there is a skewed difference in the fitted axial force and the measured axial force. Considerable variance is also present in the model parameters (see mean and std in Table 7.1), e.g. for the parameter k_2 associated with fiber stress, with standard deviation larger than the mean value.

Parameter optimization of the nine UV&WJ data sets (Table 7.1) resulted in a mean helical fiber angle of $\alpha = 4.3 \pm 5.3$ deg. The mean helical fiber angle found in the current study, for the

lumped response of the UV and surrounding WJ, is relatively low (circumferentially aligned) compared to studies in the literature, on other venous and arterial tissues. Rezakhaniha and Stergiopulos [163] reported a helical fiber angle of 32.6 deg in facial veins (rabbit), Zulliger et al. [196] reported a helical fiber angle of 35.0 deg and van den Broek et al. [184] reported a helical fiber angle of 34-37 deg in carotid arteries (porcine). The majority of the UV&WJ samples have a relatively tick layer of surrounding WJ, as seen in Fig. 7.4 and Table 7.1, which contributes to the structural integrity of the test species. The results given in Table 7.1 is inconclusive on how the amount of WJ affects the main helical fiber angle. However, a circumferential orientation of fibers in the WJ corresponds well with observations in the literature, where the orientation of collagen in the WJ close to the UV is reported to be mainly circumferential [8, 144]. Moreover, the histological study performed in the current work (Sec. 7.2.3) on the fiber angle distribution in the WJ, indicates that the majority of the fibers angles in the WJ are aligned around the circumferential direction, as seen in Fig. 7.6.

There is little evidence in the literature on the presence of axial pre-stretch of umbilical vessels, whereas axial pre-stretch is a normal and well described phenomenon for arteries and veins in other parts of the human and animal body [56, 89]. One might speculate that axial pre-stretch of umbilical vessels is somewhat unphysical due to the fact that the umbilical cord is a free floating organ in the amniotic fluid, attached to the placenta at one end and to the fetus at the other. However, with advancing pregnancy there is increasing possibilities for the cord to be entangled, winded around arms and legs, the fetal body or neck and thus under stretch and compression. Quite a proportion of neonates are delivered with the cord winded around the neck, and it is well documented that this mechanical impact must have lasted for some time since it affects birth weight and the ratio between birth weight and placental weight [164].

The exponential function (Eq. 7.3) given by Hellevik et al. [76] and Pennati [150] provides the opportunity to describe the pressure-area relation of the UV by a stiffness parameter b and the lumen area A_s at a standard pressure p_s=5mmHg. Pennati [150] reported a stiffness parameter of $b = 5.28 \pm 2.06$ for extracted UVs, and $b = 10.78 \pm 9.13$ for UVs within the intact umbilical cord. Hellevik et al. [76] reported a stiffness parameter $b = 4.0 \pm 1.0$ for the intra-abdominal portion of fetal lamb UVs, located at the entrance to the liver. The stiffness parameter is determined for the nine UV&WJ data sets resulting in $b = 8.55 \pm 4.22$. Hence, the stiffness parameter in the current study falls between the stiffness parameters for the extracted UV and the UV within the umbilical cord reported by Pennati [150]. This result is reasonable when considering that the amount of WJ around the UV will influence the overall UV stiffness. Hellevik et al. [76] studied the intra abdominal part of the UV in fetal lambs, and therefore a direct comparison is difficult. It is, however, interesting to note that no WJ is present around the UV located in the fetal abdomen, and that Hellevik et al. [76] found relatively low stiffness $b = 4.0 \pm 1.0$, compared to the findings in the current study and the study by Pennati [150]. The pulse wave velocity c (Eq. 7.1) as a function of lumen pressure is calculated for the UV&WJ model, as seen Fig. 7.7, and is comparable but somewhat higher than what has been reported before by Hellevik et al. [76].

7.4.1 Limitations

The UV&WJ test specimens contain both the UV and an outer layer of WJ (Fig. 7.4). This is to some extent a consequence of the sample preparation, as it proved difficult to separate the UV and WJ. Similar difficulties have been reported by Pennati [150] and Daniel et al. [36]. However, the UV lacks the normal adventitia found in most arteries and veins, and it has been suggested that the surrounding WJ can be regarded as a part of the structural integrity of the UV [47, 144, 150]. The structural properties of the UV and the outer layer of WJ, are in this work lumped into one UV&WJ material model. This modeling choice is a significant simplification, since the UV with the outer layer of WJ represents a two layer structure. The structural components in UV&WJ model is adopted based on the histological description of the UV and WJ in literature. WJ has been described as an elastic collagen-based extracellular matrix [47], whereas the UV has been described as similar to other cardiovascular tissues with respect to elastin, collagen and smooth muscle cells content [123].

The uniformity of the vessel wall thickness and a circular cross section, received special attention during selection and preparation of the UV&WJ test specimens. These two requirements proved difficult to meet in practice. Individual variation in wall thickness are present in the specimens in the sample population. This is also true for the circular shape of the cross sections, which for some samples proved to be elliptic in the unloaded state (see Fig. 7.4b). The numerical model of the UV&WJ specimens in this work is based on the assumption of cylinder with uniform wall thickness and a circular cross section. Hence, the difference in the geometrical shape of the test samples and the numerical model is a limitation of the current study, and may be a cause of the high SD found in the material parameters.

The umbilical cords samples in the current study were preserved from the time of delivery (birth) to mechanical testing by refrigeration to 4^{o}C. The time period from delivery to mechanical testing was 17.5h$\pm$6.2h. The method of preservation and the time span from tissue collection to mechanical testing has be shown to influence the mechanical properties of vascular tissue several studies, e.g. Stemper et al. [176] and Chow and Zhang [33]. Stemper et al. [176] found a significant drop in stiffness (Young's modulus) in uni-axial tension test of refrigerated arterial tissue compared to fresh tissue. Chow and Zhang [33] found similar results for aortic refrigerated tissue compared to fresh tissue in biaxial tests in the low strain region, but stiffer behavior in the high strain region. Hence, it is reasonable to assume that the post harvesting treatment and storage method affected the mechanical properties of the umbilical cord specimens in the current study. However, the impact of different tissue treatment and storage techniques on the mechanical properties was not investigated in the current study, and therefore represents a limitation in the presented experimental and parametric results.

The umbilical cord vessels, the UV and the two arteries, are coiled around each other in a helically arranged spiral. The variance in umbilical coiling is large, and some umbilical cords are more or less straight [46]. IE testing (as given in Sec. 7.2.1) requires a straight test specimen. Therefore, during UV&WJ sample preparation, the selection of a relatively straight section of the umbilical cord had priority over a specific position along the length of the cord. Although, Li et al. [122] reported stiffer mechanical properties for the proximal (placental) end compared to the distal (fetal) end of human umbilical cords. Furthermore, it was discovered

during dissection of the cord (Sec. 7.2.2) that the extracted UV&WJ specimens (and arteries) preserved some of the helical twist giving the majority of test specimens a corkscrew shape, illustrated schematically in Fig. 7.2. The initial corkscrew shape of the UV&WJ specimens meant that some of the initial axial displacement $\Delta L = L(\lambda_z - 1)$ not only contributed to the axial stretch but also to straightening of the samples. Hence, the magnitude of the axial force F_z found in the IE experiments may have been underestimated with respect to the applied axial stretch. Additionally, the initial corkscrew shape was not taken into account in the numerical model of the UV&WJ specimens.

Residual strains were not accounted for in this work, although strong evidence of residual strains was observed during dissection of the UV&WJ specimens. Residual strain would alter the stress distribution in the vessel wall, and therefore influence the value of the material parameters found during parameter optimization. The importance of residual strain in cardiovascular vessels has been demonstrated by several authors [34, 82], and including the effect of residual strains would be interesting in future studies on the mechanical properties of UVs and WJ.

7.4.2 Conclusion

In conclusion, the UV&WJ model describes the radial expansion and reduced axial force seen in the IE tests, reasonably well. There are however, considerable variance in the material parameters. The variance may reflect the substantial biological variation commonly observed in fetal studies. Modeling improvements may include a two layer model of the UV and WJ, and/or refinements with respect to elastin and collagen content, distribution and micro structure in both the UV and WJ. Further experimental testing of the separate properties of the UV and the WJ is also called for.

Chapter 8

Velocity profiles in the human ductus venosus: a numerical fluid structure interaction study

The content of this chapter was in 2012 accepted for publication in the journal of Biomechanics and Modeling in Mechanobiology

Velocity profiles in the human ductus venosus: a numerical fluid structure interaction study

P.R. Leinan, J. Degroote, T. Kiserud, B. Skallerud, J. Vierendeels and L.R. Hellevik

8.1 Introduction

The veins distributing oxygenated blood from the placenta to the fetal body have been given much attention in the literature, especially in Doppler velocimetry studies [17, 112, 115, 131]. One of the most prominent is the ductus venosus (DV), which bypasses the right liver lobe delivering oxygen rich blood directly to the inferior vena cava (IVC), and thus the heart [103]. The DV forms a bifurcation with the intra abdominal umbilical vein (IUV), and the left portal vein (LPV). Furthermore, the LPV is connected to the right portal vein (RPV) and the main portal stem (PV), which delivers blood low on oxygen to the right liver lobe, from the lower fetal body. The LPV-RPV-PV junction is therefore described as a watershed between oxygen rich blood from the placenta and oxygen poor blood from the intestine and spleen (Fig. 8.1) [99, 113].

Information about the blood volumetric flow rate through the DV has been made possible from Doppler velocimetry combined with detailed knowledge about the local hemodynamics [111, 151]. The volumetric flow rate $Q = V_{\text{mean}}A$ through a vessel can be found from the cross sectional mean velocity V_{mean} and the cross sectional area A of the vessel (see Sec. 8.2). Accurate measurements of the cross sectional mean velocity are not easily accessible through standard ultrasonography in a clinical setting [111]. However, the cross sectional mean velocity can be estimated from $V_{\text{mean}} = hV_{\max}$, where $V_{\max}$ is the cross sectional maximum velocity (e.g. from the Doppler tracing) and where h indicates the shape of the local cross sectional velocity profile (see Sec. 8.2). The velocity profile shape coefficient (VC), h, at the DV inlet has been investigated with CFD analysis by Pennati et al. [151] and with ultrasonography by Kiserud et al. [111], reporting $h = 0.68$ and $h = 0.69$ respectively. A VC of $h = 1.0$ and $h = 0.5$ indicate a flat and parabolic velocity profile respectively. Hence, the VC found by Pennati et al. [151] and Kiserud et al. [111] indicates a partially flat profile at the inlet of the human DV.

The degree of DV shunting has been investigated in several studies in the later stages of human fetal gestation [16, 17, 95, 96, 112, 115]. The blood flowing from the placenta through the UV and into the IUV first supplies the left liver lobe through minor veins along the IUV. A portion of the blood volume is then shunted through the DV, while the remaining blood volume enters the LPV and the right liver lobe [99] (Fig. 8.1). Haugen et al. [70] quantified the flow split between DV and the IUV immediately downstream of the DV to be 56%, for normal human fetuses at 36 weeks of gestation. The flow split between DV and the blood volume from the placenta is found to be 20-30% in studies on human fetuses [16, 70, 115, 180], depending on factors such as gestational age. Kiserud et al. [115] reported a shunt fraction of 32% at 18 weeks gestation, a decrease to a minimum of 18% at 31-34 weeks followed by an increase to 22% at 40 weeks, in normal pregnancies. In a subsequent study, Kiserud et al. [112] reported that the DV shunt fraction may increase significantly in umbilical circulatory compromise, such as intrauterine growth restriction (IUGR), especially for fetuses with an absent or reversed end-diastolic DV blood velocity. Several studies have shown that the DV shunt fraction may increase in the case of IUGR [17, 112, 179], and in some cases shunt fractions above 100% have been reported [17, 112], suggesting that the blood from the LPV is drained into the DV, i.e. a reversed flow direction in the LPV compared to the normal case (Fig. 8.1) [99, 101].

The distribution of oxygenated blood volume at the IUV-DV junction is of considerable

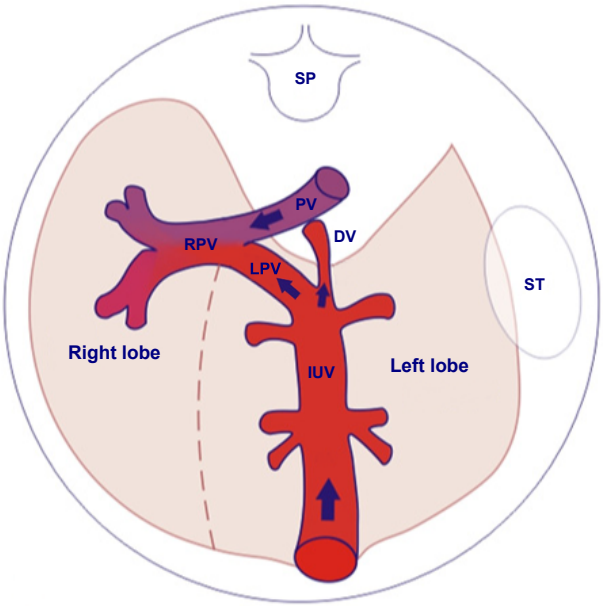

Figure 8.1 Illustration of a typical pattern of venous blood supply of the fetal liver (left and right liver lobe) in normally growing fetus. DV, ductus venosus; LPV, left portal vein; PV, main stem of the portal vein; RPV, right portal vein; SP, spine; ST, stomach; IUV, intra abdominal umbilical vein. The view plane is seen in the superior direction, i.e. towards the upper fetal body. Adapted from Kessler et al. [96]

physiological interest, however it is the recording of the DV blood velocity waveform that has caught the highest clinical interest [105]. DV velocity waveform parameters are now in common use for assessing and monitoring compromised pregnancies. Recently the magnitude and direction of the blood velocity in LPV has been added as another monitoring parameter [99].

The velocity in the human DV is pulsatile in normal pregnancies [108]. The pulsations originate from the fetal heart and propagate from the right atrium, through the IVC and into the DV [113]. The DV velocity wave form in normal fetuses can be recognized from a maximum peak during ventricular systole and a second peak during diastolic filling. An often sharp velocity reduction is present during atrial contraction, in some cases to the point of flow reversal in the DV [73, 107]. DV flow reversal is abnormal in the later stages of gestation, but may be found at an early gestational age in normal fetuses [113, 126].

Doppler velocimetry of the DV shunt is in widespread clinical use, especially in the later stages of gestation. DV ultrasonography can identify pathologies such as hypoxaemia, acidosis, cardiac decompensation and placental compromise, and is a promising tool for timing the delivery of critically ill fetuses [103]. Furthermore, DV velocimetry in early pregnancy can give indications on chromosomal defects, specifically in the presence of abnormal and reversed flow during atrial contraction [103, 126, 130, 182].

The interpretation of Doppler signals from the DV, and especially estimating volumetric flow rate is not straightforward. The DV diameter is small and reported to be between 0.5 and 2.0 mm [115]. Furthermore, the trumpet shape of the DV [134], combined with the branching

angle from the attachment point at the IUV gives rise to complex hemodynamics and a non-symmetric velocity profile [151]. Additionally, the ratio between the maximum and minimum diameter at the DV inlet during a cardiac cycle, characterized by the diameter pulse index (DPI) (see Eq. 8.9), was found to vary with a mean and median value of 0.21 and 0.05, respectively in a study by Acharya and Kiserud [1]. Considering these factors, the quantification of the volumetric flow rate shunted through the DV is a challenge. These challenges add to the normal difficulties faced in volumetric flow rate estimation with Doppler ultrasound, such as beam angle, mean flow calculation and vessel area estimation [85].

In this work a numerical study is presented on the hemodynamics in the IUV, DV and LPV bifurcation. The primary aim of the study is to investigate velocity profiles at the DV inlet region under normal conditions in the later stages of gestation, aimed at volumetric flow rate assessment with Doppler velocimetry. The numerical model includes the IUV, DV and LPV and takes into account the deformation of the vessels from the pressure and viscous forces of the blood flow through fluid structure interaction (FSI). Lumped models for the UV, IVC and the right liver lobe (HeR) are included boundary conditions for the FSI model. Additionally, CFD simulations (with rigid walls) with the same boundary conditions as the FSI simulations are included to investigate the effect of the wall compliance. The secondary aim of the study, is to advance the development of numerical models of the fetal venous system, especially of the DV, LPV and IUV bifurcation, which can supplement previous models presented in the literature [77, 79, 151, 153, 154]. The developed FSI model has the potential for further investigation of the VC in DV, LPV and IUV bifurcation during physiological and pathological conditions, and detailed cases studies on e.g. DV dilatation [18], and wave transmission from the fetal heart into the DV/IVU junction [79].

8.2 Materials and methods

8.2.1 Flow parameters

The volumetric flow rate rate $Q(t)$ passing a cross-section with area $A(t)$ at time t can be calculated from

$$Q(t) = V_{\text{mean}}(t)\ A(t), \tag{8.1}$$

where $V_{\text{mean}}(t)$ is the cross sectional mean velocity defined by

$$V_{\text{mean}}(t) = \frac{1}{A(t)} \int_{A(t)} [\mathbf{V}_A(t) \cdot \mathbf{n}_A(t)]\, dA. \tag{8.2}$$

where $\mathbf{n}_A(t) \perp A(t)$ is the cross sectional normal vector, and $\mathbf{V}_A(t) = \mathbf{V}(\mathbf{z}, t) \in A(t)$ is the velocity vector in the cross-section, at a spatial location $\mathbf{z} = [x, y, z]^T \in A(t)$.

Accurate measurements of the cross sectional mean velocity is not easily available through standard Doppler ultrasound techniques [111]. However, the cross sectional mean velocity can

be estimated from the maximum velocity in the cross-section

$$V_{\max}(t) = \max_{\mathbf{z} \in A} [\mathbf{V}_A(t) \cdot \mathbf{n}_A(t)] \tag{8.3}$$

combined with knowledge about the local cross sectional VC, $h\,(t)$, giving

$$V_{\text{mean}}(t) = h\,(t)\; V_{\max}(t). \tag{8.4}$$

The VC indicates the shape of the cross sectional velocity profile, however, different velocity profiles with the same h value exists. The VC for a parabolic velocity profile in fully developed laminar pipe flow is $h = 0.5$, whereas $h = 1.0$ corresponds to a completely flat velocity profile i.e. the cross sectional mean velocity is equal to the cross sectional maximum velocity.

In this work we define an averaged VC, $\overline{h}$, during the cardiac cycle, given by:

$$\overline{h} \equiv \frac{\overline{Q}}{\overline{V}_{\max}\,\overline{A}}, \tag{8.5}$$

where the time averaged volumetric flow rate $\overline{Q}$, cross sectional area $\overline{A}$, cross sectional maximum velocity $\overline{V}_{\max}$ are calculated from

$$\overline{\bullet} = \frac{1}{T}\int_T \bullet(t)dt, \tag{8.6}$$

and where T represents the period of one cardiac cycle.

The time averaged volumetric flow rate $\overline{Q}$ over one cardiac cycle can now be estimated from Doppler ultrasound as the product of the measured time averaged maximum cross sectional velocity, the measured time averaged cross sectional area, and the averaged VC from Eq. 8.5 which is estimated in our simulations:

$$\overline{Q} \simeq \overbrace{\overline{h}}^{\text{simulations}}\; \underbrace{\overline{V}_{\max}\;\overline{A}}_{\text{measurements}} \tag{8.7}$$

The pulsatility index for veins (PIV) during a cardiac cycle is defined as

$$\text{PIV} = \frac{\max_{t\in T}[V_{\max}(t)] - \min_{t\in T}[V_{\max}(t)]}{\overline{V}_{\max}}, \tag{8.8}$$

where $\max_{t\in T}[V_{\max}(t)]$ is the peak velocity during ventricular systole and $\min_{t\in T}[V_{\max}(t)]$ is the minimum velocity during atrial contraction [74, 111]. Furthermore, following Acharya and Kiserud [1] we define the diameter pulse index (DPI)

$$\text{DPI} = \frac{\max_{t\in T}[D(t)]}{\min_{t\in T}[D(t)]} - 1, \tag{8.9}$$

where $\max_{t\in T}[D(t)]$ and $\min_{t\in T}[D(t)]$ are the maximum and minimum vessel diameters recorded during a cardiac cycle, and $D(t) = 2\sqrt{A(t)/\pi}$.

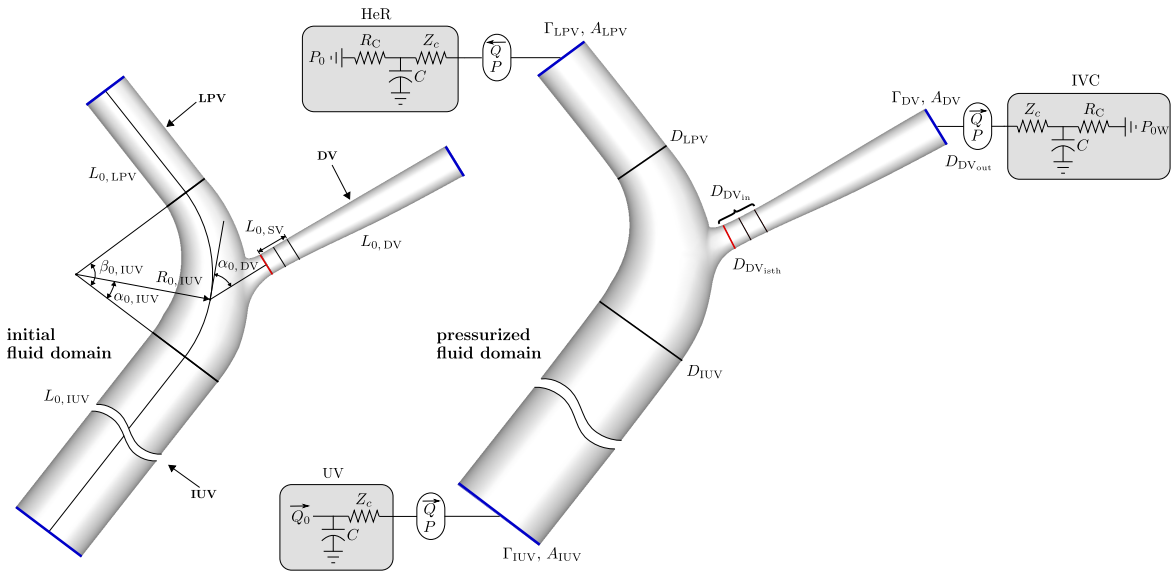

Figure 8.2 *Fluid and lumped models*: Overview of the fluid domain of the IUV, DV and LPV bifurcation in the initial and loaded state. *Initial fluid domain*: Vessel lengths and angles for the initial geometry of the fluid domain. *Pressurized fluid domain*: The loaded fluid domain at reference flow and pressure, with lumped models for the UV, IVC and HeR. The lumped models are connected to the 3D fluid domain at the surfaces Γ_{IUV}, Γ_{DV} and Γ_{LPV}. *Note*: The diameter $D_{\text{DV}_{\text{in}}}$ is calculated as the mean of three cross-sections in the DV inlet region, with an initial sample volume length of $l_{0\,\text{SV}} = 2\,\text{mm}$ (see Sec. 8.2.2)

8.2.2 Numerical model

A 3D FSI model of the IUV, DV and LPV bifurcation is presented in this work, based on a fetus of 36 weeks of gestation [70]. The FSI problem is solved with a partitioned strategy, with black box solvers for the fluid (*Ansys, Fluent*) and solid (*Abaqus FEA*). An in house code (*Tango*) is used to implicitly couple the FSI problem with the interface quasi-Newton (IQN) approach [38, 187]. Lumped models (0D) for the UV, HeR and IVC are included as boundary conditions for the FSI problem.

Initial geometry

An overview of the initial geometry of the fluid domain of the IUV, DV and LPV bifurcation is shown in Fig. 8.2. The IUV and LPV are modeled as straight tubes, connected to a curved section with a tract angle $\beta_{0,\,\text{IUV}}$ and a mean curvature radius $R_{0\,\text{IUV}}$. The DV is modeled as a conical shaped diverging tube from the DV isthmus, where the DV intersects the LPV-IUV with a branch angle of $\alpha_{0\,\text{DV}}$. The shape of the bifurcation including the conical shape of the DV is based on the histological studies presented by Mavrides et al. [134], Mavrides et al. [133] and Kivilevitch et al. [117]. The minor (portal) veins connecting the IUV to the left liver lobe, as seen in Fig. 8.1, are neglected in the current study.

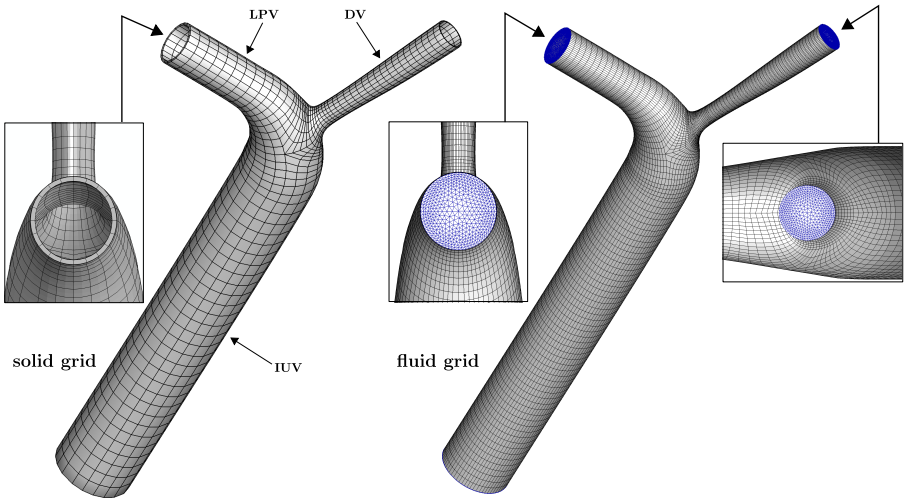

Figure 8.3 *Grid details and quality*: Grid details for a typical solid and fluid grid in a loaded state (grid refinement 3, Table. 8.5). *Solid grid*: 20 node continuum hybrid elements with reduced integration (C3D20RH). *Fluid grid*: Wedge volumes, and boundary layer resolution close to the fluid structure interface.

Table 8.1 Common parameters for the IUV, DV and LPV bifurcation, as seen in Fig. 8.2.

	L_0 (mm)	R_0 (mm)	β_0(deg)
LPV	7.5		
DV	12.5		
IUV	35.0	8.0	75

The diameter to wall thickness ratios (D/H) are calculated from the studies of Ailamazyan et al. [2] and Haugen et al. [70] giving initial wall thickness ratios equal to 11, 6, 18 and 11 for the LPV, DV_{isth}, DV_{out} and IUV respectively.

Parametric study

A parametric study including nine dynamic FSI simulations of the IUV, DV and LPV bifurcation is constructed from a reference case, by variation of the branch angles $\alpha_{0\,\text{DV}}$ and $\alpha_{0\,\text{IUV}}$; the diameters of the IUV (D_{IUV}), DV isthmus ($D_{\text{DV}_{\text{isth}}}$) and outlet ($D_{\text{DV}_{\text{out}}}$); and the amplitude of the pulsatile pressure waveform in the IVC, $P_{0W,\text{IVC}}(t)$. Geometrical parameters common for the all test cases are given in Table 8.1. The reference case is created with parameters for a normal fetus of 36 weeks of gestation, determined by *in-vivo* ultrasound data from the work of Haugen et al. [70], Kiserud et al. [110] and Acharya and Kiserud [1].

The parameters and parametric range included in the parametric study are chosen to represent some of the physiological variation in the human IUV, DV and LPV bifurcation, which can influence the VC at the DV inlet, e.i. the diameter of the DV and the IUV (from Haugen et al. [70] and Kiserud et al. [110]); the angle of insertion between the DV and the IUV (from

Beaudoin et al. [15] and Pennati et al. [151]); and the pulsation in the DV (from Kessler et al. [97]).

A sample volume is utilized while measuring the DV inlet velocities with Doppler ultrasound [111]. In this numerical study we therefore choose to middle the measurements at the DV inlet over a region of 2mm, which corresponds to a sample volume commonly used in Doppler velocimetry in a clinical setting. This is achieved by taking the mean of the measured quantities in the DV inlet region over three cross-sections, as illustrated in Fig. 8.2, for the diameter $D_{\text{DV}_{\text{in}}}$, with the initial sample volume length $L_{0,\,\text{SV}} = 2\,\text{mm}$. Similarly, velocities at the DV inlet region $V_{\text{DV}_{\text{in}}}$ are calculated as the mean of the velocities at the three cross-sections defined by $D_{\text{DV}_{\text{in}}}$.

Grid quality

Fluid and solid grid details are seen in Fig. 8.3 at physiological flow and pressure (grid refinement 3, Table. 8.5). The fluid grid is constructed of wedged volumes, with enhanced grid resolution close to the fluid structure interface. The solid grid is constructed of quadratic 20 node continuum hybrid elements with reduced integration (C3D20RH).

Fluid formulation

The fluid is modeled as an incompressible Newtonian fluid, with density ρ_f =1060 kg m^{-3} and viscosity μ =4.0 cP. The momentum and mass conservation equations are given by

$$\rho_f \frac{\partial \mathbf{u}}{\partial t} + \rho_f((\mathbf{u} - \mathbf{u}_g) \cdot \nabla)\,\mathbf{u} - \mu\nabla^2\mathbf{u} + \nabla p = \mathbf{0}, \tag{8.10}$$

$$\nabla \cdot \mathbf{u} = 0, \tag{8.11}$$

where $\mathbf{u}$ and p are the velocity and the pressure at a location in the fluid domain, and $\mathbf{u}_g$ is the local grid velocity. The *Ansys, Fluent* computational fluid dynamics solver is used to solve the flow problem on a moving/deforming grid, with a no-slip condition on the fluid structure interface. Pressure boundary conditions are applied at each of the end surfaces, Γ_{IUV}, Γ_{DV} and Γ_{LPV}, of the 3D flow domain. The boundary pressures P_i (where $i = \{\text{IUV,DV,LPV}\}$) are given by lumped models, see Sec. 8.2.2), and uniformly distributed on each end surface (Fig. 8.2).

Structural formulation

Experimental data and models for the structural response of IUV, DV and LPV veins are scarce in the literature [76], however more is known about their structural composition. The structural composition of the DV have been studied most extensively [2, 134, 136, 178], and limited morphological descriptions can be found for fetal veins entering the liver [178] and of the IUV [129]. The veins are described as similar to other venous tissues containing muscular, elastin and collagen fibers. The structural response of elastin and collagenous tissue can be modeled with the hyperelastic strain energy potential [83] (neglecting viscoelastic effects)

$$\Psi(\mathbf{C}) = c_1(I_1 - 3) + \frac{k_1}{2k_2}(\exp[k_2\,(I_1 - 3)^2] - 1) \tag{8.12}$$

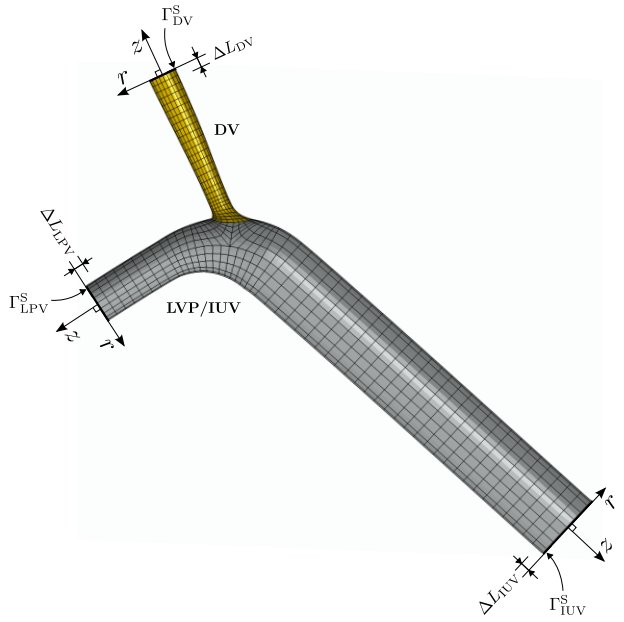

Figure 8.4 *Structure with boundary conditions and materials*: The structural grid in a loaded state, with two hyperelastic materials visualized with grey and yellow grid color for the LPV/IUV and DV respectively. The structural grid is constrained at the end surfaces Γ^{S}_{IUV}, Γ^{S}_{DV} and Γ^{S}_{LPV}, defined by local cylindrical coordinate systems (r, θ, z). Nodes on the end surfaces are free to move in the radial direction (r) and constrained in the angular direction (θ). Furthermore, the end surfaces nodes are constrained in the local z-direction, after a forced displacement of ΔL.

where $I_1 = \text{tr}(\mathbf{C})$ is first invariant of the right Cauchy-Green deformation tensor $\mathbf{C}$, and c_1, k_1, and k_2 are material parameters. The Neo-Hookean part of the strain energy potential given by the material parameter c_1 describes the elastic behaviour in the low pressure region. The stiffening effect in the high pressure region caused by increasing recruitment of collagen fibers is modeled with an exponential function of I_1, with material parameters k_1, and k_2. The anisotropic orientation of collagen fibers found in most vascular tissues is neglected in the current study, and the exponential term in Eq. 8.12 models an isotropic distribution of collagen fibers [59].

The structural problem is solved with the *Abaqus FEA* implicit structural solver, giving the Cauchy stresses

$$\boldsymbol{\sigma} = \frac{2}{J}\,\mathbf{F}\frac{\partial \Psi}{\partial \mathbf{C}}\mathbf{F}^{T}, \tag{8.13}$$

where $J = \det \mathbf{F} > 0$ is the volume ratio and $\mathbf{F}$ the deformation gradient tensor.

The material properties are different for the LPV/IUV and the DV, as seen in Fig. 8.4, visualized with grey and yellow grid color for the LPV/IUV and the DV respectively. The material parameters are given by experimental data from *in-vitro* inflation test on the DV and IUV of fetal sheep fetuses, in a study by Hellevik et al. [76]. The material parameters, given in Table 8.2, are derived from least square fitting of four individual data sets for the DV and

Table 8.2 *Material parameters*: Hyperelastic material parameters for the LPV/IUV and DV.

	c_1 (Pa)	k_1 (Pa)	k_2 (-)
LPV/IUV	1320.5	702.0	5.5
DV	374.4	1128.9	6.2

IUV respectively, see Leinan et al. [120] for details on the parameter estimation procedure. The density for all veins is set to 1200 kg m^{-3}.

The solid is constrained at the end surfaces $\Gamma^{\text{S}}_{\text{IUV}}$, $\Gamma^{\text{S}}_{\text{DV}}$ and $\Gamma^{\text{S}}_{\text{LPV}}$ (Fig. 8.4). The constraints are defined by local cylindrical coordinate systems (r, θ, z), where the z-axis is aligned with the local outwards facing surface normal. Nodes on the end surfaces are free to move in the radial direction (r) and constrained in the angular direction (θ), relative to the corresponding local cylindrical coordinate system. Additionally, the surface nodes are constrained along the local z-axis, with the forced displacements ΔL_i (where $i = \{\Gamma^{\text{S}}_{\text{IUV}}, \Gamma^{\text{S}}_{\text{DV}}, \Gamma^{\text{S}}_{\text{LPV}}\}$) in the positive z-direction. The displacements ΔL_i apply some initial axial stretch to the IUV, DV and LPV veins, and are introduced because of the initial softness of the hyperelastic LPV/IUV and DV materials. The magnitude of the initial axial stretches are chosen to prevent buckling of the veins and preserve the initial shape of the IUV, DV and LPV bifurcation at physiological pressure.

Table 8.3 *Lumped parameters*: Lumped model parameters for the UV, IVC and HeR (Fig. 8.2).

	R_C $\left(\frac{\text{mmHg s}}{\text{ml}}\right)$	C $\left(\frac{\text{ml}}{\text{mmHg}}\right)$
UV		0.3
IVC	0.04	0.4
HeR	0.16	3.0

Lumped models

The lumped (0D) parameter system consists of three sub-models. Two, three-element Windkessel (3WK) are imposed at LPV and DV outlets, and a single UV compartment is connected to the IUV inlet [52], as seen in Fig. 8.2. The HeR 3WK at the LPV outlet represents the right liver lobe. The IVC 3WK at the DV outlet represents the section of the IVC that connects the DV to the right atrium. The UV compartment at the IUV inlet represents the amniotic portion of the UV which is embedded in the umbilical cord from the placenta insertion point to the umbilical navel.

The 3WKs models are governed by the differential equation

$$\frac{dP}{dt} + \frac{(P - P_0)}{R_C C} = Z_c \frac{dQ}{dt} + Q \frac{dZ_c}{dt} + Q \left(\frac{1}{C} + \frac{Z_c}{R_C C} \right), \tag{8.14}$$

and the UV compartment is governed by the differential equation

$$\frac{dP}{dt} = -Z_c \frac{dQ}{dt} - Q \frac{dZ_c}{dt} + \frac{(Q_0 - Q)}{C}, \tag{8.15}$$

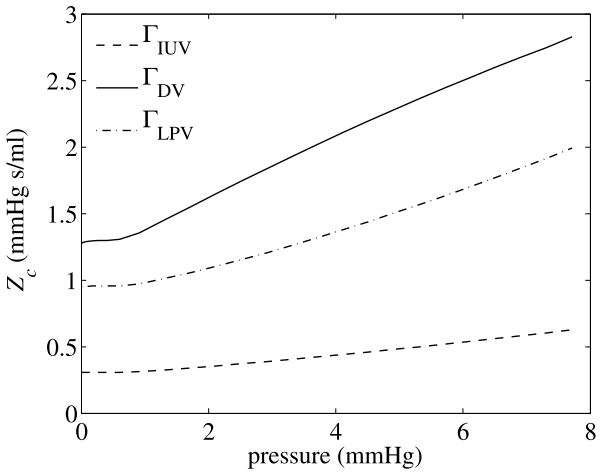

Figure 8.5 *Characteristic impedance*: Characteristic impedance (Eq. 8.16) pressure dependency for the reference parametric case 2, at the interfaces Γ_{IUV}, Γ_{DV} and Γ_{LPV}, calculated in static structural analysis

where $P = P(t)$ and $Q = Q(t)$ are the pressure and volumetric flow rate at the 3D fluid domain surfaces Γ_{IUV}, Γ_{DV}, which enters the characteristic impedance $Z_c = Z_c(t)$ (Fig. 8.2). The reservoir pressure $P_0 = P_0(t)$ is used as a force term for the HeR and IVC 3WK models (Eq. 8.14). For the UV compartment representing the UV, flow rate is imposed by Q_0 (Eq. 8.15) which is the volumetric flow rate entering the UV from the placenta. Furthermore, R_C is the lumped resistance element in the 3WK and C is the lumped compliance. Lumped model parameters for the UV, IVC and HeR are given in Table 8.3 [88, 152]. The characteristic impedance is given by

$$Z_c = \frac{\rho_f}{A} c(P), \tag{8.16}$$

where the pulse wave velocity $c(P)$ is a function of lumen pressure P, and where A is the cross sectional lumen area of the 3D vessels terminated by the lumped models. Hence, the impedances Z_c of lumped models are set equal to the characteristic impedance of the ith interface Γ_i of the 3D vessels, where $i = \{\text{IUV,DV,LPV}\}$.

The lumped model configurations and parameters are determined from preliminary simulations on the reference case (see Sec. 8.2.2). The preliminary simulations shows that WK3 models at the LPV and DV outlets, with characteristic impedance Z_c (Eq. 8.16), and R_C and C values adapted from Huikeshoven et al. [88], Pennati et al. [152] gives a numerical flow split equal to the flow split reported by [70] ($\overline{Q}_{\text{DV}}/\overline{Q}_{\text{IUV}} = 0.56$) for a normal fetus at 36 weeks of gestation.

The pressure dependency of the pulse wave velocities at the interfaces Γ_{IUV}, Γ_{DV} and Γ_{LPV} (Fig. 8.2) is estimated by a separate static structural analysis on the IUV, DV and LPV bifurcation. A uniform pressure is applied to the inner surface of the solid, and the pulse wave velocities are calculated from the Bramwell-Hill equation [29] for different pressure levels. The pressure dependency of the characteristic impedance, Eq. 8.16, for the reference parametric case 2 at interfaces Γ_{IUV}, Γ_{DV} and Γ_{LPV}, can been seen in Figure 8.5.

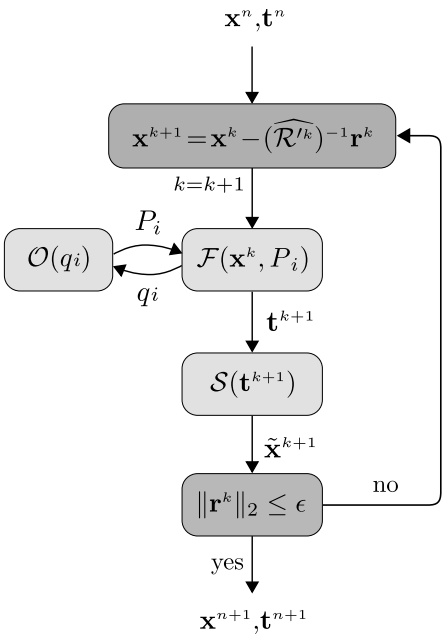

Figure 8.6 *FSI and lumped model coupling*: Schematic overview of the coupling procedure of the fluid structure problem, solved in a partitioned way with the interface quasi-Newton (IQN) approach [38, 187]. Illustrating the lumped models $\mathcal{O}$, the fluid $\mathcal{F}$ and structural solver $\mathcal{S}$, where n is the time-step counter; k, is the FSI sub-iteration counter; ϵ, is the FSI convergence criterion (remaining parameters are explained in Sec. 8.2.2)

Coupling procedure

The following outlines the procedure to couple and solve the lumped models, flow and structure, as a 3D-0D FSI model of the IUV, DV and LPV bifurcation.

- *Lumped 0D model to 3D fluid coupling*

Backward Euler is used to advance the lumped models in time, to match the time discretization in the fluid solver (see Appendix) [186].The lumped models $\mathcal{O}$ return the pressures

$$P_i = \mathcal{O}(q_i), \tag{8.17}$$

imposed as pressure boundary conditions on the fluid boundaries Γ_i where $i = \{\text{IUV,DV,LPV}\}$ as seen in Fig. 8.2. The lumped model forcing variables $q_i = \{A_i^{**}, Q_i^*, P_i^*\}$, are given by;

$$q_i = \begin{cases} A_i^{**} & = A_{\text{3D},\,i} = \int_{\Gamma_i} d\gamma \\ Q_i^* & = Q_{\text{3D},\,i} = \int_{\Gamma_i} \mathbf{u}_i \cdot \mathbf{n}_i \, d\gamma \\ P_i^* & = P_{\text{3D},\,i} = \frac{1}{A_{\text{3D},\,i}} \int_{\Gamma_i} p_i \, d\gamma. \end{cases} \tag{8.18}$$

where $\mathbf{u}$ and $\mathbf{n}$ are the velocity and unit normal vectors at the faces of each ith interface Γ_i of the 3D fluid domain [52, 137]. The unit normal vectors $\mathbf{n}$ are pointing out of the fluid domain for interfaces Γ_{DV} and Γ_{LPV}, and into the fluid domain for the Γ_{IVU} interface. The lumped model

forcing variables (Eq. 8.18), Q_i^* and P_i^* denoted with a star, are updated each flow iteration in the fluid solver. By contrast, the vessel cross sectional area denoted with a double star A_i^{**} is updated each FSI iteration (see 8.4).

- *FSI coupling procedure*

The fluid structure problem is solved in a partitioned way with the interface quasi-Newton (IQN) approach [38, 187]. The partitioned coupling procedure is outlined in Figure 8.6, with separate solver for the fluid ($\mathcal{F}$) and structure problem ($\mathcal{S}$). Dirichlet-Neumann FSI partitioning is used, in which the flow is computed for a given displacement $\mathbf{x}$ of the fluid structure interface and boundary pressures P_i (Eq. 8.17), giving the traction stress vector $\mathbf{t} = \mathcal{F}(\mathbf{x}, P_i)$ on the fluid structure interface. The traction vector is passed to the structural solver which calculates an update of the fluid structure interface displacement given by $\mathbf{x} = \mathcal{S}(\mathbf{t})$. The coupled FSI problem is defined by;

$$\mathcal{R}(\mathbf{x}) = \mathcal{S} \circ \mathcal{F}(\mathbf{x}, P_i) - \mathbf{x} = \mathbf{0}, \tag{8.19}$$

where $\mathcal{R}$ is a residual operator in a root finding formulation for the fluid structure interface displacement $\mathbf{x}$ [187]. The FSI problem is solved with quasi Newton iterations such that the update in fluid structure interface displacement is given by;

$$\mathbf{x}^{k+1} = \mathbf{x}^k - \widehat{(\mathcal{R}'^k)^{-1}}\mathbf{r}^k, \tag{8.20}$$

where $\mathbf{r}^k$ is the residual and $\widehat{(\mathcal{R}'^k)^{-1}}$ is an approximation for the inverse of the Jacobian of $\mathcal{R}$ evaluated at $\mathbf{x}^k$ [39]. The FSI coupling procedure is handled by an in-house code *Tango*, in which updates of the interface displacement $\mathbf{x}^{k+1}$ and the approximate Jacobian $\widehat{(\mathcal{R}'^k)^{-1}}$ are evaluated as given in Eq. 8.20. Interpolation between 3 points is used to match the transfer of displacement $\mathbf{x}$ and surface traction stress $\mathbf{t}$ from the different (non-conforming) grid layouts of the fluid and structural solvers, at the fluid structure interface. Furthermore, the arbitrary Lagrangian-Eulerian method is used in the fluid solver to handle grid deformation in the fluid domain. For further details on the development, validation and verification of the FSI coupling algorithm, see Degroote [38].

Numerical model initialization and solution

The IUV, DV and LPV bifurcation analyses are driven by volumetric flow rate and pressures, Q_0, $P_{0,\text{HeR}}$ and $P_{0\text{W,IVC}}$, as input (boundary conditions) to the lumped models.

According to Haugen et al. [70], the median volumetric flow rate entering the UV from the placenta is equal to $Q^1_{\text{UV}} = 205.2\,\text{ml/min}$ for a fetus of 36 weeks of gestation. The same study measured the flow rate trough the DV and LPV to be $Q^1_{\text{DV}} = 54.2\,\text{ml/min}$ and $Q^1_{\text{LPV}} = 42.5\,\text{ml/min}$ respectively. Hence, the left liver lobe receives $Q^1_{\text{HeL}} = 108.5\,\text{ml/min}$ ($Q_{\text{HeL}} = Q_{\text{UV}} - Q_{\text{DV}} - Q_{\text{LPV}}$) through minor veins along the IUV (Fig. 8.1). The minor veins along the IUV are not modelled in the current study (see Sec. 8.2.2). The flow rate input to the UV compartment is therefore given by the flow rate from the placenta that reaches the DV/LPV junction,

$$Q_{0,\,\text{UV}^*} = Q_{\text{UV}} - Q_{\text{HeL}} = 96.7\,\text{ml/min}. \tag{8.21}$$

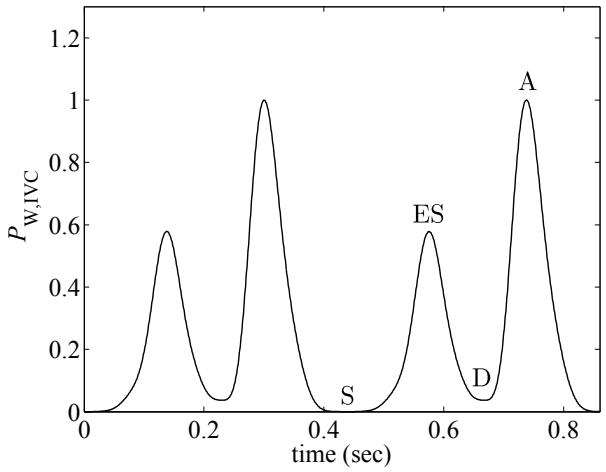

Figure 8.7 *IVC pressure waveform*: Two consecutive normalized pressure waveform in the IVC close to the fetal heart, with a cardiac cycle period of 0.43 sec, adopted from a study by Schröder et al. [167] on anesthetized sheep fetuses. The normalized pressure waveform, $P_{\text{W,IVC}}(t)$, is imposed in the lumped IVC compartment, as given in Eq. 8.22. The nadirs and peaks in each cardiac cycle represent the ventricular systole (S), end-systole (ES), ventricular diastole (D) and atrial contraction (A) [113]

The flow split recorded by Haugen et al. [70] between the flow rate immediately downstream of the DV/LPV junction ($Q_{0,\,\text{UV}^*}$) and the DV flow rate is therefore $Q_{\text{DV}}/Q_{0,\,\text{UV}^*} = 0.56$, while the flow split between the placenta blood rate and the DV flow rate is $Q_{\text{DV}}/Q_{\text{UV}} = 0.26$.

The reservoir pressure in the lumped HeR compartment is set to $P_{0,\text{HeR}} = 4.3\,\text{mmHg}$ [88, 152].

The normalized waveform $P_{\text{W,IVC}}(t)$, given in Fig. 8.7 represents the pulsatile part of pressure in the IVC at the inlet to the right atrium and is adopted from a study by Schröder et al. [167] on anaesthetized sheep fetuses. From the normalized pressure waveform $P_{\text{W,IVC}}(t)$, and a steady IVC pressure $P_{0,\text{IVC}}$ the pulsatile pressure in the lumped IVC compartment is given by

$$P_{\,0\text{W,IVC}}(t) = P_{0,\text{IVC}} + P_{\text{A,IVC}} P_{\text{W,IVC}}(t), \tag{8.22}$$

where $P_{\text{A,IVC}}$ represents the maximum pressure amplitude.

The IUV, DV and LPV bifurcation model analyses are divided into two steps:

- *Model initialization*

The model initialization phase involves initiating the analysis from an initial state of zero load on both the lumped models, 3D fluid and solid domain, to a loaded state at physiological volumetric flow rate and pressure. This is accomplished by ramping up boundary values that are constant during the model solution phase; the volumetric flow rate in the lumped UV compartment $Q_{0,\,\text{UV}^*} = 96.7$ ml/min (Eq. 8.21); the reservoir pressure in the lumped IVC compartment $P_{0,\text{IVC}} = 1.4\,\text{mmHg}$; the reservoir pressure in the lumped HeR compartment $P_{0,\text{HeR}} = 4.3\,\text{mmHg}$; the axial displacements $\Delta L_{\text{IUV}} = 1.6\,\text{mm}$, $\Delta L_{\text{DV}} = 1.6\,\text{mm}$ and

[1] Doppler velocimetry data from Haugen et al. [70]

$\Delta L_{\text{LPV}} = 0.6\,\text{mm}$ on Γ_i^S (where $i = \{\text{IUV,DV,LPV}\}$) (Figure 8.4). The model initialization phase ends when flow and pressures, in the lumped models and 3D fluid domain, are stabilized.

- Model solution

In the model solution phase, the pulsatile pressure waveform $P_{0\text{W,IVC}}(t)$, is introduced in the lumped reservoir compartment of the IVC, as given in Eq. 8.22, where the pressure amplitude is determined by $P_{\text{A,IVC}}$. Three consecutive heart cycles are simulated to obtain a periodical regime.

FSI simulations

Nine dynamic FSI simulations of the IUV, DV and LPV bifurcation are performed, where seven different geometries, (cases 2,4-9), and three different pressure amplitudes in the IVC (cases 1-3) are simulated. A time-step of $\Delta t = 5$ ms is adopted for all simulations.

CFD simulations

Three dynamic CFD simulations (with rigid walls) of the IUV, DV and LPV bifurcation are performed, on cases 1, 6 and 9 to investigate the effect of the compliance of the vein walls. The geometries in the CFD cases are extracted from the FSI results, so that the diameters D_{LPV}, $D_{\text{DV}_{\text{in}}}$, $D_{\text{DV}_{\text{out}}}$ and D_{IUV} in the CFD simulations corresponds to the time averaged diameters from the FSI simulations during a cardiac cycle.

8.3 Results

8.3.1 Flow distribution and velocities

The time averaged cross sectional mean velocities, $\overline{V}_{\text{mean}}$, are 42 ± 9 cm/sec at the DV inlet compared to 19 ± 4 cm/sec at the DV outlet (mean of cases 1-9). The time averaged max velocities, $\overline{V}_{\text{max}}$, are 60 ± 13 cm/sec at the DV inlet compared to 51 ± 3 cm/sec (mean of cases 1-9). Max velocities are higher at the DV inlet compared to the outlet for cases 1-5, 7 and 9. The opposite is found for cases 6 and 8, with higher max velocities at the DV outlet caused by the straight DV geometry.

The flow distribution in the IUV, DV and LPV bifurcation for test cases 1-9 is given in Table 8.4, expressed by the time averaged flow rate through the DV, $\overline{Q}_{\text{DV}}$, evaluated with Eq. 8.6 during one cardiac cycle. The inflow at the UV compartment is set to $Q_{0,\text{UV}^*} = 96.7$ ml/min as given in Sec. 8.2.2 for all test cases, and the flow rate through the DV is 52.3 ± 9.0 ml/min (mean of cases 1-9). This gives a flow rate split between the DV and IUV of $\overline{Q}_{\text{DV}}/\overline{Q}_{\text{IUV}} = 0.54$ (mean of cases 1-9). The lowest and highest DV shunting are found for cases 6 and 7, given by 0.31 and 0.61 respectively. Furthermore, the minimum and maximum flow rates through the DV are found for cases 6 and 7 respectively, caused by a narrow DV outlet for case 6 compared to case 7. A narrowing of the DV outlet increases the resistance to flow through the DV causing more of the volumetric flow to be directed through the LPV. The effect of the increased flow

Table 8.4 *Parametric study*: *Geometrical and lumped model input parameters*, α=branch angels and P_{A}=pressure amplitude; *Calculated model parameters*, $\overline{D}$=time averaged (Eq. 8.6) vessel diameters in the FSI simulations, D= vessel diameters in the CFD simulations, $\bar{h}$ = averaged velocity profile shape coefficients (VCs) evaluated with Eq. 8.5, $\overline{V}_{\max}$=time averaged (Eq. 8.6) max velocities, $\overline{V}_{\mathrm{mean}}$=time averaged (Eq. 8.6) cross sectional mean velocities, DPI=diameter pulsation index, PIV=index of venous pulsation, $\overline{Q}$=time averaged (Eq. 8.6) volumetric flow rate. **Note*: Mean of three cross-sections in the DV inlet region, see Fig. 8.2 and Sec. 8.2.2

		FSI										CFD		
CASE		1	2	3	4	5	6	7	8	9	(mean,std)	1	6	9
$\alpha_{0\ \mathrm{DV}}$	(deg)	0	0	0	50	70	0	0	0	0		0	0	0
$\alpha_{0\ \mathrm{IUV}}$	(deg)	0	0	0	28	35	0	0	0	0		0	0	0
$P_{\mathrm{A,IVC}}$	(mmHg)	1.5	3.0	4.5	3.0	3.0	3.0	3.0	3.0	3.0		1.5	3.0	3.0
$\overline{D}_{\mathrm{LPV}}$	(mm)	3.5	3.5	3.5	3.5	3.5	3.5	3.5	3.5	3.5				
$^*\overline{D}_{\mathrm{DV_{in}}}$	(mm)	1.6	1.6	1.6	1.6	1.6	1.6	1.6	2.1	1.6				
$\overline{D}_{\mathrm{DV_{out}}}$	(mm)	2.6	2.6	2.6	2.6	2.6	1.6	3.2	2.1	2.6				
$\overline{D}_{\mathrm{IUV}}$	(mm)	6.1	6.1	6.1	6.1	6.1	6.1	6.1	6.1	4.1				
D_{LPV}	(mm)											3.5	3.5	3.5
$^*D_{\mathrm{DV_{in}}}$	(mm)											1.6	1.6	1.6
$D_{\mathrm{DV_{out}}}$	(mm)											2.6	1.6	2.6
D_{IUV}	(mm)											6.1	6.1	4.1
$\overline{Q}_{\mathrm{DV}}/\overline{Q}_{\mathrm{IUV}}$		0.60	0.56	0.51	0.57	0.60	0.31	0.61	0.54	0.57	(0.54, 0.09)	0.54	0.32	0.61
$\bar{h}_{\mathrm{LPV}}$		0.62	0.63	0.64	0.63	0.63	0.69	0.62	0.63	0.51	(0.62, 0.05)	0.64	0.69	0.51
$^*\bar{h}_{\mathrm{DV_{in}}}$		0.70	0.69	0.68	0.70	0.72	0.64	0.70	0.68	0.67	(0.69, 0.02)	0.70	0.64	0.68
$\bar{h}_{\mathrm{DV_{out}}}$		0.33	0.34	0.34	0.34	0.35	0.49	0.24	0.51	0.33	(0.36, 0.08)	0.34	0.49	0.34
$\bar{h}_{\mathrm{IUV}}$		0.51	0.51	0.51	0.51	0.51	0.51	0.51	0.51	0.51	(0.51, 0.00)	0.51	0.51	0.51
$^*\overline{V}_{\mathrm{max,DV_{in}}}$	(cm/sec)	70	65	60	65	63	39	72	39	69	(60, 13)	66	41	70
$\overline{V}_{\mathrm{max,DV_{out}}}$	(cm/sec)	56	51	46	51	51	49	52	52	52	(51, 3)	54	51	52
$^*\overline{V}_{\mathrm{mean,DV_{in}}}$	(cm/sec)	49	45	41	46	45	25	51	27	47	(42, 9)	46	26	47
$\overline{V}_{\mathrm{mean,DV_{out}}}$	(cm/sec)	19	17	16	17	18	25	12	27	17	(19, 4)	18	25	17
$^*\mathrm{PIV_{DV_{in}}}$		0.21	0.52	0.98	0.52	0.54	0.50	0.51	0.54	0.48	(0.53, 0.20)	0.24	0.54	0.53
$\mathrm{PIV_{DV_{out}}}$		0.26	0.61	1.03	0.61	0.61	0.59	0.62	0.59	0.57	(0.61, 0.19)	0.32	0.61	0.66
$^*\mathrm{DPI_{DV_{in}}}$		0.04	0.07	0.09	0.07	0.07	0.01	0.09	0.02	0.07	(0.06, 0.03)			
$\mathrm{DPI_{DV_{out}}}$		0.04	0.07	0.09	0.07	0.07	0.06	0.07	0.07	0.07	(0.07, 0.01)			

resistance for case 6 compared to case 7 is also seen in Fig. 8.8, as a decrease in the maximum cross sectional velocity at the DV isthmus, $V_{\mathrm{max,DV_{isth}}}$.

8.3.2 Axial stretch

Axial displacements $\Delta L_{\mathrm{LPV}} = 1.6\,\mathrm{mm}$, $\Delta L_{\mathrm{DV}} = 1.6\,\mathrm{mm}$ and $\Delta L_{\mathrm{IUV}} = 0.6\,\mathrm{mm}$, of the $\Gamma^{\mathrm{S}}_{\mathrm{LPV}}$, $\Gamma^{\mathrm{S}}_{\mathrm{DV}}$ and $\Gamma^{\mathrm{S}}_{\mathrm{IUV}}$ vein boundaries (Sec. 8.2.2) are applied to all simulations in the model initiation

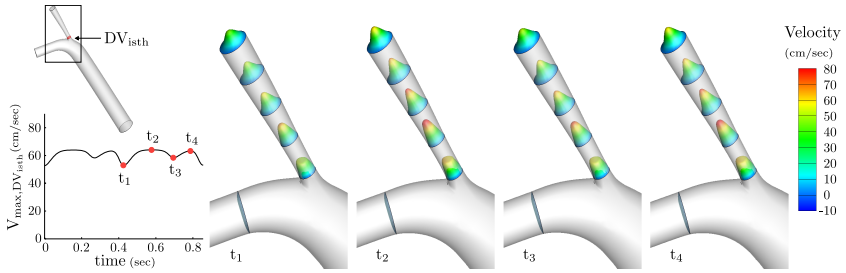

(a) case 1

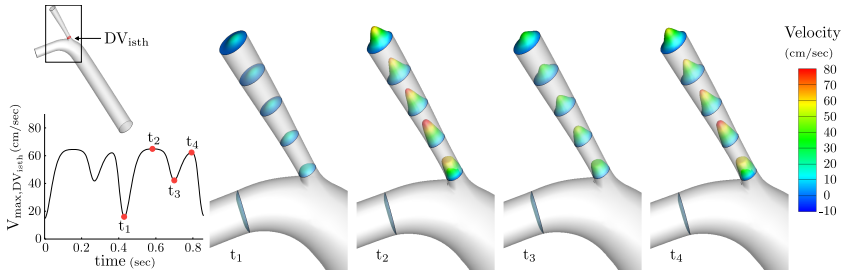

(b) case 3

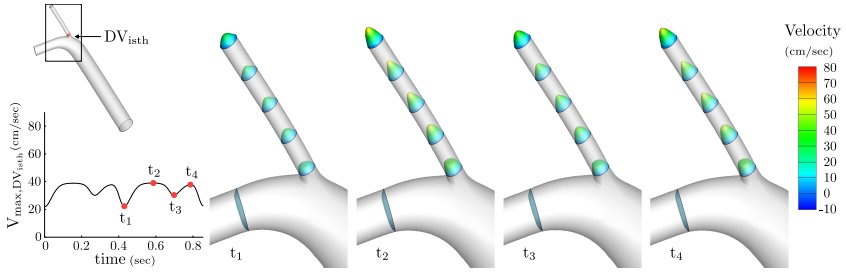

(c) case 6

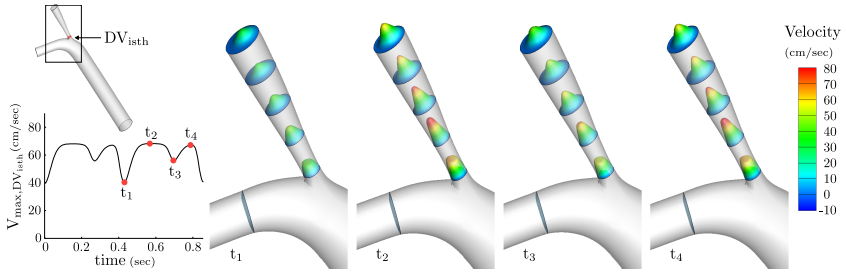

(d) case 7

Figure 8.8 *Velocity profiles projections*: Velocity profiles at different time points during the cardiac cycle. The velocity profiles are represented as cross-section normal projections of the velocity magnitude at different cross-sections in the DV and LPV. Four time points during the cardiac cycle are illustrated; t_1, atrial contraction; t_2, ventricular systole; t_3, end systole; t_4,ventricular diastole, given by the maximum cross sectional velocity at the DV isthmus, $V_{\text{max,DV}_{\text{isth}}}$

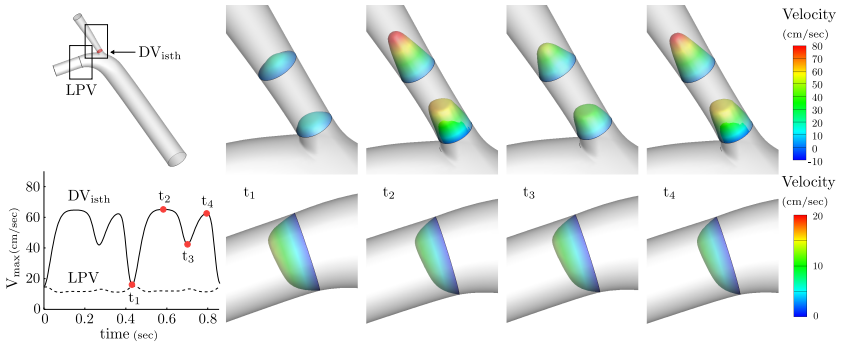

(a) case 3

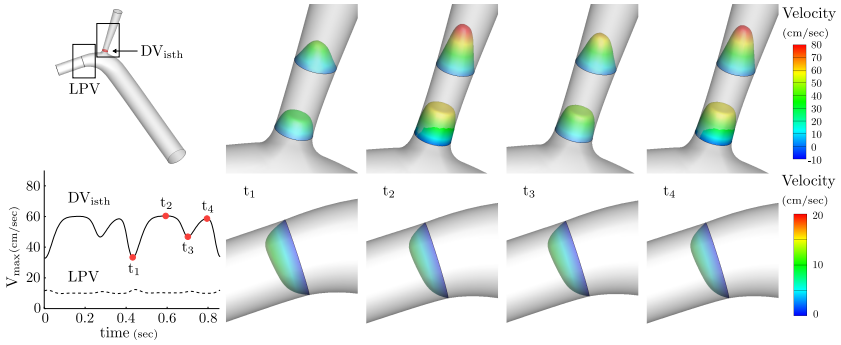

(b) case 5

Figure 8.9 *Velocity profiles projections*: Velocity profiles at the DV and LPV for case 1 and 5. *Case 1*: The velocity profile at the DV isthmus is blunt and skewed towards the LPV. The velocity profile $1/4$ DV length from the DV isthmus is close to parabolic. The velocity profile at the LPV is skewed towards the DV. The maximum flow velocity and the pulsatility in the DV is significantly higher than in the LPV. The maximum flow velocity at the LPV occurs during atrial contraction t_1, when the velocity in the DV is at its minimum. *Case 5*: The velocity profile at the DV isthmus for case 5 is blunt and close to symmetric compared to case 1. *Note*: The velocity profile projection at the LPV position, is scaled with a factor of 4 compared to the DV.

phase (Sec. 8.2.2). For the reference case 2, the displacements resulted in axial stretches of $L_{0,\text{LPV}}/L_{\text{LPV}} = 1.03$, $L_{0,\text{DV}}/L_{\text{DV}} = 1.11$ and $L_{0,\text{IUV}}/L_{\text{IUV}} = 1.04$, at the end of the model initiation phase. The magnitudes of axial displacement are determined from initial static tests on the solid model for reference case 2, so that after pressurization of the LPV, DV and IUV bifurcation, the position of the insertion point of the DV onto the LPV/IUV (i.e. at the $D_{\text{DV}_{\text{isth}}}$) is approximately the same as in initial geometry.

8.3.3 Velocity profiles

Velocity profiles at a range of cross-sections normal to the DV axial direction, are illustrated in Fig. 8.8 for specific instances in time. The velocity profiles represent the cross-section normal

projection of velocity magnitude.

Four time points during the cardiac cycle are given t_1, t_2, t_3 and t_4, derived from the maximum velocity at the DV isthmus cross-section $V_{\max,\mathrm{DV_{isth}}}$. The four time points are; (t_1) the nadir during atrial contraction; (t_2) the peak during ventricular systole; (t_3) the nadir during end systole; (t_4) the peak during ventricular diastole. The blunt velocity profiles at the DV isthmus (Fig. 8.8 and 8.9), are caused by the entrance effect of flow entering a narrow tube from a larger reservoir. The narrow DV opening compared to the large diameter of the IUV, accelerates the fluid into an undeveloped blunt velocity profile at the DV isthmus (Fig. 8.9). The DV velocity profile at $1/4$ DV length from the DV isthmus is more parabolic, with a VC of 0.547 ± 0.022 (mean of cases 1-9). The blunt velocity profiles at the DV isthmus is skewed towards the LVP for all tested cases. This trend is least apparent for case 5, where the velocity profile at the DV inlet is almost symmetric (Fig. 8.9). Case 5 has the steepest branch angle, $\alpha_{\mathrm{DV}} = 70\,\mathrm{deg}$, between the DV and IUV of all the tested cases.

The averaged VCs $\bar{h}$ are calculated for the LPV, DV inlet, DV outlet and IUV as defined in Eq. 8.5. The values of the velocity shape coefficient are 0.687 ± 0.023 and 0.363 ± 0.084 at the DV inlet and outlet position respectively (mean of cases 1-9). The VC at the IUV position (at D_{IUV}, Fig. 8.2) is equal to 0.509 ± 0.001 (mean of cases 1-9), i.e. close to parabolic, while the VC at the LPV position (at D_{LPV}, Fig. 8.2) is partially blunt and equal to 0.624 ± 0.048 (mean of cases 1-9). The VC for case 9 in the LPV position is close to parabolic, equal to 0.512. Case 9 stands out from the remaining cases, with a minor diameter change from the IUV to the LPV (see Table 8.4). Furthermore, while the VC in the LPV position is partially blunt (0.624 ± 0.048 for cases 1-9), the VC at the LPV outlet (at Γ_{LPV}, Fig. 8.2) is close to parabolic and equal to 0.524 ± 0.009 (for cases 1-9, not given in Table 8.4).

8.3.4 Dynamic effects

The maximum flow velocities and the pulsatility in the DV are significantly higher than in the LPV and IUV. The maximum flow velocity in the LPV occur during atrial contraction when the velocity in the DV and IUV is at its minimum (t_1 in Fig. 8.9).

The IVC pulsations generates flow pulsations at the DV inlet which can be quantified by the PIV index (Eq. 8.8) equal to 0.21, 0.52 and 0.98 for cases 1 to 3, as given in Table 8.4. Furthermore, increasing DV pulsation index causes a minor decrease in the time averaged value of the VC at the DV inlet, equal to 0.70,0,69 and 0.68 for cases 1 to 3.

The change in diameter at the DV inlet and outlet is quantified by the diameter pulsation index DPI (Eq. 8.9), and given in Table 8.4. The diameter pulsations are smaller at the DV inlet with mean DPI value of 0.06 ± 0.03, compared to 0.07 ± 0.01 at the DV outlet (mean of cases 1-9).

Maximum and minimum quantities during the cardiac cycle used to derive the PIV (Eq. 8.8) and the DPI (Eq. 8.9) indexes are determined after spline interpolation in the time history data for increased accuracy.

Table 8.5 *FSI grid sensitivity*: Grid sensitivity test of the VC h at the LPV, DV inlet and outlet and at the IUV. Four grid sets were tested with increasing number (#) of fluid grid volumes and quadratic elements. Satisfactory grid independence is found for grid 3, with minor changes for VCs when moving to the finer grid 4. **Note*: Solid grid 4 included two layers of quadratic elements through the wall thickness

grid	fluid-grid (#)	solid-grid (#)	$\overline{h}_{\mathrm{LPV}}$	$\overline{h}_{\mathrm{DV_{in}}}$	$\overline{h}_{\mathrm{DV_{out}}}$	$\overline{h}_{\mathrm{IUV}}$
1	4 392	208	0.663	0.743	0.375	0.537
2	28 304	564	0.644	0.701	0.357	0.525
3	139 278	1 660	0.631	0.690	0.337	0.509
4	320 536	6 664*	0.632	0.688	0.338	0.507

8.3.5 Grid sensitivity for VC

A grid sensitivity test, seen in Table 8.5, has been performed on the reference geometry (case 2), where the grid sensitivity of the VC at the LPV, DV inlet and outlet and at the IUV is investigated. Four grid sets are tested with increasing number of fluid grid volumes and quadratic elements for the solid. Satisfactory grid independence for the VCs is found for grid 3, with minor changes for VCs when moving to the finer grid 4, as seen in Table 8.5. Hence, grid refinement level 3 is used for all test cases in the parametric study, i.e. cases 1 to 9. The finest solid grid (grid 4) includes two layers of quadratic elements through the wall thickness of the LPV, DV and IUV veins.

8.3.6 CFD simulations

Results from the CFD analyses for cases 1, 6 and 9 are given in Table 8.4. A flow shift towards the LPV is observed for CFD case 1 compared to FSI case 1, with a $\overline{Q}_{\mathrm{DV}}/\overline{Q}_{\mathrm{IUV}}$ ratio of 0.54 and 0.60 respectively. The opposite is seen for CFD cases 6 and 9 with a flow shift towards the DV compared the FSI simulations. The main difference in the VCs between the CFD and FSI cases is seen for case 1 in the LPV position, with a VC of 0.64 (CFD) compared to 0.62 (FSI). For the other cases and positions only minor changes are observed between CDF and FSI. However, the recorded PIV index are higher for all CFD cases compared to the FSI cases.

8.4 Discussion

Doppler ultrasound combined with detailed knowledge about the local hemodynamics is used in several studies for non-invasive measurements of volumetric flow rate in the fetal venous return [16, 70, 115, 151]. Several potential pitfalls exist when evaluating the volumetric flow rate in blood vessels with ultrasound, which is especially true for the human DV. One important source of error is the small DV diameter, found to be between 0.5 and 2.0 mm in the second half of the pregnancy [115]. Furthermore, since it is difficult to obtain reliable direct measurements

of the spatial mean velocity [115], it is preferred to trace the maximum velocity evaluated in combination with a VC to estimate the mean velocity. The complex hemodynamics of the DV [151], means that simple assumptions for the VC at the DV inlet, i.e. flat profile $h = 1.0$, results in wrong evaluation of the volumetric flow rate, as shown by Pennati et al. [151].

A numerical model has been developed in this work, to evaluate the VC in the human DV, which can supplement existing studies on the DV VC in the literature [111, 151]. The DV, LPV and IUV bifurcation is modeled with 3D FSI, and the major neighbouring vessels are included in lumped models, more specifically the amniotic part of the UV, the HeR and the IVC. The VC makes it possible to estimate the mean volumetric flow rate through the DV during the cardiac cycle, from the maximum velocity trace given by Doppler ultrasound.

The VC predicted by the numerical model in the DV inlet region is found to be 0.687 ± 0.023 (mean and standard deviation for the 9 parametric FSI cases, Table 8.5). Pennati et al. [151] reported a velocity coefficient at the DV inlet of 0.677 ± 0.040 in a numerical steady state CFD study of the IUV, DV and LPV bifurcation with rigid walls. Kiserud et al. [111] reported a VC of 0.68 ± 0.07 in a high frequency Doppler velocimetry *in-vivo* study on fetal sheep fetuses. In the study of Kiserud et al. [111], the spatial mean velocity and maximum velocity in a sample volume at the DV inlet was determined from the Doppler velocity spectrum during anaesthesia and laparotomy, so that the ultrasound probe could be applied directly at the uterine wall. Hence, our findings for the VCs at the DV inlet region, although slightly higher, are in agreement with the findings Pennati et al. [151] and Kiserud et al. [111].

The flow split between the DV and the IUV ($\overline{Q}_{\mathrm{DV}}/\overline{Q}_{\mathrm{IUV}}$) given by the FSI simulations are found to be 0.54 ± 0.09 (mean and standard deviation for the 9 parametric FSI cases, Table 8.5). The reference case 2, gave a flow split of 0.56 which is the same as reported for normal fetuses at 36 weeks of gestation by Haugen et al. [70] in a Doppler study. The flow split between the placenta and the DV flow rate is changing throughout the gestational period [115], and a significant flow shift towards the DV is documented in several studies on pathological situations such as IUGR [17, 112, 179]. Shunt fractions above 100% is also reported [17, 112], suggesting a reversed flow direction in the LPV compared to the normal case [99, 101]. Abnormal and changing flow split in the IUV, DV and LPV bifurcation during gestation will most probably affect the VC at the DV inlet (and at other locations in the bifurcation), however such cases are not included in the current study. Especially the case of reversed flow direction in the LPV will influence the DV inflow pattern from the normal case, where the blood flow rate from the IUV is divided between the DV and LPV (see Fig. 8.1). Moreover, the minor vessels along the IUV are not included in the current study. Anatomical investigations from Mavrides et al. [133, 134] on human fetuses suggest that some of the minor IUV vessels are positioned close to the DV inlet. Hence, the minor IUV vessels may influence the flow field in and around the IUV, DV and LPV bifurcation and therefore influence the VCs in the same region. The minor IUV vessels are excluded in the current numerical study to simplify the modelling approach. Moreover, the location and the individual size of these vessels are not well described in the literature. Anatomical mapping and numerical modelling of these vessels to determined their influence on the local hemodynamics in the IUV and in the IUV, DV and LPV bifurcation is therefore an interesting prospect for future studies.

The local hemodynamics is an important determinant for the shape of the velocity profile at

the DV inlet. Pennati et al. [151] found a regurgitation zone (standing flow vortex) extending from the DV inlet and well into the DV at the LPV side of the DV, for the majority of the test cases in their study. Kiserud et al. [115] reported in their Doppler velocimetry study on sheep fetuses, that they could not confidently trace a negative velocity component (flow regurgitation) in the DV. In the current study, none of the nine parametric cases shows flow regurgitation at the DV inlet. However some regurgitation is found at the DV outlet for case 7, where the conicity is high, i.e. $\overline{D}_{\text{DV,out}}/\overline{D}_{\text{DV,in}} = 1.9$. The regurgitation zone at the DV inlet, reported by Pennati et al. [151], might be caused by a sharp notch radius at the DV isthmus. In the current study, the transition between the DV and the IUV is more gradual (based on the findings of Mavrides et al. [134] and Mavrides et al. [133], i.e. larger notch radius (Fig. 8.2). A regurgitation zone at the DV inlet will influence the VC, i.e. the spatial mean velocity would be the same if the regurgitation zone is there or not (for equal volumetric flow rate). However, the spatial maximum velocity will increase if a regurgitation zone is present and cause a decrease in the VC (Eq. 8.16), which can explain why the VC found by Pennati et al. [151] is somewhat lower than in the current study. Pennati et al. [151] also found that the velocity profile at the DV inlet was skewed towards the IUV, whereas in the current study it is found that the velocity profile at the DV inlet is skewed towards the LPV for all test cases. This disagreement may also be attributed to the local notch geometry at the DV isthmus.

The mean VC in the LPV position (Fig. 8.2) in the current study for cases 1 to 9, is found to be partially blunt (0.624 ± 0.048), and approached a parabolic value (0.524 ± 0.009) at the LPV outlet (Γ_{LPV}, Fig. 8.2). The VC in the LPV is important for calculating the correct flow distribution in the DV, LPV and IUV bifurcation. However, the VC decreases when the conicity between the IUV and LPV decreases, as seen for case 9 with a VC of 0.512 and conicity $D_{\text{IUV}}/D_{\text{LPV}} = 1.2$, compared to $D_{\text{IUV}}/D_{\text{LPV}} = 1.8$, for cases 1 to 8. Several studies in the literature on the flow distribution in the DV, LPV and IUV bifurcation have used a VC of 0.5 in the LPV [17, 70, 98], which could lead to an underestimation of LPV volumetric flow rates, depending on the measurement site in the LPV and on the local geometry.

An increase in the PIV index causes the time averaged VCs to decrease, as seen for cases 1 to 3 (Table 8.4), with PIV index 0.21, 0.52 and 0.98 compared to a time averaged VCs of 0.70, 0.69 and 0.68 respectively. However, the decrease in the time averaged VC with increasing PIV index is considered to be minor. Our findings are therefore in agreement with Kiserud et al. [111], in their Doppler velocimetry study on fetal sheep fetuses, where they were unable to demonstrate any influence of the PIV index on the VCs.

The diameter pulsations are quantified by the diameter pulsation index DPI (Eq. 8.9), at the DV inlet and outlet (Table 8.4). The diameter pulsations are highest at the DV outlet with a mean value for cases 1 to 9 of 0.07 ± 0.01, compared to 0.06 ± 0.03 at the inlet. The magnitude of the diameter pulsations in the current numerical study at the DV inlet is comparable to the diameter pulsations observed by Acharya and Kiserud [1] in a Doppler velocimetry study on human fetuses, who reported a mean DPI of 0.21 and a median DPI of 0.05, at the DV inlet for 20 fetuses (gestational age 19-40 weeks). However, Acharya and Kiserud [1] reported mean DPI of 0.40 and median DPI of 0.65 at the DV outlet, which is significantly higher than in the current numerical study.

CFD simulations of cases 1, 6 and 9 (Table 8.4) are included in the current study with same

boundary conditions as in the respective FSI cases, to investigate the effect of the compliance of the vein walls. A flow shift towards the LPV is observed for CFD case 1 and towards the DV for cases 6 and 9, compared to the FSI simulations as seen in Table 8.4. The resistance to flow during the cardiac cycle is constant with respect to the vessel cross-sectional areas in the CFD simulations, compared to the FSI simulations where the vessel areas change during the cardiac cycle due to changes in the transmural pressure. Additionally, the rigid walls in the CFD simulations caused the PIV index magnitude to increase compared to the FSI PIV index, as seen in Table 8.4. Only minor changes in the predicted VCs are observed between the CFD and FSI simulations. The main difference is seen for case 1 in the LPV position, with a CFD VC of 0.64 for the compared to a FSI VC of 0.62. However, further investigations are needed to determined if FSI predicts different VCs compared to CFD in the case of higher DPI index (i.e. larger deformations caused by softer vein walls/high pressure variations). For example, Acharya and Kiserud [1] reported DPI indexes of 0.21 and 0.40 at the DV inlet and outlet respectively, in an ultrasound study on human fetuses, which is notably higher seen in the current FSI simulations (Table 8.4). Additionally, the current numerical study did not include abnormal/diseased conditions such as reversed flow in the LPV and flow reversal in the DV during atrial contraction, which may induce greater differences between CFD and FSI in terms of VCs.

In conclusion, the numerical model of the DV, LPV and IUV bifurcation developed in this work using pulsatile flow and distensible vessel walls, confirms previous studies based on steady flow and rigid walls [151], regarding the VC at the DV inlet. The VC at the DV inlet is found to be 0.687 ± 0.023, which is in agreement with the numerical findings by Pennati et al. [151] and Doppler velocimetry measurements by Kiserud et al. [111]. Compared to numerical models of the DV, LPV and IUV bifurcation in the literature [77, 151], the current model takes into account the interaction between the veins and blood flow (FSI) and includes lumped boundary models. Additionally, CFD simulations with rigid walls performed in the current study, produced only minor differences in the predicted VCs compared to the FSI simulations. Hence, our results indicate that wall compliance does not significantly alter the VCs predictions in the LPV, DV and IUV bifurcation, and that rigid wall CFD simulations as performed by Pennati et al. [151], may be sufficient for predicting VCs for clinical flow assessments in the DV. However, further model development and investigations on the impact of model input parameters are needed, to increase the confidence of velocity profile predictions for Doppler ultrasound studies of the human DV over a wider physiological and pathological range.

Appendix

The following outlines the time discretization of the lumped 0D models presented in Sec. 8.2.2, and the lumped model to 3D fluid coupling as presented in Sec. 8.2.2.

The 3WK and Z_cC lumped models are discretized in time with a first order implicit scheme, and solved for the pressure update P^{n+1}. The lumped model pressures P_i^{n+1} are updated and imposed as pressure boundary conditions on the fluid domain boundaries, Γ_i ($i = \{\text{IUV,DV,LPV}\}$, Fig. 8.2), each flow iteration in the fluid solver.

In the following, the variables denoted with a star, i.e. P^* and Q^* are updated each flow iteration in the fluid solver. Whereas, the vessel cross sectional area denoted with a double star A^{**} is updated each FSI iteration. The A^{**}, Q^* and P^* variables are calculated from the end surface of the fluid domain boundaries, Γ_i, connected to the lumped model, as given in Eq. 8.18.

- *3WK model*

The 3WK model given in Eq. 8.14:

$$\frac{dP}{dt} + \frac{(P - P_0)}{R_C C} = Z_c \frac{dQ}{dt} + Q \frac{dZ_c}{dt} + Q \left(\frac{1}{C} + \frac{Z_c}{R_C C} \right),$$

discretized with Backward Euler, gives

$$\begin{aligned} P^{n+1} &= \left(P^n + \widehat{P} + P_0 \frac{\Delta t}{\tau} \right) / \left(1 + \frac{\Delta t}{\tau} \right) \\ \tau &= R_C C \end{aligned} \tag{8.23}$$

where $\widehat{P}$ is given by,

$$\widehat{P} = Z_c^* \left(Q^* - Q^n \right) + Q^* \left(Z_c^* - Z_c^n \right) + Q^* \left(\frac{1}{C} + \frac{Z_c^*}{\tau} \right) \Delta t,$$

- *UV compartment*

The UV compartment given in Eq. 8.15:

$$\frac{dP}{dt} = -Z_c \frac{dQ}{dt} - Q \frac{dZ_c}{dt} + \frac{(Q_0 - Q)}{C},$$

discretized with Backward Euler, gives

$$P^{n+1} = P^n + \widehat{P} \tag{8.24}$$

where $\widehat{P}$ is given by

$$\widehat{P} = -Z_c^* \left(Q^* - Q^n \right) - Q^* \left(Z_c^* - Z_c^n \right) + \frac{(Q_0 - Q^*)}{C} \Delta t.$$

- *Characteristic impedance Z_c*

The characteristic impedance Z_c^* of the 3WK and UV compartment are evaluated as:

$$Z_c^* = \frac{\rho_f}{A^{**}} c(P^*). \tag{8.25}$$

where $c(P^*)$ is the pulse wave velocity (see Sec. 8.2.2) and A^{**} is the cross sectional area of the terminating vessel connected to the lumped models.

Chapter 9

A one-dimensional vascular network model, for applications in the feto-placental circulation

9.1 Introduction

The fetal vascular system is from an early gestational age (8-10 gestational week) well developed and consists of a network of veins and arteries, within the fetal body and in the umbilical circulation [103, 104, 171]. The feto-placental circulatory system (and adult circulation), may from a simplified mechanical point of view, be considered a network of slender compliant vessels. One-dimensional (1D) network models for blood flow in compliant vessels [50, 161, 169, 177], are therefore an appealing choice for studying small or large parts of the systemic fetal and adult circulation. The complex local hemodynamics in blood vessels cannot be captured by 1D models, however they are computationally efficient and can give valuable information on the distribution and propagation of flow, pressure and shear waves from a systemic point of view [183].

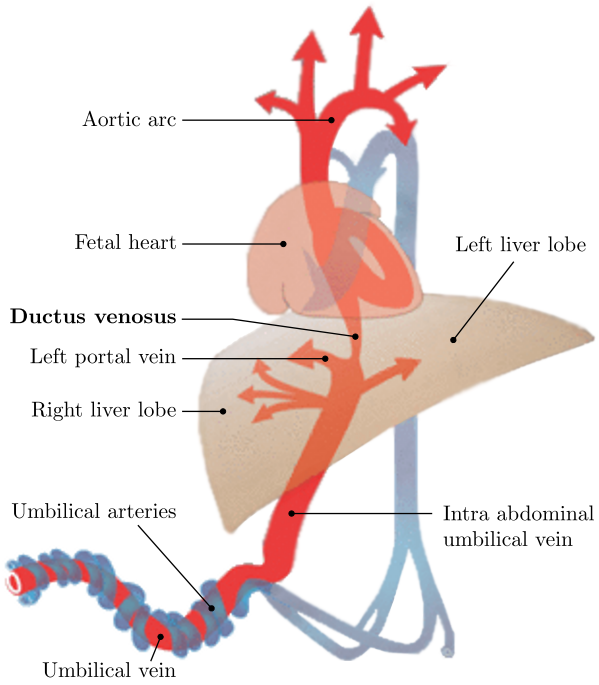

Figure 9.1 Illustration of major vessels in the feto-placental circulation. Modified from Haugen et al. [69]

A considerable amount of research papers can be found in the literature on 1D models for blood flow, with different levels of model complexity, for an overview see e.g. Reymond et al. [161]. A number of research articles on 1D modeling in fetal flows are also present in the literature, Sherwin et al. [169] investigated wave propagation in the umbilical arteries, Alastruey et al. [4] modeled clamping of the umbilical vein, Franke et al. [55] modeled flow in the arterial network of monochorionic placentas, Smolich et al. [173, 174] performed wave intensity analysis in the pulmonary trunk and ductus arteriosus and Hellevik et al. [79] assessed ductus venosus tapering and wave transmission from the fetal heart.

The feto-placental circulation has gained considerable clinical interest after the introduction of non-invasive examination techniques such as Doppler ultrasound [67, 105]. One important area within the feto-placental circulation is the venous return of oxygen and nutrient rich blood from the placenta to the fetal liver and heart [104] (Fig. 9.1). Observations of hemodynamical phenomena in the venous placenta return have generated numerous scientific studies and clinical interest [131]. Abnormal velocity waveforms in the ductus venosus can signal chromosomal abnormalities [27, 30, 126, 130], and umbilical venous pulsations have been associated with pathologies such as imminent asphyxia and congestive heart disease [68, 124]. Another important hemodynamics determinant is the umbilicocaval (portocaval) pressure gradient between the umbilical vein and inferior vena cava. Increased pressure gradient might be caused by liver disease and anemia, which increases flow resistance in the liver [116], and leads to

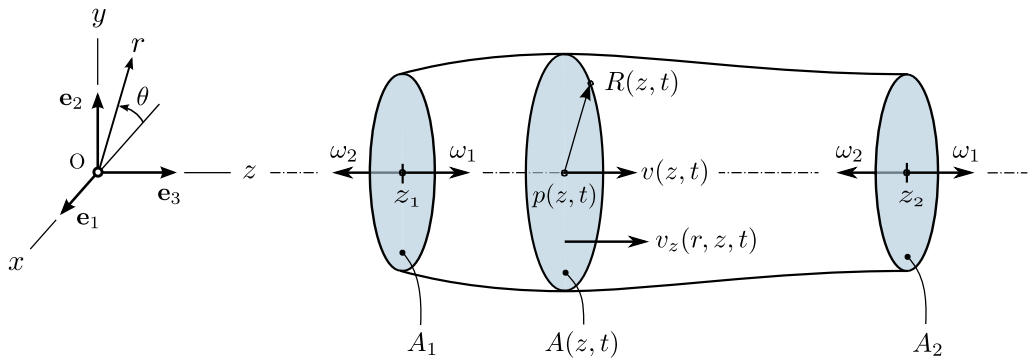

Figure 9.2 Illustration of compliant fluid filled vessel with major axis along the z-axis. Given by the vessel radius $R = R(z,t)$ and cross-section area $A = A(z,t)$. The axial fluid velocity $v_z = v_z(r,z,t)$ is a function of the radial position r in the cross-section A. The cross-sectional averaged fluid velocity and pressure are given by given by $v = v(z,t)$ and $p = p(z,t)$ respectively. The $A_1 = A_1(t)$ and $A_2 = A_2(t)$ boundaries defines the in/out-flow faces of the vessel fixed at the axial positions z_1 and z_2. The Riemann variables ω_1 and ω_2 in the positive and negative z-direction respectively, are illustrated as they leave and enters the flow domain at the two boundary surfaces A_1 and A_2.

increased flow velocities in the ductus venosus [110]. The portocaval pressure gradient is also one of the determinants for the central venous pressure, which by many clinicians is regarded a key factor for understanding central blood circulation and hemodynamics changes in pathology [104]. Other clinically important aspects of the feto-placental circulation may include flow reversal in the ductus venosus [113], and the flow distribution between the ductus venosus and the two liver lobes [94–96].

In this study, we present a 1D vascular network model aimed at applications in the feto-placental circulation, and other vascular networks such as the adult arterial tree. The network model is derived from the governing equations for 1D flow in compliant vessels [75, 87, 183], and discretized with the explicit MacCormack scheme [5, 125]. Furthermore, the system characteristics (the Riemann variables [169]) are determined and formulated in a linearized form [158], and used to impose boundary conditions and network connections.

9.2 Methods

9.2.1 Governing equations

Conservation of mass and momentum for fluid flow in a 1D compliant vessel with a circular cross-section and major axis defined along the z-axis (Fig. 9.2) [24, 161, 183], may be presented as

$$\frac{\partial A}{\partial t} + \frac{\partial Av}{\partial z} = 0 \tag{9.1}$$

$$\frac{\partial Av}{\partial t} + \frac{\partial}{\partial z}\left(2\pi\int_0^R r\, v_z^2\, dr\right) + \frac{A}{\rho}\frac{\partial p}{\partial z} = \frac{2\pi R}{\rho}\mu\left[\frac{\partial v_z}{\partial r}\right]_{r=R} \tag{9.2}$$

where $A = A(z,t)$ is cross-section lumen area, $R = R(z,t) = \sqrt{A/\pi}$ is the lumen radius, and $p = p(z,t)$ and $v = v(z,t)$ are the cross-section averaged fluid pressure and velocity, respectively. The fluid density and kinematic viscosity is given by ρ and μ, and the axial velocity $v_z = v_z(r,z,t)$ is a function of the radial position r in the cross-section A (Fig. 9.2) [24, 183]. In the 1D momentum balance (Eq. 9.2), both the convective acceleration (second left hand side) and viscous (second right hand side) terms are functions of the axial velocity v_z, which may be determined by an approximated velocity profile in the cross-section A. The 1D system given by Eq. 9.1 and 9.2, is generally represented by the three state variables (p, v, A). However, the system can be represented by two independent variables, e.g. (A, v), (A, q), (p, v) and (p, q) where $q = Av$ is the flow rate through the cross-section A [169], if an instantaneous constitutive relation is established between the pressure p and cross-section area A.

9.2.2 Velocity profiles

The distribution of the axial velocity v_z in the cross-section A, i.e. the velocity profile, needs to be evaluated to approximate the convective acceleration and the viscous forces in 1D momentum balance (Eq. 9.2). Several approaches for velocity profile approximation for 1D flow have been explored in the literature, e.g. assumed shape profiles (power-law and assumed stokes layer), time-periodic profiles (Womersley velocity profiles) and approximated time-periodic profiles [183]. In this work, an axisymmetrical assumed shape profile is employed, such that the axial velocity v_z can be redefined according to

$$v_z(r,z,t) = \phi(r)\, v(z,t), \tag{9.3}$$

where $\phi(r)$ defines the profile shape in the cross-section A. A power law approximation can be made with the shape function

$$\phi(r) = \frac{\gamma+2}{\gamma}\left[1 - \left(\frac{r}{R}\right)^{\gamma}\right], \tag{9.4}$$

where γ determines the bluntness of the velocity profile, for example $\gamma = 2$ yields Poiseuille flow [87]. The non-slip condition at the vessel wall surface is satisfied with $\phi(R) = 0$, along with the condition $2\pi \int_R r\phi\, dr = A$. Substitution of Eq. 9.3 and the power-law profile Eq. 9.4 into the second left hand and right hand term in the momentum balance Eq. 9.2, gives

$$\frac{\partial}{\partial z}\left(2\pi \int_0^R r\, v_z^2\, dr\right) = \delta \frac{\partial}{\partial z}(Av^2) \tag{9.5}$$

$$\frac{2\pi R}{\rho}\mu\left[\frac{\partial v_z}{\partial r}\right]_{r=R} = -2\pi(\gamma+2)\frac{\mu}{\rho}v \tag{9.6}$$

where $\delta = \frac{(\gamma+2)}{(\gamma+1)}$ is a shape constant.

9.2.3 Vessel compliance

The governing equations for conservation of mass and momentum given in Eq. 9.1 and 9.2 contains three state variables (p, v, A). A constitutive relation between the cross-sectional area A and pressure p is therefore needed to close the system. A simplified instantaneous relationship between the vessel transmural pressure and cross-sectional area might be presented as

$$p = \widetilde{p}(A; z, t) \tag{9.7}$$

from which the vessel compliance

$$C = \frac{\partial A}{\partial p}, \tag{9.8}$$

can be determined. The vessel compliance is generally non-linearly dependent on the pressure and the location in the vascular three [161]. The spacial dependency of the compliance might be caused by local variations in material properties and support from surrounding tissue. The non-linear pressure dependence is to a large extent caused by the progressive recruitment of collagen fibers at increasing strain [83]. Additionally, intrinsic factors like smooth muscle cell activation may significantly influence the local compliance of a vessel [56]. Viscoelastic behavior is another important determinant for the structural response of cardiovascular vessels, and several authors have included viscoelasticity of the vessel wall in 1D models for blood flow, see e.g. Bessems et al. [23], DeVault et al. [41], Reymond et al. [161].

A simplified purely elastic pressure-area relationship may be derived from Laplace‘s law, giving

$$p = p_{\text{ext}} + \beta(\sqrt{A} - \sqrt{A_0}) \tag{9.9}$$

where p_{ext} is a constant external pressure and A_0 is the reference cross-section vessel area at $p = p_{\text{ext}}$. The stiffness parameter β is given by

$$\beta = \frac{\sqrt{\pi} h_0 E}{(1 - \nu^2) A_0}, \tag{9.10}$$

where E is the Youngs modulus, ν is Poisson ratio and h_0 is the reference wall thickness of the vessel [169]. Hence, the constitutive model given in Eq. 9.9, relates instantaneous changes in pressure and cross-sectional area at a local point in a vessel. Substitution of Eq. 9.9 into Eq. 9.8 gives the compliance

$$C = \frac{2\sqrt{A}}{\beta}, \tag{9.11}$$

for the Laplace‘s law model.

9.2.4 System equations

A closed system for the state variables (p, q) may be derived from the 1D equations for conservation of mass and momentum Eq. 9.1 and 9.2, in combination with Eq. 9.5 and 9.6 and the vessel compliance Eq. 9.8;

$$\frac{\partial p}{\partial t} + \frac{1}{C}\frac{\partial q}{\partial z} = 0, \tag{9.12a}$$

$$\frac{\partial q}{\partial t} + \delta\frac{\partial}{\partial z}\left(\frac{q^2}{A}\right) + \frac{A}{\rho}\frac{\partial p}{\partial z} = -2\pi(\gamma+2)\frac{\mu}{\rho}\frac{q}{A}, \tag{9.12b}$$

where $q = vA$ is the flow rate through the cross-section A. The above system can be rearranged and presented as (non-conservative form);

$$\frac{\partial \mathbf{u}}{\partial t} + \mathbf{M}(\mathbf{u})\frac{\partial \mathbf{u}}{\partial z} = \mathbf{b}(\mathbf{u}), \quad \mathbf{u} = \begin{bmatrix} p \\ q \end{bmatrix}, \tag{9.13}$$

with

$$\mathbf{M} = \begin{bmatrix} 0 & \frac{1}{C} \\ C(c^2 - \delta v^2) & 2\delta v \end{bmatrix}, \quad \mathbf{b} = \begin{bmatrix} 0 \\ -2\pi(\gamma+2)\frac{\mu}{\rho}v \end{bmatrix}, \tag{9.14}$$

where c is the pulse wave velocity given by the Bramwell-Hill equation $c^2 C = A/\rho$ [29], and where the relation $\frac{\partial}{\partial z}(\frac{q^2}{A}) = 2v\frac{\partial q}{\partial z} - v^2\frac{\partial A}{\partial z}$ is used.

The eigenvalues of the system matrix $\mathbf{M}$ are given by

$$\lambda_{1,2} = \delta v \pm \acute{c}, \tag{9.15a}$$

where $\acute{c} = c\sqrt{1 + \delta(\delta - 1)\mathcal{M}^2}$, and $\mathcal{M} = v/c$ is the Mach number. The diagonal eigenvalue matrix, and the left and the right eigenvector matrices of the system matrix $\mathbf{M}$, may be presented as

$$\mathbf{\Lambda} = \begin{bmatrix} \lambda_1 & 0 \\ 0 & \lambda_2 \end{bmatrix}, \tag{9.16}$$

$$\mathbf{R} = \begin{bmatrix} Z_1 & -Z_2 \\ 1 & 1 \end{bmatrix} = \begin{bmatrix} \mathbf{r}_1 & \mathbf{r}_2 \end{bmatrix}, \tag{9.17}$$

$$\mathbf{L} = \frac{1}{Z_1 + Z_2}\begin{bmatrix} 1 & Z_2 \\ -1 & Z_1 \end{bmatrix} = \begin{bmatrix} \mathbf{l}_1^T \\ \mathbf{l}_2^T \end{bmatrix}, \tag{9.18}$$

where $Z_1 \equiv \dfrac{1}{C\lambda_1}$ and $Z_2 \equiv -\dfrac{1}{C\lambda_2}$, and $\mathbf{l}_k^T$ and $\mathbf{r}_k$ for $k = \{1, 2\}$ are the left and right eigenvectors respectively. For a zero Mach number, we find that

$$Z_1 = Z_2 = Z_c = \frac{\rho c}{A} = \frac{1}{Cc} \quad \text{for} \quad \mathcal{M} = 0 \tag{9.19}$$

where Z_c is the characteristic impedance. The left and right eigenvectors are chosen so that $\mathbf{LR} = \mathbf{I}$, which allows for the decomposition

$$\mathbf{M} = \mathbf{R}\mathbf{\Lambda}\mathbf{L}. \tag{9.20}$$

The differential system given in Eq. 9.13 can now be presented in the equivalent form by substitution of Eq. 9.20, giving

$$\mathbf{L}\frac{\partial \mathbf{u}}{\partial t} + \mathbf{\Lambda}\mathbf{L}\frac{\partial \mathbf{u}}{\partial z} = \mathbf{L}\mathbf{b}. \tag{9.21}$$

A change in variables is introduced by,

$$\frac{\partial \boldsymbol{\omega}}{\partial \mathbf{u}} = \mathbf{L}, \tag{9.22}$$

where $\boldsymbol{\omega} = [\omega_1, \omega_2]^T$ is a vector of characteristic variables (Riemann variables) [169]. The system presented in Eq. 9.21 can now be transformed into a system of the decoupled characteristic variables

$$\frac{\partial \boldsymbol{\omega}}{\partial t} + \mathbf{\Lambda}\frac{\partial \boldsymbol{\omega}}{\partial z} = \mathbf{L}\mathbf{b}, \tag{9.23}$$

by the introduction of the change in variables presented in Eq. 9.22. Hence, there exists two Riemann variables, give by

$$\boldsymbol{\omega} = \begin{bmatrix} \omega_1 \\ \omega_2 \end{bmatrix} \tag{9.24}$$

with two characteristic directions, determined by the two non-zero eigenvalues (Eq. 9.15a), i.e in the positive and negative z-direction. Integration of Eq. 9.22 from a reference state $\mathbf{u}_0$ to a current state $\mathbf{u}$ at time t, and employing the mean value theorem, gives

$$\Delta\boldsymbol{\omega} = \int_{\mathbf{u}_0}^{\mathbf{u}} \mathbf{L}(\mathbf{u})\, d\mathbf{u} = \mathbf{L}(\hat{\mathbf{u}})\Delta\mathbf{u}, \tag{9.25}$$

$$\Delta\mathbf{u} = \mathbf{R}(\hat{\mathbf{u}})\Delta\boldsymbol{\omega}, \tag{9.26}$$

for $\hat{\mathbf{u}} \in (\mathbf{u}, \mathbf{u}_0)$, and where $\Delta\boldsymbol{\omega} = \boldsymbol{\omega} - \boldsymbol{\omega}_0$.

Wave separation assumes that perturbations in pressure and flow can be split into a forward $(\Delta p_1, \Delta q_1)$ and backward $(\Delta p_2, \Delta q_2)$ component [149]. The total perturbation in pressure and flow $(\Delta p, \Delta q)$ given by the Riemann variables in Eq. 9.26, reads on component from

$$\Delta p = Z_1\Delta\omega_1 - Z_2\Delta\omega_2 \equiv \Delta p_1 + \Delta p_2, \tag{9.27}$$

$$\Delta q = \quad \Delta\omega_1 + \Delta\omega_2 \quad \equiv \Delta q_1 + \Delta q_2. \tag{9.28}$$

where $Z_1 = Z_1(\bar{\mathbf{u}})$ and $Z_1 = Z_1(\bar{\mathbf{u}})$ (Eq. 9.17 and 9.26). From comparing terms in Eq. 9.27-9.28, we arrive at

$$Z_1 = \frac{\Delta p_1}{\Delta q_1} \tag{9.29}$$

$$Z_2 = -\frac{\Delta p_2}{\Delta q_2}. \tag{9.30}$$

Reflection and transmission

A wave encountering a change in the local impedance (e.g. change in cross-sectional area and/or compliance) along a vessel will cause a reflection. The reflection coefficient may be defined as the ratio between an incident pressure wave Δp_1 and the reflected pressure wave Δp_2, caused by a discontinuity in local impedance of an elastic vessel [100], giving

$$\Gamma_p = \frac{\Delta p_2}{\Delta p_1} = -\frac{Z_2 \Delta \omega_2}{Z_1 \Delta \omega_1}, \tag{9.31}$$

and similarly for an incident flow wave Δq_1 and the reflected flow wave Δq_2,

$$\Gamma = -\frac{\Delta q_2}{\Delta q_1} = -\frac{\Delta \omega_2}{\Delta \omega_1}, \tag{9.32}$$

where $-1 \leq \{\Gamma_p, \Gamma\} \leq 1$. For a zero Mach number, we find that

$$\Gamma_p = \Gamma \quad \text{for} \quad \mathcal{M} = 0. \tag{9.33}$$

A reflection coefficient of $\Gamma = 1$ represents a closed vessel, giving total reflection where the reflected wave is a compression wave for an incoming compression wave. A reflection coefficient of $\Gamma = -1$, represents a open vessel (infinitely large reservoir) also causing total reflection, where the reflected wave is an expansion wave for an incoming compression wave. The reflection coefficient Γ can be related to the impedance $Z = \dfrac{\Delta p}{\Delta q}$, eqs. 9.27-9.28 and 9.32, gives

$$\Gamma = \frac{Z - Z_1}{Z + Z_2}. \tag{9.34}$$

The transmission coefficient is defined from the reflection coefficient [191], according to

$$T = 1 + \Gamma. \tag{9.35}$$

Hence, a zero reflection coefficient $\Gamma = 0$ give full transmission $T = 1$ of flow and pressure waves.

9.2.5 Discretization

The 1D system presented in Eq. 9.13 is discretized with the explicit MacCormack scheme [5, 125]. A vessel segment with length L is defined by a uniform grid such that $L = (N - 1)\Delta z$, where N is the number of grid nodes $i = \{1, .., N\}$, and Δz is the nodal spacing. MacCormack's (forward-backward) method gives

$$\widehat{\mathbf{u}}_i = \mathbf{u}_i^n - \Delta t \left(\mathbf{M}(\mathbf{u}_i^n) \frac{(\mathbf{u}_{i+1}^n - \mathbf{u}_i^n)}{\Delta z} + \mathbf{b}(\mathbf{u}_i^n) \right) \tag{9.36}$$

$$\mathbf{u}_i = \frac{1}{2} \left(\mathbf{u}_i^n + \widehat{\mathbf{u}}_i - \Delta t \left(\mathbf{M}(\widehat{\mathbf{u}}_i) \frac{(\widehat{\mathbf{u}}_i - \widehat{\mathbf{u}}_{i-1})}{\Delta z} + \mathbf{b}(\widehat{\mathbf{u}}_i) \right) \right) \tag{9.37}$$

for $i = \{2, .., N-1\}$, where $\Delta t = t - t^n$ is the time step. Hence, the *predictor* step (Eq. 9.36) returns the intermediate state $\widehat{\mathbf{u}}_i$ which is updated in the *corrector* step (Eq. 9.37), giving the state variables $\mathbf{u}_i$ at time $t = t^n + \Delta$. The explicit system is stable for CFL ≤ 1, which is the Courant-Friedrichs-Lewy condition [5], given by CFL $\geq (|u| + c)\frac{\Delta t}{\Delta x}$ in the one-dimensional case. Appropriate boundary conditions needs to be applied at the boundary nodes $i = \{1, N\}$, which is discussed on the following section.

9.2.6 Boundary conditions

Boundary conditions for the discretized system (Eq. 9.36-9.37) are formulated and imposed in a characteristic manner. Linearization of Eqs. 9.25-9.26 around the previous time-step $t^n = t - \Delta t$, gives

$$\Delta \boldsymbol{\omega} = \mathbf{L}(\mathbf{u}^n)\, \Delta \mathbf{u} \tag{9.38}$$

$$\Delta \mathbf{u} = \mathbf{R}(\mathbf{u}^n) \Delta \boldsymbol{\omega}, \tag{9.39}$$

where $\Delta \boldsymbol{\omega} = \boldsymbol{\omega} - \boldsymbol{\omega}^n$ and $\Delta \mathbf{u} = \mathbf{u} - \mathbf{u}^n$, are the local changes in the Riemann variables and the state variables respectively, during a small time increment $\Delta t = t - t^n$. The variable update at the vessels boundaries is determined by Eq. 9.39, giving

$$\widehat{\mathbf{u}}_i = \mathbf{u}_i^n + \mathbf{R}(\mathbf{u}_i^n) \Delta \boldsymbol{\omega}_i, \tag{9.40}$$

$$\mathbf{u}_i = \widehat{\mathbf{u}}_i + \mathbf{R}(\widehat{\mathbf{u}}_i) \Delta \widehat{\boldsymbol{\omega}}_i. \tag{9.41}$$

for $i = \{1, N\}$ (boundary nodes), during the MacCormack *predictor* and *corrector*, respectively. As can be seen from Eq. 9.40 and 9.41, the Riemann variables at time $t = t^n + \Delta t$ are needed. Furthermore, two Riemann variables exist on each boundary surfaces A_1 and A_2 (Fig. 9.2), one leaving and one entering the 1D domain, as illustrated in Fig. 9.2.

The Riemann variables ω_2 at A_1 and ω_1 at A_2, leaving the 1D domain at time $t = t^n + \Delta t$, may be approximated. The system presented in Eq. 9.13, allows us to write

$$\mathbf{l}_k^T \left(\frac{\partial \mathbf{u}}{\partial t} + \mathbf{M} \frac{\partial \mathbf{u}}{\partial z} - \mathbf{b} \right) = 0 \tag{9.42}$$

which, after some manipulation reformulate into

$$\frac{d\, \omega_k(z,t)}{dt} - \mathbf{l}_k^T \mathbf{b} = 0 \tag{9.43}$$

for $k = \{1, 2\}$, where the first term in the total derivative of ω_k along the characteristic paths defined by λ_k in (z, t) space [3, 52]. Discretization of Eq. 9.43 with a first order scheme gives

$$\omega_2(z_1, t) = \omega_2(z_1 - \Delta t \lambda_2, t^n) \quad \text{at} \quad A_1, \tag{9.44}$$

$$\omega_1(z_2, t) = \omega_1(z_2 - \Delta t \lambda_1, t^n) \quad \text{at} \quad A_2, \tag{9.45}$$

where the contribution from the viscous forces in $\mathbf{b}$ are neglected. Hence, the characteristic leaving the domain is approximated by extrapolation of the characteristic approaching the domain boundary at the previous time-step.

The Riemann variables ω_1 at A_1 and ω_2 at A_2 entering the domain at time $t = t^n + \Delta t$, needs to be prescribed according to the choice of boundary conditions.

Proximal/distal conditions

Boundary condition may be enforced in a characteristic manner at A_1 and A_2 (Fig. 9.2), by prescribing the Riemann variables entering the vessel domain, given by

$$\omega_1 = \omega_1(f_1(\omega_2, t),\, g_1(t)) \quad \text{at} \quad A_1, \tag{9.46}$$

$$\omega_2 = \omega_2(f_2(\omega_1, t),\, g_2(t)) \quad \text{at} \quad A_2. \tag{9.47}$$

Hence, the Riemann variables entering the domain at A_1 and A_2, may generally be functions of some boundary models $f_1(\omega_2, t)$ and $f_2(\omega_2, t)$, which are dependent on the conditions inside the vessel domain given by the Riemann variables leaving the vessel, ω_2 at A_1 and ω_1 at A_2 (e.g. lumped model boundary conditions). Additionally, the Riemann variables entering the domain at A_1 and A_2 may be functions of some state property $g_1(t)$ and $g_2(t)$ entering the vessel, e.g. a predicted flow rate, pressure or change in cross-sectional area.

Prescribed flow

A forward propagating flow $q_1 = g_1(t)$ at the left boundary A_1 can be prescribed on the Riemann variable ω_1 entering the domain (Fig. 9.2). From Eq. 9.28 we realize that as $q_1 = g_1(t)$,

$$\Delta\omega_1 = \Delta g_1 \quad \text{at} \quad A_1. \tag{9.48}$$

where $\Delta g_1 = g_1 - g_1^n$. Hence, Eq. 9.48 is a special case of the prescribed forward propagating Riemann variable given in Eq. 9.46, where $\omega_1 = \omega_1(g_1(t))$. Substitution of Eq. 9.48 into Eq. 9.24, gives

$$\Delta\boldsymbol{\omega} = \begin{bmatrix} \Delta g_1 \\ \Delta\omega_2 \end{bmatrix} \quad \text{at} \quad A_1, \tag{9.49}$$

where the Riemann variable $\Delta\omega_2$ leaving the domain at A_1, is extrapolated as given in Eq. 9.44. The variable update $\Delta\mathbf{u}$ at A_1, is now given by Eq. 9.26 and 9.49,

$$\Delta\mathbf{u} = \begin{bmatrix} \Delta p \\ \Delta q \end{bmatrix} = \mathbf{R}\,\Delta\boldsymbol{\omega} = \begin{bmatrix} Z_1\Delta g_1 - Z_2\Delta\omega_2 \\ \Delta g_1 + \Delta\omega_2 \end{bmatrix} \quad \text{at} \quad A_1. \tag{9.50}$$

An imposed flow with this formulation results in an absorbing formulation at the boundary A_1, meaning that a forward propagating flow rate can be prescribed while at the same time allowing outgoing waves from the domain to exit without being reflected. As only the forward propagating flow Δq_1 is prescribed, the net flow Δq is free the vary due to $\Delta q = \Delta g_1 + \Delta\omega_2$ (see Eq. 9.50). Boundary formulations of this nature have been used to model flow trough an open aortic valve, when no reflections from the ventricle is assumed [51, 169].

Terminal reflection

A boundary condition which acts as a terminal reflection point can be prescribed through the reflection coefficient Γ (Eq. 9.32). A terminal reflection boundary condition for the right boundary A_2 (Fig. 9.2), is constructed by prescribing the Riemann variable $\Delta\omega_2$ entering the domain

at A_2. By similar arguments as given in Sec. 9.2.6 (Prescribed flow), and from Eq. 9.47, we define

$$\Delta\omega_2 = \Delta f_2(\omega_1, t), \quad \text{at} \quad A_2, \tag{9.51}$$

where $\Delta f_2(\omega_1, t) = -\Gamma\,\Delta\omega_1$ (Eq. 9.32), giving

$$\Delta\boldsymbol{\omega} = \begin{bmatrix} \Delta\omega_1 \\ -\Gamma\,\Delta\omega_1 \end{bmatrix} \quad \text{at} \quad A_2, \tag{9.52}$$

and state variable update (Eq. 9.24 and 9.39)

$$\Delta\mathbf{u} = \begin{bmatrix} (Z_1 + \Gamma Z_2)\,\Delta\omega_1 \\ (1-\Gamma)\,\Delta\omega_1 \end{bmatrix} \quad \text{at} \quad A_2. \tag{9.53}$$

where the Riemann variable leaving the domain, $\Delta\omega_1$, is extrapolated as given in Eq. 9.45. Hence, the Riemann variable leaving the domain is reflected back into domain with an amplitude depending on the reflection coefficient Γ. Several studies have used this type of boundary condition to model the reflection of flow and pressure waves caused by the resistance of the capillary bed at the distal ends of the arterial tree [51, 168]. As can be seen from Eq. 9.41, an absorbing terminal boundary (reflection free) can be enforced by, $\Gamma \equiv 0$, i.e. the Riemann variable entering the domain $\Delta\omega_2$ at A_2 is set to zero.

Prescribed flow and terminal reflection

A forward propagating flow $q_1 = g_1(t)$ and a reflection point can by prescribed to the left boundary A_1, on the Riemann variable ω_1 entering the domain (Fig. 9.2). Again, by similar arguments as given in Sec. 9.2.6 (Prescribed flow and Terminal reflection), and from Eq. 9.46, we define

$$\Delta\omega_1 = \Delta g_1 + \Delta f_1(\omega_2, t) \quad \text{at} \quad A_1, \tag{9.54}$$

where $\Delta f_1(\omega_2, t) = -\Gamma\,\Delta\omega_2$, giving

$$\Delta\boldsymbol{\omega} = \begin{bmatrix} \Delta g_1 - \Gamma\,\Delta\omega_2 \\ \Delta\omega_2 \end{bmatrix} \quad \text{at} \quad A_1, \tag{9.55}$$

and state variable update (Eq. 9.24 and 9.55)

$$\Delta\mathbf{u} = \begin{bmatrix} Z_1\Delta g_1 - (Z_2 + \Gamma Z_1)\,\Delta\omega_2 \\ \Delta g_1 + (1-\Gamma)\,\Delta\omega_2 \end{bmatrix} \quad \text{at} \quad A_1. \tag{9.56}$$

where the Riemann variable leaving the domain, $\Delta\omega_2$, is extrapolated as given in Eq. 9.45. In this boundary formulation, a flow $g_1(t)$ can be prescribed to enter the vessel at the A_1, while at the same time allow waves from the domain to be reflected with an amplitude depending on the reflection coefficient Γ. Hence, a reflection coefficient of $\Gamma = 0$, returns the absorbing boundary formulation for a forward propagating flow $q_1 = g_1(t)$ at the left boundary A_1, as given in Eq. 9.50.

Terminal resistance

A terminal resistance R_f can be imposed as a boundary condition for a 1D vessel, as illustrated in Fig. 9.3 for the right boundary A_2. The resistance compartment R_f can for example represent the lumped preferential resistance of a vascular bed beyond the domain of the 1D model.

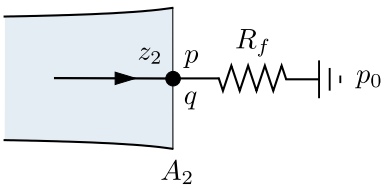

Figure 9.3 Schematic illustration of a resistance compartment R_f connected to a 1D vessel.

The resistance model is governed by

$$\frac{p - p_0}{R_f} = q, \tag{9.57}$$

where p and q are pressure and flow at the boundary node of the 1D vessel, and where p_0 is pressure in the lumped model reservoir (Fig. 9.3). A resistance compartment connected to the right vessel boundary A_2, as seen in Fig. 9.3, requires an expression for the Riemann variable ω_2 entering the domain. Rewriting the resistance model presented in Eq. 9.57 for incremental changes in pressure and flow $(\Delta p, \Delta q)$ at the boundary node, which can conveniently be represent by the Riemann variables from the definition in Eqs. 9.27-9.28, gives

$$\Delta\omega_2 = \frac{-(R_f - Z_1)\,\Delta\omega_1 - \Delta p_0}{R_f + Z_2}, \quad \text{at} \quad A_2, \tag{9.58}$$

where the Riemann variable $\Delta\omega_1$ leaving the boundary at A_2 needs to be extrapolated as given in Eq. 9.45. The boundary variables can now be updated by solving for $\Delta\mathbf{u} = \mathbf{R}\,\Delta\boldsymbol{\omega}$ (Eq. 9.39).

By letting the impedance in Eq. 9.34 be replaced with the resistance compartment in 9.58, i.e. $Z \equiv R_f$, we find that the resistance model is related to a reflection boundary condition, given by

$$\Delta\omega_2 = -\Gamma\,\Delta\omega_1 - \frac{\Delta p_0}{R_f + Z_2}, \quad \text{at} \quad A_2. \tag{9.59}$$

Terminal three-element Windkessel

Windkessel models are frequently used as terminal boundary conditions for distributed 1D networks [3, 51, 128, 142, 159, 177, 183]. The basic (two-element) Windkessel model consists of a lumped compliance compartment connected in parallel with a lumped resistance compartment [193]. Hence, contrary to the pure resistance model, both the lumped resistance to flow

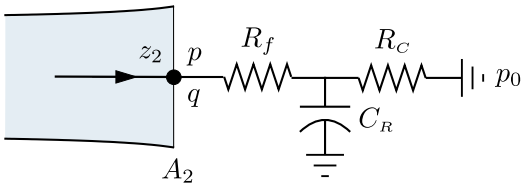

Figure 9.4 Schematic illustration of a three-element Windkessel model connected to a 1D vessel, with a resistance compartment R_f, connected in series to a parallel resistance R_C and compliance C_R circuit.

and the elastic distensibility due to pressure of a vessel or vascular bed, can be modeled with a Windkessel model.

A schematic illustration of a three-element Windkessel (WK) connected to a 1D vessel, is given in Fig. 9.4. The WK model is governed by a resistance compartment R_f, connected in series to a parallel resistance R_C and compliance C_R circuit. The WK model, may be presented as

$$\frac{dp}{dt} + \frac{(p - p_0)}{\tau} = \frac{dq}{dt} R_f + \frac{q}{\tau} \left(R_C + R_f \right), \tag{9.60}$$

where $\tau = R_C C_R$ is a time constant. A WK terminal boundary condition is developed in a similar manner to the resistance boundary condition in the previous section, i.e. pressure and mass flow rate at the boundary node are substituted with Riemann variables. The time derivatives for incremental changes of pressure and flow rate in Eq. 9.60, after substitution of Eqs. 9.28-9.29 and temporal discretization with a first order scheme, gives

$$\frac{d\left(\Delta p\right)}{dt} = Z_1 \frac{\Delta\omega_1 - \Delta\omega_1^n}{\Delta t} - Z_2 \frac{\Delta\omega_2 - \Delta\omega_2^n}{\Delta t} \tag{9.61}$$

$$\frac{d\left(\Delta q\right)}{dt} = \frac{(\Delta\omega_1 - \Delta\omega_1^n)}{\Delta t} + \frac{(\Delta\omega_2 - \Delta\omega_2^n)}{\Delta t} \tag{9.62}$$

for $\Delta t = t - t^n$, where the time derivative of Z_1 and Z_2 are neglected.

A WK model connected to the right boundary A_2, as seen in Fig. 9.4, is imposed on the Riemann variable ω_2 entering the domain. Flow and pressure enters the WK model on the Riemann variable ω_1 leaving the domain at A_2, which needs to extrapolated as given in Eq. 9.45. The Riemann variable entering the domain at A_2 is found from rewriting the WK model (Eq. 9.60) for incremental changes in pressure and flow $(\Delta p, \Delta q)$, followed by substitution of

Eqs. 9.28-9.29 and 9.61-9.62, which gives

$$\Delta\omega_2 = \frac{b_2\Delta\omega_2^n + a_1\Delta\omega_1 + b_1\Delta\omega_1^n - \Delta p_0}{a_2}, \quad \text{at} \quad A_2, \tag{9.63}$$

$$a_1 = -\left(\frac{\tau}{\Delta t} + 1\right)(R_f - Z_1) - R_C,$$

$$a_2 = \left(\frac{\tau}{\Delta t} + 1\right)(R_f + Z_2) + R_C,$$

$$b_1 = \frac{\tau}{\Delta t}(R_f - Z_1),$$

$$b_2 = \frac{\tau}{\Delta t}(R_f + Z_2).$$

Finally, the variables update at the boundary is determined by solving for $\Delta\mathbf{u} = \mathbf{R}\,\Delta\boldsymbol{\omega}$ (Eq. 9.39).

The input impedance of the WK model is frequency dependent

$$Z_{\text{WK}}(w) = R_f + \frac{R_C}{1 + jw\tau}, \tag{9.64}$$

given time periodic solutions on the form $p(t) = \tilde{p}\,e^{jwt}$ and $q(t) = \tilde{q}\,e^{jwt}$, where $j = \sqrt{-1}$ and w is an angular frequency. Hence, for higher frequencies the WK model approaches a pure resistance model. This quality can be exploited, by choosing R_f to be equal to the impedance of the boundary node that connects to the WK model, e.g. $R_f \equiv Z_1|_{A_2}$, and the WK model will absorb high frequency incoming waves [183] (as seen from Eq. 9.58).

Network bifurcations

The vascular system is composed of a network of diverging and converging arteries and veins. The branching points are most often bifurcations where three vessels meet to split or merge the blood flow.

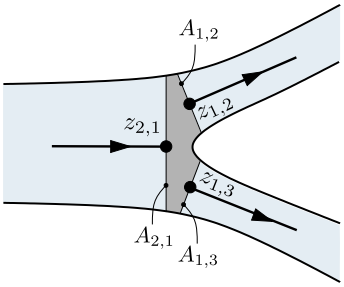

Figure 9.5 Network bifurcation, at the three nodal positions $z_{2,1}$, $z_{1,2}$ and $z_{1,3}$. The first subscript denotes the vessels left (1) or right (2) boundary, and the second subscript denotes the vessel number. The arrows indicates the positive z-directions. Adapded from Sherwin et al. [169].

A diverging bifurcation is defined as given in Fig. 9.5, where the positive direction along the z-axis of a parent vessel, splits into two daughter vessels. Hence, the A_2 boundary of the parent

vessel connects to two daughter vessels at their A_1 boundaries. The bifurcation is defined by the three nodal points $z_{2,1}$, $z_{1,2}$ and $z_{1,3}$ (Fig. 9.5), with the associated sets of state variables $\mathbf{u}_{,1}$, $\mathbf{u}_{,2}$ and $\mathbf{u}_{,3}$. The system is solved by first assuming conservation of mass and total pressure

$$q_{,1} = q_{,2} + q_{,3}, \tag{9.65a}$$

$$p_{,1} + \frac{\rho}{2} v_{,1}^2 = p_{,2} + \frac{\rho}{2} v_{,2}^2, \tag{9.65b}$$

$$p_{,1} + \frac{\rho}{2} v_{,1}^2 = p_{,3} + \frac{\rho}{2} v_{,3}^2, \tag{9.65c}$$

between the three vessels. Furthermore, the incremental change in the variables $\mathbf{u}_{,1}$, $\mathbf{u}_{,2}$ and $\mathbf{u}_{,3}$ at the three boundaries, are required to satisfy

$$\Delta\omega_{1,1} - \mathbf{l}_{1,1}^T \Delta\mathbf{u}_{,1} = 0, \tag{9.66a}$$

$$\Delta\omega_{2,2} - \mathbf{l}_{2,2}^T \Delta\mathbf{u}_{,2} = 0, \tag{9.66b}$$

$$\Delta\omega_{2,3} - \mathbf{l}_{2,3}^T \Delta\mathbf{u}_{,3} = 0, \tag{9.66c}$$

where $\omega_{1,1}$, $\omega_{2,2}$ and $\omega_{2,3}$ are the Riemann variables leaving the three vessels at the bifurcation, which are extrapolated from the domain of each vessel (Eq. 9.44 and 9.45). Hence, Eqs 9.66a-9.66c state that the Riemann variables leaving the three vessels should remain constant. The system represent by the six equations 9.65a-9.66c, is solved with a Newton iteration scheme each MacCormack *predictor* and *corrector* step (Eq. 9.37 and 9.36).

A converging bifurcation is solved for in a similar manner, where the positive direction is defined along two daughter vessels which merge into one parent vessel. Hence, for a converging bifurcation the A_1 boundary of the parent vessel connects to two daughter vessels at their A_2 boundaries. Additionally, a connection between two vessels or a branching point between more than three vessels can also be defied by the approach outlined above.

Pressure and flow waves approaching a bifurcation may be reflected depending on the impedance mismatch between the connected vessels. For the bifurcation illustrated in Fig. 9.5, the reflection coefficient (linearized) for waves approaching the bifurcation in the mother vessel towards $z_{2,1}$, is given by

$$\Gamma = \frac{\frac{1}{Z_{c,1}} - \frac{1}{Z_{c,2}} - \frac{1}{Z_{c,3}}}{\frac{1}{Z_{c,1}} + \frac{1}{Z_{c,2}} + \frac{1}{Z_{c,3}}}, \tag{9.67}$$

where $Z_{c,1}$, $Z_{c,2}$ and $Z_{c,3}$ are the characteristic impedances of the connected boundaries of the three vessels [169]. For example, a well match bifurcation for waves approaching $z_{2,1}$ requires $\Gamma = 0$ (no reflections), Eq. 9.67 yields

$$Z_{c,1} = \frac{Z_{c,2} Z_{c,3}}{Z_{c,2} + Z_{c,3}}, \tag{9.68}$$

which if we require $Z_{c,2} = Z_{c,3}$, gives $Z_{c,2} = 2\, Z_{c,1}$.

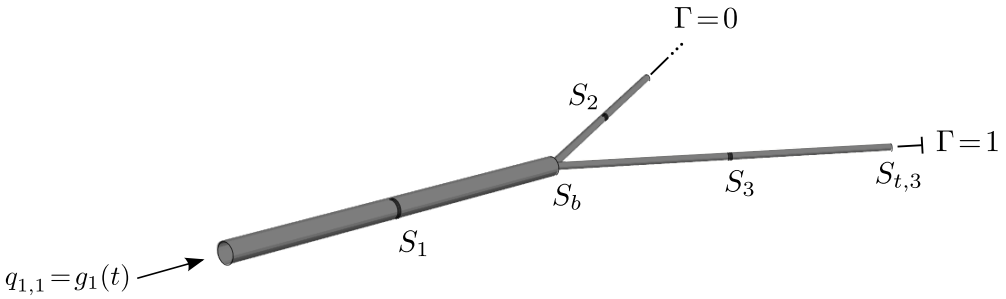

Figure 9.6 Three vessels connected in a bifurcation at S_b. The vessel midpoints are given by S_1, S_2 and S_3. Vessel number one is given an inflow of $q_{1,1} = g_1(t)$ at its left boundary. Vessel two is given a reflection free boundary $\Gamma = 0$ at its right boundary, and the right boundary of vessel three is closed, i.e $\Gamma = 1$ at $S_{t,3}$.

Table 9.1 Bifurcation parameters

vessel	A_0 (mm^2)	L_0 (m)	β (kPa/m)
1	78.5	0.2	324.97
2	13.1	0.2	796.02
3	13.1	0.2	796.02

9.3 Numerical results

Bifurcation

The discretized 1D distributed model for blood flow in compliant vessel networks is tested in a simplified validation case provided by Xiu and Sherwin [195]. The test case consists of three vessels connected in a bifurcation, marked by S_b as seen in Fig. 9.9. Initial geometrical and stiffness parameter for the three vessels are given in Table 9.1. The (linearized) wave speeds of the three vessels are $c_0 = 1.2$ m/s, derived from the compliance given by Laplace law Eq. 9.8 and the Bramwell-Hill equation, for the particular choice of parameters in Table 9.1. The fluid density is set to $\rho = 1000\,\text{kg/m}^3$. A flat velocity profile is chosen, i.e a shape function $\phi = 1$ (Eq. 9.3), with gives inviscid flow and $\delta = 1$.

At the inlet of vessel one we prescribe a forward propagating flow

$$q_{1,1} = g_1(t) = q_0 \exp\left(-\frac{1}{2}\left(\frac{t - t_0}{\sigma}\right)^2\right), \tag{9.69}$$

where $q_0 = u_0 A_0$ for $u_0 = 5\,\text{mm/s}$, $\sigma = 0.01\,\text{s}$ and $t_0 = 0.05\,\text{s}$. The inflow is prescribed on the Riemann variable entering vessel one at the left boundary in an absorbing formulation, as presented in Eq. 9.50. Vessel two is given a reflection free boundary $\Gamma = 0$ at its right outlet, while vessel three is given a reflection boundary with $\Gamma = 1$ at its right outlet, i.e closed outlet. The reflection boundary conditions for vessel two and three are imposed as given in Eq. 9.51. The bifurcation point S_b between the three vessels is imposed as described in Eqs. 9.65a-9.66c,

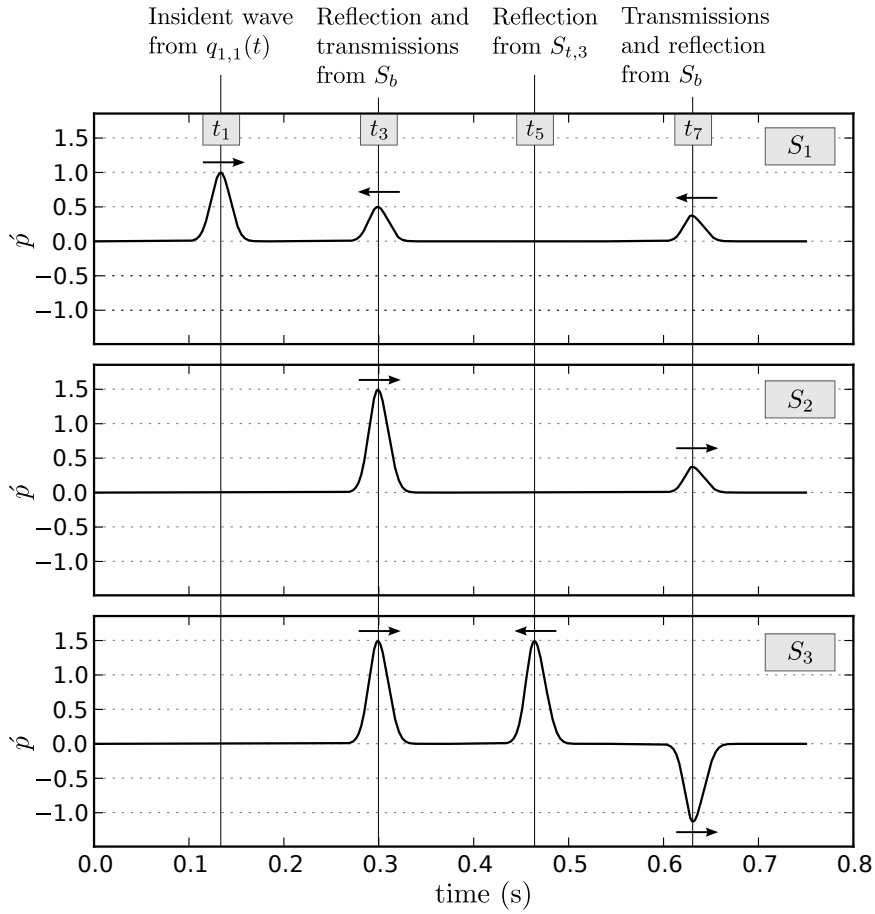

Figure 9.7 Normalized pressure waveforms $\acute{p} = \frac{p}{p_{1,1}}$ at the midpoints, S_1, S_2 and S_3 of three vessels forming a bifurcation at S_b. The pressure waveforms are normalized with the pressure wave amplitude $p_{1,1}$, associated with the incident flow $q_{1,1}$ in vessel number one, see Fiq. 9.6. Peak amplitudes can be seen at time-points t_1, t_3, t_5 and t_7 at the midpoints of the three vessels (see also Fig. 9.8).

i.e. a diverging bifurcation with positive z direction towards the bifurcation for vessel one, and positive z directions away from the bifurcation for vessels two and three. The base frequency of the inflow is approximately $f \approx \frac{1}{5\,\sigma} = 20$Hz which is much higher than e.g. a normal heart beat. The wave length is $l_w = c_0/f \approx 6$ cm which is shorter that the lengths of individual vessels. The high inflow frequency and the short wavelength in this test case will give a clearer visualization of the dynamics of the system, although it is not directly physiological with regards to wave propagation in human blood vessels. The vessels are each discretized with 401 nodal points, and the $[\text{CFL}]_0 = c_0 \frac{\Delta t}{\Delta z}$ number is set to 0.95.

The (linearized) reflection coefficient for waves approaching the bifurcation in vessel one is $\Gamma = 0.5$, given by the chosen dimensions of the three vessels and the common wave speed c_0. As can be shown by substitution of the cross-sectional areas in Table 9.1 into Eq. 9.69, where $Z_{c,m} = A_{0,m}\, c_0/\rho$ for the three vessels $m = \{1, 2, 3\}$. The waves transmitted through the bifurcation from vessel one have a transmission coefficient of $T = 1.5$ (Eq. 9.35). How-

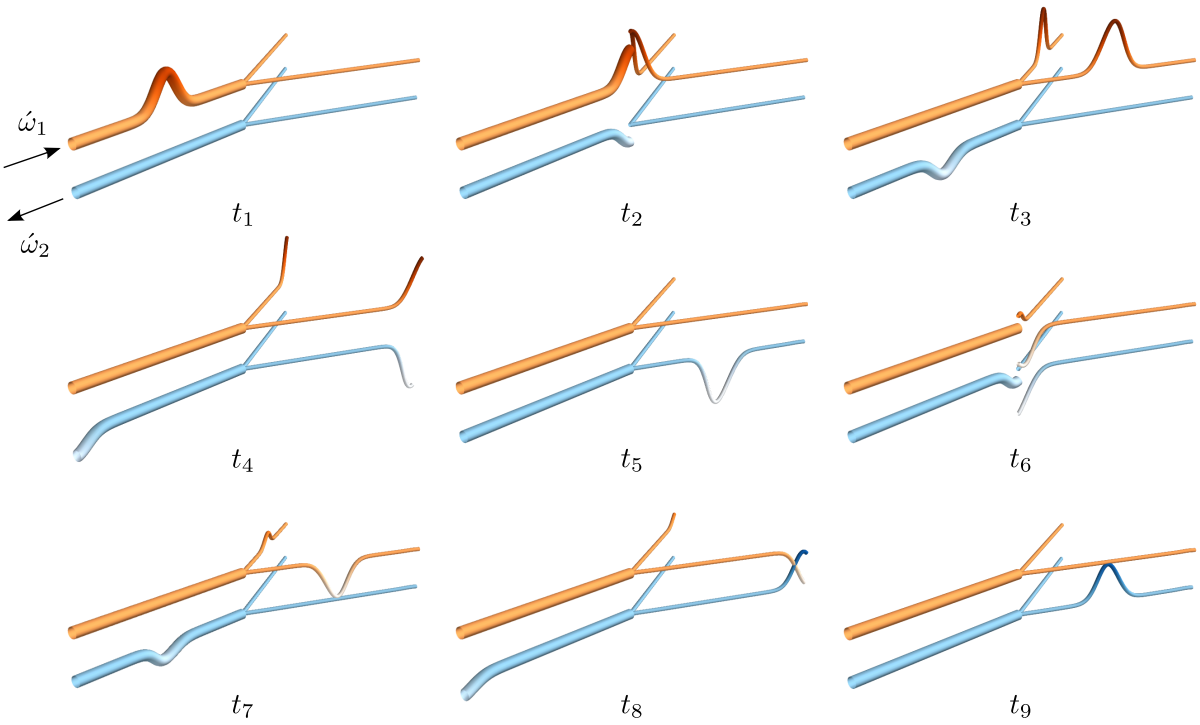

Figure 9.8 Normalized Riemann variables $\acute{\omega}_1$ and $\acute{\omega}_2$ at nine time points t_1 to t_9 as they propagate through the three vessels forming a bifurcation, given in Fig. 9.6. The Riemann variables are modified to have velocity units and are normalized with the amplitude of the incident Riemann variable $\omega_{1,1}$ from the inflow $q_{1,1}$, giving $\acute{\omega}_1(t) = \frac{\omega_1(t)}{A(t)\,\omega_{1,1}}$ and $\acute{\omega}_2(t) = \frac{\omega_2(t)}{A(t)\,\omega_{1,1}}$. The direction of the Riemann variables are illustrated in time-point t_1, $\acute{\omega}_1$ propagate from left to right (orange vessels) and $\acute{\omega}_2$ propagate from right to left (blue vessels). The vertical displacement of the tubes (and colorization) represent the local amplitudes of the Riemann variables.

ever, waves approaching the bifurcation from either vessel two or three have have a theoretical reflection coefficient of $\Gamma = -0.75$ (Eq. 9.68 and Table 9.1) and a corresponding transmission coefficient of $T = 0.25$. Hence, a reflected wave from the bifurcation in vessel two or three will be expansion waves due to the negative reflection coefficient.

Normalized pressure waveforms $\acute{p}$ as functions of time are plotted in Fig. 9.7, at the midpoints, S_1, S_2 and S_3 of the three vessels (Fig. 9.6). The pressure waveforms are normalized with the incident pressure amplitude $p_{1,1} = 6.0\,\text{Pa}$, associated with the incident flow $q_{1,1}$ (Eq. 9.69) in vessel number one. The incident wave reaches the midpoint of vessel one S_1 at t_1, and propagate towards the bifurcation at S_b. At time-point t_3, a reflected wave from the bifurcation again passes the midpoint of vessel one with half the amplitude of the incident wave as predicted from the reflection factor for the bifurcation $\Gamma = 0.5$, i.e $[\acute{p}]_{S_1,t_3} = 0.5\ [\acute{p}]_{S_1,t_1} = 0.5$. The transmitted waves reaches the midpoints of vessels two and three at time-point t_3, and their amplitudes are in accordance with the transmittance $T = 1.5$, i.e $[\acute{p}]_{S_3,t_3} = 1.5\ [\acute{p}]_{S_1,t_1} = 1.5$.

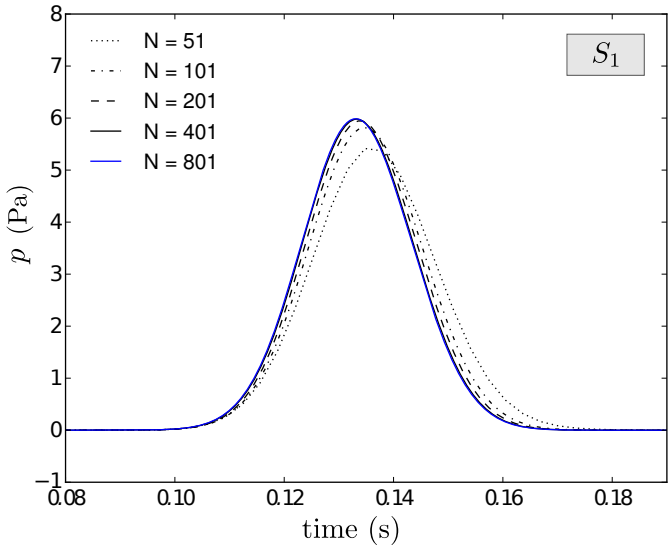

Figure 9.9 The pressure wave at the midpoint of vessel one for increasing grid resolution, $N = \{51, 101, 201, 401, 801\}$.

The reflected wave from the terminal reflection point at the right boundary of vessel three reaches the midpoint of vessel three at time-point t_5, with equal amplitude as at time-point t_3, i.e $[\acute{p}]_{S_3,t_5} = [\acute{p}]_{S_3,t_3}$, due to the terminal reflection coefficient of $\Gamma = 1$ at $S_{f,3}$ (Fig. 9.6). The reflected wave from the bifurcation in vessel three, reaches the midpoint of vessel three at time-point t_7, the amplitude is in accordance with the reflection coefficient for the bifurcation for a wave approaching from vessel three $\Gamma = -0.75$, i.e. $[\acute{p}]_{S_3,t_7} = -0.75\ [\acute{p}]_{S_1,t_5} = -1.125$. Furthermore, the pressure wave is an expansion wave due the the negative pressure amplitude. The transmitted waves from the last wave interaction with the bifurcation, reaches the midpoints of vessels one and two at time-point t_7, and their amplitudes are in accordance with a transmittance coefficient of $T = 0.25$, i.e $[\acute{p}]_{S_2,t_7} = 0.25\ [\acute{p}]_{S_1,t_5} = 0.375$.

The normalized Riemann variables $\acute{\omega}_1$ and $\acute{\omega}_2$ are plotted in Fig. 9.8, as they propagate through the three vessels at nine time points t_1 to t_9. The inflow from the left boundary of vessel one, is seen as it propagate towards the bifurcation on $\acute{\omega}_1$, at time-point t_1. At time-point t_3, only left traveling waves are present in vessel one on $\acute{\omega}_2$, and only right traveling waves are present in vessels two and three on $\acute{\omega}_1$. The reflected and transmitted waves reaches the vessel boundaries at time-point t_4, and as can be seen at time-point t_5, only the wave hitting the terminal reflective boundary at $S_{f,3}$ is reflected back into the system.

Grid sensitivity

The incident pressure wave at the midpoint of vessel one is plotted in Fig. 9.9 for increasing grid resolution, $N = \{51, 101, 201, 401, 801\}$. The $[\text{CFL}]_0$ number is kept constant at 0.95, hence both the spatial Δz and temporal Δt resolution is increasing for increasing number of grid points. Fig. 9.9 illustrates that both the amplitude and the timing of the pressure wave is affected by the grid resolution. Low grid resolution, causes a decrease in the pressure amplitude

and the pressure wave arrives later at the midpoint S_1 of vessel one. However, for increasing grid resolution the solution converges towards the expected (linearized) incident pressure amplitude $[p]_{S_1,t_1} = Z_{c,1}\, q_{1,1} = \rho\, c_0\, u_0 = 6\,\text{Pa}$, and arrival time $t_1 = t_0 + \frac{L_0}{2\,c_0} = 1.33\,\text{s}$.

Conservation of mass

Conservation of mass is tested for a single vessel with cross-sectional area A_0 and stiffness parameter β, equal to vessel one in Table 9.1. The vessel is given the inflow in Eq. 9.69, and a reflection boundary with $\Gamma = 1$ at its right outlet, i.e closed outlet. Mass conservation is calculated as the difference between the mass m_{in} entering the vessel on the incident flow wave $q_{1,1}$, and the mass m_{out} exiting the vessel at the inlet, after being fully reflected at the right boundary, i.e $m_\varepsilon = 100\,(1 - \dfrac{m_{\text{out}}}{m_{\text{in}}})$. Three different vessel lengths are tested $L_0 = \{0.2\,\text{m}, 0.4\,\text{m}, 0.8\,\text{m}\}$, with node spacing $N = \{401, 801, 1601\}$ and CFL number 0.95. The difference in mass entering and exiting the vessels with the three different lengths are found to be $m_\varepsilon = \{0.047\,\%,\ 0.096\,\%,\ 0.201\,\%\}$. Hence, a small loss of mass is present after the incident wave has traveled twice the vessel length, and this loss increases with increasing vessel length.

9.4 Conclusions

In this work, we have presented a 1D vascular network model, aimed for applications in the feto-placental circulation. The model is derived from the governing equations for 1D flow in compliant vessels and discretized with the explicit MacCormack scheme. Boundary conditions are imposed in a characteristics manner by the linearized Riemann variables (Eqs. 9.38-9.39). By employing the linearized Riemann variables we avoid the need for an explicit form of the Riemann variables by full integration of Eq. 9.22, which may be considered the more common approach, see e.g [3, 50, 143, 169]. Integration of the Riemann variables is not always possible, and depends on the choice of constitutive models for the vessels compliance. Moreover, we show that the Riemann variables linearized around the previous time-step incorporates well in the explicit MacCormack scheme (Eqs. 9.40-9.41). A flexible framework for the imposition of flow (and pressure) boundary conditions is outlined such that reflections points at the flow inlet/outlets may be accounted for (Eq. 9.56), e.g. to model reflection from the ventricle and aortic valve while at the same time allow for flow to be ejected into the vascular system. The proposed formulation for imposition of boundary conditions, by constructing an characteristic vector $\Delta\boldsymbol{\omega}$ and solving for the system $\Delta\mathbf{u} = \mathbf{R}\Delta\boldsymbol{\omega}$ at the boundaries (Eq. 9.39), means that complex lumped models (formulated as ODEs) may also be incorporated with ease, e.g. WK models (Eq. 9.63). Our explicit numerical scheme is well suited for parallelization, as the solution in each vessel is a function of local information and information from other vessel at the previous time step.

The high frequency and the short wave length of the inflow signal in the bifurcation test case [195], required a relative fine grid resolution with the employed numerical scheme as seen in Fig. 9.9. However, physiological frequencies of the heart are much lower and typical wave

lengths are much longer in the human body. Hence, physiological conditions can be modeled with good accuracy with relatively few grid nodes per vessel. Our model results from the bifurcation test case agrees with the results provided by Xiu and Sherwin [195], and with the analytical (linearized) expected values for reflection and transmission of pressure waves, as seen in Fig. 9.8. A small loss of mass is found in a single vessel test case, however within acceptable limits for the indented applications and vessel network sizes.

In conclusion, we have provided a framework for 1D vascular network simulation with the explicit MacCormack scheme, where non-linearities due to vessel compliance and characteristic boundary conditions can be treated efficiently. The model is developed for applications in the feto-placental circulation, however we have successfully simulated large arterial networks, as given by Sherwin et al. [168], Stergiopulos et al. [177], with the current modeling approach.

Bibliography

[1] Acharya, G. and T. Kiserud (1999). Pulsations of the ductus venosus blood velocity and diameter are more pronounced at the outlet than at the inlet. *European Journal of Obstetrics, Gynecology and Reproductive Biology 84*(2), 149–154.

[2] Ailamazyan, E., O. Kirillova, A. Polyanin, and I. Kogan (2003). Functional morphology of ductus venosus in human fetus. *Neuroendocrinology Letters 24*(1/2), 28–32.

[3] Alastruey, J., K. Parker, J. Peiró, and S. Sherwin (2008). Lumped parameter outflow models for 1-D blood flow simulations: effect on pulse waves and parameter estimation. *Communications in Computational Physics 4*, 317–336.

[4] Alastruey, J., S. Sherwin, K. Parker, and D. Rubens (2009). Placental transfusion insult in the predisposition for SIDS: A mathematical study. *Early Human Development 85*(7), 455–459.

[5] Anderson, J. and J. Wendt (1995). *Computational fluid dynamics*, Volume 206. McGraw-Hill.

[6] Bahlmann, F., S. Wellek, I. Reinhardt, E. Merz, E. Steiner, and C. Welter (2000). Reference values of ductus venosus flow velocities and calculated waveform indices. *Prenatal Diagnosis 20*(8), 623–634.

[7] Bańkowski, E. (1999). Collagen of the umbilical cord and its alteration in EPH-gestosis (preeclampsia). *Journal Of Chemical Sciences 111*(1), 207–213.

[8] Bańkowski, E., K. Sobolewski, L. Romanowicz, L. Chyczewski, and S. Jaworski (1996). Collagen and glycosaminoglycans of Wharton's jelly and their alterations in EPH-gestosis. *European Journal of Obstetrics, Gynecology and Reproductive Biology 66*(2), 109–117.

[9] Barcroft, J. (1946). The development of vascular reflexes. *Researches On Prenatal Life*, 123–144.

[10] Baschat, A., U. Gembruch, and C. Harman (2001). The sequence of changes in Doppler and biophysical parameters as severe fetal growth restriction worsens. *Ultrasound in Obstetrics & Gynecology 18*(6), 571–577.

[11] Batina, J. (1990). Unsteady Euler airfoil solutions using unstructured dynamic meshes.

AIAA Journal 28(8), 1381–1388.

[12] Bazilevs, Y., V. Calo, T. Hughes, and Y. Zhang (2008). Isogeometric fluid-structure interaction: theory, algorithms, and computations. *Computational Mechanics 43*(1), 3–37.

[13] Bazilevs, Y., V. Calo, Y. Zhang, and T. Hughes (2006). Isogeometric fluid–structure interaction analysis with applications to arterial blood flow. *Computational Mechanics 38*(4), 310–322.

[14] Bazilevs, Y., J. Gohean, T. Hughes, R. Moser, and Y. Zhang (2009). Patient-specific isogeometric fluid-structure interaction analysis of thoracic aortic blood flow due to implantation of the Jarvik 2000 left ventricular assist device. *Computer Methods in Applied Mechanics and Engineering 198*(45), 3534–3550.

[15] Beaudoin, S., F. Bargy, D. Mahieu, and P. Barbet (1998). Anatomic study of the umbilical vein and ductus venosus in human fetuses: ultrasound application in prenatal examination of left congenital diaphragmatic hernia. *Surgical and Radiologic Anatomy 20*(2), 99–103.

[16] Bellotti, M., G. Pennati, C. De Gasperi, F. Battaglia, and E. Ferrazzi (2000). Role of ductus venosus in distribution of umbilical blood flow in human fetuses during second half of pregnancy. *American Journal of Physiology: Heart and Circulatory Physiology 279*(3), H1256.

[17] Bellotti, M., G. Pennati, C. Gasperi, M. Bozzo, F. Battaglia, and E. Ferrazzi (2004). Simultaneous measurements of umbilical venous, fetal hepatic, and ductus venosus blood flow in growth-restricted human fetuses. *American Journal Of Obstetrics and Gynecology 190*(5), 1347–1358.

[18] Bellotti, M., G. Pennati, G. Pardi, and R. Fumero (1998). Dilatation of the ductus venosus in human fetuses: ultrasonographic evidence and mathematical modeling. *American Journal of Physiology: Heart and Circulatory Physiology 275*(5), H1759.

[19] Belytschko, T., W. Liu, and B. Moran (2000). *Nonlinear finite elements for continua and structures*, Volume 1. Wiley New York.

[20] Benirschke, K. and P. Kaufmann (2000). *Pathology of the human placenta*. Springer Verlag.

[21] Benirschke, K., P. Kaufmann, and R. Baergen (2006). Anatomy and pathology of the umbilical cord. In *Pathology of the Human Placenta*, pp. 380–451. Springer New York.

[22] Bertrand, C., L. Duperron, and J. St-Louis (1993). Umbilical and placental vessels: modifications of their mechanical properties in preeclampsia. *American Journal Of Obstetrics and Gynecology 168*(5), 1537–1546.

[23] Bessems, D., C. Giannopapa, M. Rutten, and F. van de Vosse (2008). Experimental validation of a time-domain-based wave propagation model of blood flow in viscoelastic vessels. *Journal Of Biomechanics 41*(2), 284–291.

[24] Bessems, D., M. Rutten, and F. van de Vosse (2007). A wave propagation model of blood flow in large vessels using an approximate velocity profile function. *Journal Of Fluid*

Mechanics 580(1), 145–168.

[25] Blanco, P., M. Pivello, S. Urquiza, and R. Feijóo (2009). On the potentialities of 3D-1D coupled models in hemodynamics simulations. *Journal of biomechanics 42*(7), 919–930.

[26] Borrell, A., E. Antolin, D. Costa, M. Farre, J. Martinez, and A. Fortuny (1998). Abnormal ductus venosus blood flow in trisomy 21 fetuses during early pregnancy. *American journal of obstetrics and gynecology 179*(6), 1612–1617.

[27] Borrell, A., V. Borobio, J. Bestwick, and N. Wald (2009). Ductus venosus pulsatility index as an antenatal screening marker for Down's syndrome: use with the combined and integrated tests. *Journal Of Medical Screening 16*(3), 112–118.

[28] Brace, R. (1993). Regulation of blood volume in utero. *The circulation, Fetus and neonate. Physiology and clinical application 1*, 75–99.

[29] Bramwell, J. and A. Hill (1922). The velocity of the pulse wave in man. *Proceedings Of The Royal Society Of London 93*(652), 298–306.

[30] Campbell, S., E. Mavrides, F. Prefumo, F. Presti, and J. Carvalho (2001). Prenatal diagnosis of mosaic trisomy 8 in a fetus with normal nuchal translucency thickness and reversed end-diastolic ductus venosus flow. *Ultrasound in Obstetrics & Gynecology 17*(4), 341–343.

[31] Cardamone, L., A. Valentin, J. Eberth, and J. Humphrey (2009). Origin of axial prestretch and residual stress in arteries. *Biomechanics and Modeling in Mechanobiology 8*(6), 431–446.

[32] Carew, T., R. Vaishnav, and D. Patel (1968). Compressibility of the arterial wall. *Circulation Research 23*(1), 61–68.

[33] Chow, M. and Y. Zhang (2010). Changes in the mechanical and biochemical properties of aortic tissue due to cold storage. *Journal Of Surgical Research 1*, 9.

[34] Chuong, C. and Y. Fung (1986). On residual stresses in arteries. *Journal of Biomechanical Engineering 108*(2), 189–192.

[35] Crosetto, P., P. Reymond, S. Deparis, D. Kontaxakis, N. Stergiopulos, and A. Quarteroni (2011). Fluid-structure interaction simulation of aortic blood flow. *Computers & Fluids 43*(1), 46–57.

[36] Daniel, J., K. Abe, and P. McFetridge (2005). Development of the human umbilical vein scaffold for cardiovascular tissue engineering applications. *ASAIO Journal 51*(3), 252.

[37] Degand, C. and C. Farhat (2002). A three-dimensional torsional spring analogy method for unstructured dynamic meshes. *Computers & structures 80*(3), 305–316.

[38] Degroote, J. (2010). *Development of algorithms for the partitioned simulation of strongly coupled fluid-structure interaction problems*. Ph. D. thesis, Ghent University.

[39] Degroote, J., K. Bathe, and J. Vierendeels (2009). Performance of a new partitioned procedure versus a monolithic procedure in fluid-structure interaction. *Computers & Structures 87*(11-12), 793–801.

[40] Degroote, J., R. Haelterman, S. Annerel, P. Bruggeman, and J. Vierendeels (2010). Performance of partitioned procedures in fluid-structure interaction. *Computers & Structures 88*(7-8), 446–457.

[41] DeVault, K., P. Gremaud, V. Novak, M. Olufsen, G. Vernieres, and P. Zhao (2008). Blood flow in the circle of Willis: Modeling and calibration. *Multiscale modeling & simulation: a SIAM interdisciplinary journal 7*(2), 888.

[42] Donea, J., S. Giuliani, and J. Halleux (1982). An arbitrary Lagrangian-Eulerian finite element method for transient dynamic fluid-structure interactions. *Computer Methods in Applied Mechanics and Engineering 33*(1), 689–723.

[43] Driessen, N., M. Cox, C. Bouten, and F. Baaijens (2008). Remodelling of the angular collagen fiber distribution in cardiovascular tissues. *Biomechanics and Modeling in Mechanobiology 7*(2), 93–103.

[44] Dukowicz, J. and J. Kodis (1987). Accurate conservative remapping (rezoning) for arbitrary Lagrangian-Eulerian computations. *Siam Journal On Scientific and Statistical Computing 8*, 305.

[45] Edelstone, D., A. Rudolph, and M. Heymann (1980). Effects of hypoxemia and decreasing umbilical flow liver and ductus venosus blood flows in fetal lambs. *American Journal of Physiology: Heart and Circulatory Physiology 238*(5), H656–H663.

[46] Ercal, T., S. Lacin, S. Altunyurt, U. Saygili, O. Cinar, and A. Mumcu (1996). Umbilical coiling index: Is it a marker for the foetus at risk? *The British Journal of General Practice 50*(5), 254–264.

[47] Ferguson, V. and R. Dodson (2009). Bioengineering aspects of the umbilical cord. *European Journal of Obstetrics, Gynecology and Reproductive Biology 144*, 108–113.

[48] Flory, P. (1961). Thermodynamic relations for high elastic materials. *Transactions Of The Faraday Society 57*, 829–838.

[49] Formaggia, L., J. Gerbeau, F. Nobile, and A. Quarteroni (2001). On the coupling of 3D and 1D Navier-Stokes equations for flow problems in compliant vessels. *Computer Methods in Applied Mechanics and Engineering 191*(6), 561–582.

[50] Formaggia, L., D. Lamponi, and A. Quarteroni (2003). One-dimensional models for blood flow in arteries. *Journal Of Engineering Mathematics 47*(3), 251–276.

[51] Formaggia, L., D. Lamponi, M. Tuveri, and A. Veneziani (2006). Numerical modeling of 1D arterial networks coupled with a lumped parameters description of the heart. *Computer Methods in Biomechanics and Biomedical Engineering 9*(5), 273–288.

[52] Formaggia, L., A. Quarteroni, and A. Veneziani (2009). *Cardiovascular Mathematics: Modeling and simulation of the circulatory system*, Volume 1. Springer Verlag.

[53] Fox, S. and T. Khong (1990). Lack of innervation of human umbilical cord. An immunohistological and histochemical study. *Placenta 11*(1), 59–62.

[54] Franc, S., J. Rousseau, R. Garrone, M. Van der Rest, and M. Moradi-Améli (1998). Microfibrillar composition of umbilical cord matrix: Characterization of fibrillin, collagen VI and intact collagen V. *Placenta 19*(1), 95–104.

[55] Franke, V., K. Parker, L. Wee, N. Fisk, and S. Sherwin (2003). Time domain computational modelling of 1D arterial networks in monochorionic placentas. *ESAIM: Mathematical Modelling and Numerical Analysis 37*(4), 557–580.

[56] Fung, Y. (1993). *Biomechanics: mechanical properties of living tissues*. Springer.

[57] Fung, Y. (1997). *Biomechanics: circulation*. Springer Verlag.

[58] Fung, Y. and K. Fronekk (1979). Pseudoelasticity of arteries and the choice of its mathematical expression. *American Journal Of Physiology 237*(5), H620–H631.

[59] Gasser, T., R. Ogden, and G. Holzapfel (2006). Hyperelastic modelling of arterial layers with distributed collagen fibre orientations. *Journal Of The Royal Society Interface 3*(6), 15–35.

[60] Gerbeau, J. and M. Vidrascu (2003). A quasi-Newton algorithm based on a reduced model for fluid-structure interaction problems in blood flows. *ESAIM: Mathematical Modelling and Numerical Analysis 37*(04), 631–647.

[61] Gervaso, F., G. Pennati, F. Boschetti, S. Rigano, A. Pigni, and A. Padoan (2003). Biomechanics of the human umbilical cord under compressive loads. In *2003 Summer Bioengineering Conference, June 25*, Volume 29.

[62] Ghosh, K., S. Ghosh, and A. Gupta (1984). Tensile properties of human umbilical cord. *Indian Journal Of Medical Research 79*, 538–541.

[63] Gill, R. (1979). Pulsed Doppler with B-mode imaging for quantitative blood flow measurement. *Ultrasound in medicine & biology 5*(3), 223–225.

[64] Glowinski, R., T. Pan, and J. Periaux (1994). A fictitious domain method for Dirichlet problem and applications. *Computer Methods in Applied Mechanics and Engineering 111*(3-4), 283–303.

[65] Goktas, S., N. Pierre, K. Abe, J. Dmytryk, and P. McFetridge (2009). Cellular interactions and biomechanical properties of a unique vasc-derived scaffold for periodontal tissue regeneration. *Tissue Engineering 16*(3), 769–780.

[66] Gray, H. (1918). *Anatomy of the human body*. Lea & Febiger.

[67] Gudmundsson, S. (1999). Importance of venous flow assessment for clinical decision-making. *European Journal of Obstetrics & Gynecology and Reproductive Biology 84*(2), 173–178.

[68] Gudmundsson, S., J. Huhta, D. Wood, G. Tulzer, A. Cohen, and S. Weiner (1991). Venous Doppler ultrasonography in the fetus with nonimmune hydrops. *American Journal Of Obstetrics and Gynecology 164*(1), 33–37.

[69] Haugen, G., M. Hanson, T. Kiserud, S. Crozier, H. Inskip, and K. Godfrey (2005). Fetal

liver-sparing cardiovascular adaptations linked to mothers slimness and diet. *Circulation research 96*(1), 12–14.

[70] Haugen, G., T. Kiserud, K. Godfrey, S. Crozier, and M. Hanson (2004). Portal and umbilical venous blood supply to the liver in the human fetus near term. *Ultrasound in Obstetrics & Gynecology 24*(6), 599–605.

[71] Haugen, G., J. Mellembakken, and S. Stray-Pedersen (1997). Characterization of the vasodilatatory response to serotonin in human umbilical arteries perfused in vitro. The influence of the endothelium. *Early Human Development 47*(2), 185–193.

[72] Hecher, K., C. Bilardo, R. Stigter, Y. Ville, B. Hackelöer, H. Kok, M. Senat, and G. Visser (2001). Monitoring of fetuses with intrauterine growth restriction: a longitudinal study. *Ultrasound in obstetrics & gynecology 18*(6), 564–570.

[73] Hecher, K. and S. Campbell (1996). Characteristics of fetal venous blood flow under normal circumstances and during fetal disease. *Ultrasound in Obstetrics & Gynecology 7*(1), 68–83.

[74] Hecher, K., S. Campbell, R. Snijders, and K. Nicolaides (1994). Reference ranges for fetal venous and atrioventricular blood flow parameters. *Ultrasound in Obstetrics & Gynecology 4*(5), 381–390.

[75] Hellevik, L. (2012). *Cardiovascular Biomechanics*.

[76] Hellevik, L., T. Kiserud, F. Irgens, N. Stergiopulos, and M. Hanson (1998). Mechanical properties of the fetal ductus venosus and umbilical vein. *Heart and Vessels 13*(4), 175–180.

[77] Hellevik, L., T. Kiserud, F. Irgens, T. Ytrehus, and S. Eik-Nes (1998). Simulation of pressure drop and energy dissipation for blood flow in a human fetal bifurcation. *Journal of Biomechanical Engineering 120*(4), 455–462.

[78] Hellevik, L., N. Stergiopulos, T. Kiserud, S. Rabben, S. Eik-Nes, and F. Irgens (2000). A mathematical model of umbilical venous pulsation. *Journal Of Biomechanics 33*(9), 1123–1130.

[79] Hellevik, L., J. Vierendeels, T. Kiserud, N. Stergiopulos, F. Irgens, E. Dick, K. Riemslagh, and P. Verdonck (2009). An assessment of ductus venosus tapering and wave transmission from the fetal heart. *Biomechanics and Modeling in Mechanobiology 8*(6), 509–517.

[80] Hirt, C., A. Amsden, and J. Cook (1974). An arbitrary Lagrangian-Eulerian computing method for all flow speeds. *Journal Of Computational Physics 14*(3), 227–253.

[81] Holzapfel, G. (2000). *Nonlinear Solid Mechanics - A continuum approach for engineering*. West Sussex, England: John Wiley and Sons Ltd.

[82] Holzapfel, G. and T. Gasser (2007). Computational stress-deformation analysis of arterial walls including high-pressure response. *International Journal Of Cardiology 116*(1), 78–85.

[83] Holzapfel, G., T. Gasser, and R. Ogden (2000). A new constitutive framework for arterial wall mechanics and a comparative study of material models. *Journal Of Elasticity 61*(1-3),

1–48.

[84] Holzapfel, G. and H. Weizacker (1998). Biomechanical behavior of the arterial wall and its numerical characterization. *Journal Of Elasticity 28*(4), 377–392.

[85] Hoskins, P. (1990). Measurement of arterial blood flow by Doppler ultrasound. *Clinical Physics and Physiological Measurement 11*, 1.

[86] Hron, J. and S. Turek. *A monolithic FEM solver for an ALE formulation of fluid-structure interaction with configuration for numerical benchmarking*.

[87] Hughes, T. and J. Lubliner (1973). On the one-dimensional theory of blood flow in the larger vessels. *Mathematical Biosciences 18*(1-2), 161–170.

[88] Huikeshoven, F., I. Hope, G. Power, R. Gilbert, and L. Longo (1985). Mathematical model of fetal circulation and oxygen delivery. *American Journal of Physiology: Regulatory, Integrative and Comparative Physiology 249*(2), R192.

[89] Humphrey, J. (2002). *Cardiovascular solid mechanics: cells, tissues, and organs*. Springer.

[90] Irgens, F. (2008). *Continuum mechanics*. Berlin: Springer.

[91] Itskovitz, J., E. LaGamma, and A. Rudolph (1987). Effects of cord compression on fetal blood flow distribution and O2 delivery. *American Journal Of Physiology-heart and Circulatory Physiology 252*(1), H100–H109.

[92] Johnson, P., D. Maxwell, M. Tynan, and L. Allan (2000). Intracardiac pressures in the human fetus. *Heart 84*(1), 59–63.

[93] Jones, E., T. Oliphant, P. Peterson, et al. (2001). SciPy: Open source scientific tools for Python.

[94] Kessler, J. (2007). *Portal and umbilical venous distribution in the human fetus: a longitudinal ultrasound study*. Ph. D. thesis, The University of Bergen.

[95] Kessler, J., S. Rasmussen, K. Godfrey, M. Hanson, and T. Kiserud (2008). Longitudinal study of umbilical and portal venous blood flow to the fetal liver: low pregnancy weight gain is associated with preferential supply to the fetal left liver lobe. *Pediatric Research 63*(3), 315.

[96] Kessler, J., S. Rasmussen, K. Godfrey, M. Hanson, and T. Kiserud (2011). Venous liver blood flow and regulation of human fetal growth: evidence from macrosomic fetuses. *American Journal Of Obstetrics and Gynecology 204*, 429.e1–7.

[97] Kessler, J., S. Rasmussen, M. Hanson, and T. Kiserud (2006). Longitudinal reference ranges for ductus venosus flow velocities and waveform indices. *Ultrasound in Obstetrics & Gynecology 28*(7), 890–898.

[98] Kessler, J., S. Rasmussen, and T. Kiserud (2007a). The fetal portal vein: normal blood flow development during the second half of human pregnancy. *Ultrasound in Obstetrics & Gynecology 30*(1), 52–60.

[99] Kessler, J., S. Rasmussen, and T. Kiserud (2007b). The left portal vein as an indicator of watershed in the fetal circulation: development during the second half of pregnancy and a suggested method of evaluation. *Ultrasound in Obstetrics & Gynecology 30*(5), 757–764.

[100] Khir, A. and K. Parker (2002). Measurements of wave speed and reflected waves in elastic tubes and bifurcations. *Journal Of Biomechanics 35*(6), 775–783.

[101] Kilavuz, Ö., K. Vetter, T. Kiserud, and P. Vetter (2003). The left portal vein is the watershed of the fetal venous system. *Journal Of Perinatal Medicine 31*(2), 184–187.

[102] Kiserud, T. (2000). Fetal venous circulation, an update on hemodynamics. *Journal Of Perinatal Medicine 28*(2), 90–96.

[103] Kiserud, T. (2005). Physiology of the fetal circulation. In *Seminars in Fetal and Neonatal Medicine*, Volume 10, pp. 493–503. Elsevier.

[104] Kiserud, T. and G. Acharya (2004). The fetal circulation. *Prenatal Diagnosis 24*(13), 1049–1059.

[105] Kiserud, T., S. Eik-Nes, H. Blaas, and L. Hellevik (1991). Ultrasonographic velocimetry of the fetal ductus venosus. *Lancet 338*(8780), 1412–1414.

[106] Kiserud, T., S. Eik-Nes, H. Blaas, and L. Hellevik (1992). Foramen ovale: an ultrasonographic study of its relation to the inferior vena cava, ductus venosus and hepatic veins. *Ultrasound in Obstetrics & Gynecology 2*(6), 389–396.

[107] Kiserud, T., S. Eik-Nes, H. Blaas, L. Hellevik, and B. Simensen (1994). Ductus venosus blood velocity and the umbilical circulation in the seriously growth-retarded fetus. *Ultrasound in Obstetrics & Gynecology 4*(2), 109–114.

[108] Kiserud, T., S. Eik-Nes, L. Hellevik, and H. Blaas (1992). Ductus venosus: a longitudinal Doppler velocimetric study of the human fetus. *Journal Of Maternal-fetal Investigation 2*(1), 5–11.

[109] Kiserud, T., S. Eik-Nes, L. Hellevik, and H. Blaas (1993). Ductus venosus blood velocity changes in fetal cardiac diseases. *Journal of Maternal-Fetal Investigation 3*, 15–20.

[110] Kiserud, T., L. Hellevik, S. Eik-Nes, B. Angelsen, and H. Blaas (1994). Estimation of the pressure gradient across the fetal ductus venosus based on Doppler velocimetry. *Ultrasound in medicine & biology 20*(3), 225–232.

[111] Kiserud, T., L. Hellevik, and M. Hanson (1998). Blood velocity profile in the ductus venosus inlet expressed by the mean/maximum velocity ratio. *Ultrasound in medicine & biology 24*(9), 1301–1306.

[112] Kiserud, T., J. Kessler, C. Ebbing, and S. Rasmussen (2006). Ductus venosus shunting in growth-restricted fetuses and the effect of umbilical circulatory compromise. *Ultrasound in Obstetrics & Gynecology 28*(2), 143–149.

[113] Kiserud, T., Ö. Kilavuz, and L. Hellevik (2003). Venous pulsation in the fetal left portal branch: the effect of pulse and flow direction. *Ultrasound in Obstetrics & Gynecology 21*(4),

359–364.

[114] Kiserud, T., T. Ozaki, H. Nishina, C. Rodeck, and M. Hanson (2000). Effect of NO, phenylephrine, and hypoxemia on ductus venosus diameter in fetal sheep. *American Journal Of Physiology-heart and Circulatory Physiology 279*(3), H1166–H1171.

[115] Kiserud, T., S. Rasmussen, and S. Skulstad (2000). Blood flow and the degree of shunting through the ductus venosus in the human fetus. *American Journal Of Obstetrics and Gynecology 182*(1), 147–153.

[116] Kiserud, T., L. Stratford, and M. Hanson (1997). Umbilical flow distribution to the liver and the ductus venosus: an in vitro investigation of the fluid dynamic mechanisms in the fetal sheep. *American Journal Of Obstetrics and Gynecology 177*(1), 86–90.

[117] Kivilevitch, Z., L. Gindes, H. Deutsch, and R. Achiron (2009). In-utero evaluation of the fetal umbilical–portal venous system: two-and three-dimensional ultrasonic study. *Ultrasound in Obstetrics & Gynecology 34*(6), 634–642.

[118] Kroon, M. and G. Holzapfel (2008). A new constitutive model for multi-layered collagenous tissues. *Journal Of Biomechanics 41*(12), 2766–2771.

[119] Lanir, Y., Y. Hollander, D. Durban, X. Lu, and G. Kassab (2011). Constitutive modeling of coronary arterial media-comparison of three model classes. *Journal of Biomechanical Engineering 1*, 282.

[120] Leinan, P., L. Hellevik, V. Victorien, T. Kiserud, and B. Skallerud (2009). On material modelling of the umbilical vein. In *MekIT'09: Fifth National Conference on Computational Mechanics*, pp. 281–295. Tapir Akademisk Forlag.

[121] Li, W., T. Huang, Y. Zeng, and Z. Yao (2006). The relationship between gestational age and compliance in human umbilical vein and its possible application in vascular grafting. *Annals Of Vascular Surgery 20*(2), 237–242.

[122] Li, W., X. Ruan, H. Zhang, and Y. Zeng (2006). Biomechanical properties of different segments of human umbilical cord vein and its value for clinical application. *Journal Of Biomedical Materials Research 76*(1), 93–97.

[123] Li, W., H. Zhang, P. Wang, G. Xi, H. Wang, Y. Chen, Z. Deng, Z. Zhang, and T. Huang (2008). Quantitative analysis of the microstructure of human umbilical vein for assessing feasibility as vessel substitute. *Annals Of Vascular Surgery 22*(3), 417–424.

[124] Lingman, G., J. Laurin, and K. Maršál (1986). Circulatory changes in fetuses with imminent asphyxia. *Neonatology 49*(2), 66–73.

[125] MacCormack, R. (1969). The effect of viscosity in hypervelocity impact cratering. *Frontiers of Computational Fluid Dynamics*, 27–44.

[126] Maiz, N. and K. Nicolaides (2010). Ductus venosus in the first trimester: contribution to screening of chromosomal, cardiac defects and monochorionic twin complications. *Fetal Diagnosis and Therapy 28*(2), 65–71.

[127] Maiz, N., W. Plasencia, T. Dagklis, E. Faros, and K. Nicolaides (2008). Ductus venosus Doppler in fetuses with cardiac defects and increased nuchal translucency thickness. *Ultrasound in Obstetrics & Gynecology 31*(3), 256–260.

[128] Marchandise, E., M. Willemet, and V. Lacroix (2009). A numerical hemodynamic tool for predictive vascular surgery. *Medical Engineering & Physics 31*(1), 131–144.

[129] Martin, B. and R. Tudor (1980). The umbilical and paraumbilical veins of man. *Journal Of Anatomy 130*(Pt 2), 305.

[130] Matias, A., C. Gomes, N. Flack, N. Montenegro, and K. Nicolaides (1998). Screening for chromosomal abnormalities at 10–14 weeks: the role of ductus venosus blood flow. *Ultrasound in Obstetrics & Gynecology 12*(6), 380–384.

[131] Matias, A. and N. Montenegro (2011). Ductus venosus: A love story of 14 years. *Donald School Ultrasound in Obstetrics and Gynecology 5*(2), 00–00.

[132] Maulik, D. (2005). *Doppler Ultrasound in Obstetrics & Gynecology*. Springer Verlag.

[133] Mavrides, E., G. Moscoso, J. Carvalho, S. Campbell, and B. Thilaganathan (2001). The anatomy of the umbilical, portal and hepatic venous systems in the human fetus at 14–19 weeks of gestation. *Ultrasound in Obstetrics & Gynecology 18*(6), 598–604.

[134] Mavrides, E., G. Moscoso, J. Carvalho, S. Campbell, and B. Thilaganathan (2002). The human ductus venosus between 13 and 17 weeks of gestation: histological and morphometric studies. *Ultrasound in Obstetrics & Gynecology 19*(1), 39–46.

[135] Meyer, F., Z. Laver-Rudich, and R. Tanenbaum (1983). Evidence for a mechanical coupling of glycoprotein microfibrils with collagen fibrils in Wharton's jelly. *Biochimica Et Biophysica Acta 755*(3), 376–387.

[136] Meyer, W. and J. Lind (1966). The ductus venosus and the mechanism of its closure. *Archives Of Disease in Childhood 41*(220), 597.

[137] Migliavacca, F., R. Balossino, G. Pennati, G. Dubini, T. Hsia, M. De Leval, and E. Bove (2006). Multiscale modelling in biofluidynamics: application to reconstructive paediatric cardiac surgery. *Journal Of Biomechanics 39*(6), 1010–1020.

[138] Mildenberger, E., B. Biesel, G. Siegel, and H. Versmold (2003). Nitric oxide and endothelin in oxygen-dependent regulation of vascular tone of human umbilical vein. *American Journal Of Physiology 285*(4), H1730–7.

[139] Mildenberger, E., G. Siegel, and H. Versmold (2004). Prostanoids contribute to the oxygen-dependent regulation of vascular tone of human umbilical vein. *Journal Of Perinatal Medicine 32*(2), 149–154.

[140] Moireau, P., N. Xiao, M. Astorino, C. Figueroa, D. Chapelle, C. Taylor, and J. Gerbeau (2012). External tissue support and fluid-structure simulation in blood flows. *Biomechanics and Modeling in Mechanobiology 11*(1), 1–18.

[141] Murphy, P. (2005). The fetal circulation. *BJA-CEPD Reviews 5*(4), 107–112.

[142] Mynard, J., M. Davidson, D. Penny, and J. Smolich (2010). A numerical model of neonatal pulmonary atresia with intact ventricular septum and RV-dependent coronary flow. *International Journal for Numerical Methods in Biomedical Engineering 26*(7), 843–861.

[143] Mynard, J. and P. Nithiarasu (2008). A 1D arterial blood flow model incorporating ventricular pressure, aortic valve and regional coronary flow using the locally conservative Galerkin (LCG) method. *Communications in Numerical Methods in Engineering 24*(5), 367–417.

[144] Nanaev, A., G. Kohnen, A. Milovanov, S. Domogatsky, and P. Kaufmann (1997). Stromal differentiation and architecture of the human umbilical cord. *Placenta 18*(1), 53–64.

[145] Naro, E. D., F. Ghezzi, L. Raio, M. Franchi, and V. D'Addario (2001). Umbilical cord morphology and pregnancy outcome. *European Journal of Obstetrics, Gynecology and Reproductive Biology 96*(2), 150–157.

[146] Nobile, F. (2009). Coupling strategies for the numerical simulation of blood flow in deformable arteries by 3D and 1D models. *Mathematical and Computer Modelling 49*(11-12), 2152–2160.

[147] Ogden, R. (2009). Anisotropy and nonlinear elasticity in arterial wall mechanics. In G. A. Holzapfel, R. W. Ogden, F. Pfeiffer, F. G. Rammerstorfer, J. Salençon, B. Schrefler, and P. Serafini (Eds.), *Biomechanical Modelling at the Molecular, Cellular and Tissue Levels*, Volume 508 of *CISM Courses and Lectures*, pp. 179–258. Springer Vienna.

[148] Ottosen, N. and H. Petersson (1992). *Introduction to the finite element method*. Prentice-Hall.

[149] Parker, K., C. Jones, et al. (1990). Forward and backward running waves in the arteries: analysis using the method of characteristics. *Journal of Biomechanical Engineering 112*(3), 322–326.

[150] Pennati, G. (2001). Biomechanical properties of the human umbilical cord. *Biorheology 38*(5-6), 355–366.

[151] Pennati, G., M. Bellotti, E. Ferrazzi, M. Bozzo, G. Pardi, and R. Fumero (1998). Blood flow through the ductus venosus in human fetus: calculation using Doppler velocimetry and computational findings. *Ultrasound in medicine & biology 24*(4), 477–487.

[152] Pennati, G., M. Bellotti, and R. Fumero (1997). Mathematical modelling of the human foetal cardiovascular system based on Doppler ultrasound data. *Medical Engineering & Physics 19*(4), 327–335.

[153] Pennati, G., C. Corno, M. Costantino, and M. Bellotti (2003). Umbilical flow distribution to the liver and the ductus venosus in human fetuses during gestation: an anatomy-based mathematical modeling. *Medical Engineering & Physics 25*(3), 229–238.

[154] Pennati, G., A. Redaelli, M. Bellotti, and E. Ferrazzi (1996). Computational analysis of the ductus venosus fluid dynamics based on Doppler measurements. *Ultrasound in medicine & biology 22*(8), 1017–1029.

[155] Peskin, C. (1972). Flow patterns around heart valves: a numerical method. *Journal Of Computational Physics 10*(2), 252–271.

[156] Prot, V. and B. Skallerud (2009). Nonlinear solid finite element analysis of mitral valves with heterogeneous leaflet layers. *Computational Mechanics 43*(3), 353–368.

[157] Prot, V., B. Skallerud, and G. Holzapfel (2007). Transversely isotropic membrane shells with application to mitral valve mechanics. Constitutive modelling and finite element implementation. *International Journal for Numerical Methods in Engineering 71*(8), 987–1008.

[158] Quarteroni, A. and L. Formaggia (2004). Mathematical modelling and numerical simulation of the cardiovascular system. In N. Ayache (Ed.), *Computational Models for the Human Body*, Volume 12 of *Handbook of Numerical Analysis*, pp. 3–127. Elsevier.

[159] Raines, J., M. Jaffrin, and A. Shapiro (1974). A computer simulation of arterial dynamics in the human leg. *Journal Of Biomechanics 7*(1), 77–91.

[160] Rasanen, J., D. Wood, S. Weiner, A. Ludomirski, and J. Huhta (1996). Role of the pulmonary circulation in the distribution of human fetal cardiac output during the second half of pregnancy. *Circulation 94*(5), 1068–1073.

[161] Reymond, P., F. Merenda, F. Perren, D. Rüfenacht, and N. Stergiopulos (2009). Validation of a one-dimensional model of the systemic arterial tree. *American Journal Of Physiology-heart and Circulatory Physiology 297*(1), H208.

[162] Rezakhaniha, R., A. Agianniotis, J. Schrauwen, A. Griffa, D. Sage, C. Bouten, F. van de Vosse, M. Unser, and N. Stergiopulos (2012). Experimental investigation of collagen waviness and orientation in the arterial adventitia using confocal laser scanning microscopy. *Biomechanics and Modeling in Mechanobiology 11*(3/4), 461.

[163] Rezakhaniha, R. and N. Stergiopulos (2008). A structural model of the venous wall considering elastin anisotropy. *Journal of Biomechanical Engineering 130*, 031017.

[164] Rhoades, D., U. Latza, and B. Mueller (1999). Risk factors and outcomes associated with nuchal cord: a population-based study. *Journal Of Reproductive Medicine 44*(1), 39–45.

[165] Rudolph, A. and M. Heymann (1970). Circulatory changes during growth in the fetal lamb. *Circulation Research 26*(3), 289–299.

[166] Sage, D. (2012). OrientationJ, plug-in for ImageJ for directional analysis in images. Biomedical Image Group (BIG), EPFL, Switzerland.

[167] Schröder, H., M. Tchirikov, and C. Rybakowski (2003). Pressure pulses and flow velocities in central veins of the anesthetized sheep fetus. *American Journal of Physiology: Heart and Circulatory Physiology 284*(4), H1205–H1211.

[168] Sherwin, S., L. Formaggia, J. Peiro, and V. Franke (2003). Computational modelling of 1D blood flow with variable mechanical properties and its application to the simulation of wave propagation in the human arterial system. *International Journal for Numerical Methods in Fluids 43*(6-7), 673–700.

[169] Sherwin, S., V. Franke, J. Peiro, and K. Parker (2003). One-dimensional modelling of a vascular network in space-time variables. *Journal Of Engineering Mathematics 47*(3), 217–250.

[170] Shung, K., R. Sigelmann, and G. Schmer (1975). Ultrasonic measurement of blood coagulation time. *Biomedical Engineering, IEEE Transactions on* (4), 334–337.

[171] Skulstad, S. (2005). *Umbilical vein constriction at the abdominal wall An ultrasound study in low risk pregnancies*. Ph. D. thesis, The University of Bergen.

[172] Skulstad, S., M. Ulriksen, S. Rasmussen, and T. Kiserud (2006). Effect of umbilical ring constriction on Wharton's jelly. *Ultrasound in Obstetrics & Gynecology 28*(5), 692–698.

[173] Smolich, J., J. Mynard, and D. Penny (2009). Ductus arteriosus wave intensity analysis in fetal lambs: midsystolic ductal flow augmentation is due to antegrade pulmonary arterial wave transmission. *American Journal of Physiology-Regulatory, Integrative and Comparative Physiology 297*(4), R1171–R1179.

[174] Smolich, J., J. Mynard, and D. Penny (2011). Pulmonary trunk, ductus arteriosus, and pulmonary arterial phasic blood flow interactions during systole and diastole in the fetus. *Journal Of Applied Physiology 110*(5), 1362–1373.

[175] Solomon, E., R. Schmidt, and P. Adragna (1990). *Human anatomy and physiology*. Saunders College Publishing, Philadelphia, PA.

[176] Stemper, B., N. Yoganandan, M. Stineman, T. Gennarelli, J. Baisden, and F. Pintar (2007). Mechanics of fresh, refrigerated, and frozen arterial tissue. *Journal Of Surgical Research 139*(2), 236–242.

[177] Stergiopulos, N., D. Young, and T. Rogge (1992). Computer simulation of arterial flow with applications to arterial and aortic stenoses. *Journal Of Biomechanics 25*(12), 1477–1488.

[178] Tchirikov, M., S. Kertschanska, and H. Schröder (2003). Differential effects of catecholamines on vascular rings from ductus venosus and intrahepatic veins of fetal sheep. *Journal of Physiology 548*(2), 519–526.

[179] Tchirikov, M., C. Rybakowski, B. Hüneke, and H. Schröder (1998). Blood flow through the ductus venosus in singleton and multifetal pregnancies and in fetuses with intrauterine growth retardation. *American Journal of Obstetrics and Gynecology 178*(5), 943–949.

[180] Tchirikov, M., H. Schröder, and K. Hecher (2006). Ductus venosus shunting in the fetal venous circulation: regulatory mechanisms, diagnostic methods and medical importance. *Ultrasound in Obstetrics & Gynecology 27*(4), 452–461.

[181] Torii, R., M. Oshima, T. Kobayashi, K. Takagi, and T. Tezduyar (2008). Fluid–structure interaction modeling of a patient-specific cerebral aneurysm: influence of structural modeling. *Computational Mechanics 43*(1), 151–159.

[182] Toyama, J., M. Brizot, A. Liao, L. Lopes, R. Nomura, F. Saldanha, and M. Zugaib (2004). Ductus venosus blood flow assessment at 11 to 14 weeks of gestation and fetal outcome.

Ultrasound in Obstetrics & Gynecology 23(4), 341–345.

[183] van de Vosse, F. and N. Stergiopulos (2011). Pulse wave propagation in the arterial tree. *Annual Review Of Fluid Mechanics 43*, 467–499.

[184] van den Broek, C., A. van der Horst, M. Rutten, and F. van de Vosse (2011). A generic constitutive model for the passive porcine coronary artery. *Biomechanics and Modeling in Mechanobiology 10*(2), 249–258. 10.1007/s10237-010-0231-9.

[185] Versteeg, H. and W. Malalasekera (2007). *An introduction to computational fluid dynamics: the finite volume method*. Prentice Hall.

[186] Vierendeels, J., K. Dumont, E. Dick, and P. Verdonck (2005). Analysis and stabilization of fluid-structure interaction algorithm for rigid-body motion. *AIAA Journal 43*(12), 2549–2557.

[187] Vierendeels, J., L. Lanoye, J. Degroote, and P. Verdonck (2007). Implicit coupling of partitioned fluid-structure interaction problems with reduced order models. *Computers & Structures 85*(11-14), 970–976.

[188] Ville, Y., I. Sideris, K. Hecher, R. Snijders, and K. Nicolaides (1994). Umbilical venous pressure in normal, growth-retarded, and anemic fetuses. *American Journal Of Obstetrics and Gynecology 170*(2), 487–494.

[189] Vizza, E., S. Correr, V. Goranova, R. Heyn, P. Angelucci, R. Forleo, and P. Motta (1996). The collagen skeleton of the human umbilical cord at term. A scanning electron microscopy study after 2N-NaOH maceration. *Reproduction Fertility Dev 8*(5), 885–894.

[190] Wall, W., P. Gamnitzer, and A. Gerstenberger (2008). Fluid-structure interaction approaches on fixed grids based on two different domain decomposition ideas. *International Journal Of Computational Fluid Dynamics 22*(6), 411–427.

[191] Wang, J. and K. Parker (2004). Wave propagation in a model of the arterial circulation. *Journal Of Biomechanics 37*(4), 457–470.

[192] Weiner, C., J. Heilskov, G. Pelzer, S. Grant, K. Wenstrom, and R. Williamson (1989). Normal values for human umbilical venous and amniotic fluid pressures and their alteration by fetal disease. *American Journal Of Obstetrics and Gynecology 161*(3), 714.

[193] Westerhof, N., J. Lankhaar, and B. Westerhof (2009). The arterial windkessel. *Medical & Biological Engineering & Computing 47*(2), 131–141.

[194] White, F. (2007). *Fluid mechanics*. McGraw-Hill, New York.

[195] Xiu, D. and S. Sherwin (2007). Parametric uncertainty analysis of pulse wave propagation in a model of a human arterial network. *Journal Of Computational Physics 226*(2), 1385–1407.

[196] Zulliger, M., P. Fridez, K. Hayashi, and N. Stergiopulos (2004). A strain energy function for arteries accounting for wall composition and structure. *Journal Of Biomechanics 37*(7), 989–1000.